AD-A105 501 AIR FORCE INST OF TECH WRIGHT-PATTERSON AFB OH F/G 7/2
THE INITIALIZATION OF THE DIVERGENT COMPONENT OF THE HORIZONTAL--ETC(U)
MAY 79 T C TARBELL
UNCLASSIFIED AFIT-CI-79-294D-S NL

1 OF 3
AD
A105501

The Pennsylvania State University

The Graduate School

Department of Meteorology

The Initialization of the Divergent Component of the Horizontal Wind in Mesoscale Numerical Weather Prediction Models and Its Effect on Initial Precipitation Rates

A Thesis in

Meteorology

by

Terry Charles Tarbell

Submitted in Partial Fulfillment
of the Requirements
for the Degree of

Doctor of Philosophy

May 1979

UNCLASS

SECURITY CLASSIFICATION OF THIS PAGE (When Data Entered)

REPORT DOCUMENTATION PAGE		READ INSTRUCTIONS BEFORE COMPLETING FORM
1. REPORT NUMBER 79-294D-S	2. GOVT ACCESSION NO.	3. RECIPIENT'S CATALOG NUMBER
4. TITLE (and Subtitle) The Initialization of the Divergent Component of the Horizontal Wind in Mesoscale Numerical Weather Prediction Models and Its Effect on Initial Precipitation Rates		5. TYPE OF REPORT & PERIOD COVERED THESIS/DISSERTATION
		6. PERFORMING ORG. REPORT NUMBER
7. AUTHOR(s) Terry Charles Tarbell		8. CONTRACT OR GRANT NUMBER(s)
9. PERFORMING ORGANIZATION NAME AND ADDRESS AFIT STUDENT AT: Pennsylvania State Univ		10. PROGRAM ELEMENT, PROJECT, TASK AREA & WORK UNIT NUMBERS
11. CONTROLLING OFFICE NAME AND ADDRESS AFIT/NR WPAFB OH 45433		12. REPORT DATE May 1979
		13. NUMBER OF PAGES 210
14. MONITORING AGENCY NAME & ADDRESS(if different from Controlling Office)		15. SECURITY CLASS. (of this report) UNCLASS
		15a. DECLASSIFICATION/DOWNGRADING SCHEDULE

16. DISTRIBUTION STATEMENT (of this Report)

APPROVED FOR PUBLIC RELEASE; DISTRIBUTION UNLIMITED

17. DISTRIBUTION STATEMENT (of the abstract entered in Block 20, if different from Report)

FREDRIC C. LYNCH, Major, USAF
Director of Public Affairs

18. SUPPLEMENTARY NOTES

APPROVED FOR PUBLIC RELEASE: IAW AFR 190-17

Fredric C Lynch

FREDRIC C. LYNCH, Major, USAF
Director of Public Affairs
Air Force Institute of Technology (ATC)
Wright-Patterson AFB, OH 45433

30 SEP 1981

19. KEY WORDS (Continue on reverse side if necessary and identify by block number)

20. ABSTRACT (Continue on reverse side if necessary and identify by block number)

ATTACHED

DD FORM 1 JAN 73 1473 EDITION OF 1 NOV 65 IS OBSOLETE

UNCLASS

SECURITY CLASSIFICATION OF THIS PAGE (When Data Entered)

The signatories below indicate that they have read and approved the thesis of Terry Charles Tarbell.

Date of Signature:	Signatories:
5/8/1979	Thomas T. Warner, Assistant Professor of Meteorology, Chairman of Committee, Thesis Advisor
Mar. 5, 1979	Alfred K. Blackadar, Head of the Department of Meteorology
Mar. 5, 1979	Richard A. Anthes, Professor of Meteorology
March 1, 1979	Sabih I. Hayek, Professor of Engineering Mechanics

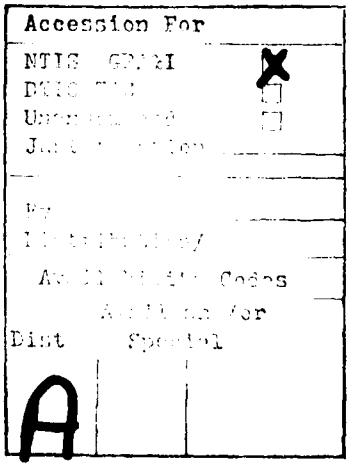

ABSTRACT

Numerical weather prediction models have not produced accurate precipitation forecasts, especially short-term forecasts of significant precipitation events. One reason for this has been that numerical models are normally initialized with nondivergent winds. This means the model must develop a vertical motion field and an associated precipitation field. Therefore, the initial precipitation rate is underforecast and the precipitation forecast itself is adversely affected. One method of solving this problem is the initialization of the divergent wind component (hereafter termed divergent initialization). Previous divergent initialization attempts have been primarily on the synoptic scale. These attempts did not produce a significant change in the initial precipitation rate. Divergent initialization on the mesoscale will be attempted here.

The general divergent initialization procedure proceeds as follows: omega values are diagnosed using the omega equation; velocity potentials are derived from the vertical velocities with the continuity equation; the divergent wind components are obtained from the velocity potentials; geopotentials are calculated on sigma surfaces using a balance equation with contributions from both the nondivergent and divergent wind components; finally, balanced temperatures are derived using the hydrostatic equation.

A scale analysis was performed on the vertical velocity and divergence equations to determine the forms appropriate for the mesoscale (grid increments from 60 to 200 km). The scale-dependent

differences of divergent initialization on the synoptic and mesoscales were studied. Both nondivergent and divergent wind components are required for these equations. To obtain them, boundary conditions on stream function and velocity potential are required. The low-wavenumber boundary variation of stream function and velocity potential should be specified accurately to minimize the influence of the boundary values on the solution in the domain interior. A method for specifying boundary conditions on velocity potential with accurate low-wavenumber boundary variation was developed.

The forecast model used was developed at The Pennsylvania State University. The version used here had six levels, low-resolution planetary boundary layer physics, and a grid increment of 120 km.

The mesoscale omega equation was solved by three-dimensional relaxation over the domain. The observed rainfall rate was used to construct a parabolic omega profile. A heating rate was derived from the profile and used as input for the diabatic term in the omega equation. On the mesoscale, the largest single term in the omega equation was the diabatic term. The greatest uncertainty in the calculation of omega values was the representativeness of the observed precipitation rate.

Five 12-hour forecasts were conducted, two with unbalanced initial conditions and three with different balanced initial conditions. Three forecasts had essentially nondivergent initial conditions. The fifth forecast was balanced on sigma surfaces and was initialized with

the total wind, the divergent part of which was derived from the diagnosed omega field. The noise characteristics of the five forecasts did not differ greatly from those reported by other investigators. However, the forecast from the divergent initialization produced more precipitation than the other forecasts, especially in the first three hours. Also, the divergent initialization produced a more evenly distributed precipitation prediction. The forecast model retained the initial divergence. The effect of divergent initialization was significant for this case and would likely improve short-range precipitation forecasts from mesoscale numerical weather prediction models.

TABLE OF CONTENTS

TABLE OF CONTENTS (Continued)

TABLE OF CONTENTS (Continued)

TABLE OF CONTENTS (Continued)

LIST OF TABLES

LIST OF FIGURES

LIST OF FIGURES (Continued)

LIST OF FIGURES (Continued)

LIST OF FIGURES (Continued)

LIST OF FIGURES (Continued)

LIST OF FIGURES (Continued)

LIST OF SYMBOLS

a	earth radius = 6.37×10^6 m; coefficient in equation for convective omega profile (Appendix 1)
A	amplitude of velocity potential in (2.66); domain area; area of overlap region (Appendix 3)
$A_{i,j}$	$p_{i,j}\, u_{i,j}$
b	coefficient in equation for convective omega profile
B	$f\zeta$
$B_{i,j}$	$p_{i,j}\, v_{i,j}$
BADJ	boundary velocity potential gradient correction (Section 2.3.4)
c	coefficient in equation for convective omega profile
c_B	correction to be added to $v_{n_{obs}}$ in Anthes (1976) method for the determination of ψ_B
$c_{\ell,k}$	correlation coefficient for a displacement given by ℓ and k
c_p	specific heat capacity of dry air at constant pressure
c_1, c_2	arbitrary constants
C	characteristic phase speed of motions considered; matrix of correlation coefficients for precipitation scoring (Appendix 3)
C_D	surface drag coefficient
d	depth of PBL
D	horizontal divergence = $\nabla \cdot \underset{\sim}{V}$
D_1	length of domain in y direction
$\hat{D}$	characteristic value of the local rate of change of divergence
e_s	saturation vapor pressure
f	Coriolis parameter = $2\Omega \sin\Phi$

LIST OF SYMBOLS (Continued)

f_1, f_2, f_3	humidity parameters defined by (A1.20a), (A1.20b), and (A1.20c), respectively
f_o	typical mid-latitude value of $f = 10^{-4}$ s^{-1}
F	forcing function in omega equation relaxation
F(x,y)	general forcing function
Fr_x	component of $\underset{\sim}{Fr}$ in the x direction
Fr_y	component of $\underset{\sim}{Fr}$ in the y direction
$\underset{\sim}{Fr}$	surface friction force
g	acceleration of gravity
$\underset{\sim}{G}$	general horizontal vector
G	Green's function (Section 2.3.4)
G_i	in an S1 score, the maximum of Δp_f and Δp_o (Section 7.2.2)
h	actual height above sea level or terrain height above sea level; heating rate per unit mass of air (Appendix 1)
H	atmospheric scale height = RT/g
H_s	rate of sensible heat addition per unit mass from a water surface
i	index in finite-difference equations in the x direction; $\sqrt{-1}$
$\hat{i}$	unit vector in the positive x direction
j	index in finite-difference equations in the y direction
$\hat{j}$	unit vector in the positive y direction
k	index in finite-difference equations in the z direction; north-south displacement of forecast precipitation field with respect to the observed field (Appendix 3)
$\hat{k}$	unit vector in the positive z direction

LIST OF SYMBOLS (Continued)

KMAX	one less than the number of levels (Appendix 1)
ℓ	east-west displacement of forecast precipitation field with respect to the observed field
L	characteristic horizontal length scale; latent heat of condensation (Appendix 1)
L_p	length of the domain perimeter
L_l	length of the domain in the x direction
m	map scale factor
m_v	molecular weight of water = 18 g
M	number of points in the y direction (Appendix 3)
MAXBDY	number of iterations for which χ_B is corrected (Section 2.3.4)
n	coordinate direction normal to the domain boundary; iteration number (Appendix 1)
$\hat{n}$	unit normal vector, positive outward
N	number of points in the x direction (Appendix 3)
NBP	number of boundary points in Eq. (2.57)
p	pressure
$p_{i,j}$	$\overline{\overline{p_*}^{xy}}_{i,j}$
p_m	$(p_t+p_s)/2$
p_n	pressure at sigma level n
p_o	sea level pressure
p_s	surface pressure
p_t	pressure at the model top
p_*	p_s-p_t
P	precipitation matrix (Appendix 3)

LIST OF SYMBOLS (Continued)

$P_{i,j}$	precipitation amount at point (i,j) (Appendix 3)
PF	forecast precipitation matrix
PO	observed precipitation matrix
q	specific humidity
q_s	saturation specific humidity
Q	diabatic heating rate per unit mass of dry air
R	specific gas constant for dry air; rain rate (Appendix 1)
R'	$1.134(10^{-6})$ R where R is rainfall rate (Appendix 1)
$R^n_{i,j,k}$	residual at point (i,j,k) after iteration n
Ro	Rossby number = V/fL
R_1	characteristic ratio of divergence to vorticity for a given L
R_2	parameter used for rain rate in the scale analysis of the vertical velocity equation
R^*	universal gas constant
s	coordinate direction along domain boundary, positive in the counterclockwise direction
S_{PF}	variance of forecast precipitation field
S_{PO}	variance of observed precipitation field
t	time
$\hat{t}$	tangent unit vector in the counterclockwise direction
T	temperature
T	characteristic local time scale
Tx	where x is a term number in an equation
u	horizontal velocity component in the positive x direction

LIST OF SYMBOLS (Continued)

u_χ	divergent part of u
u_ψ	nondivergent part of u
v	horizontal velocity component in the positive y direction
v_n	horizontal velocity component normal to the domain boundary, positive outward
v_t	horizontal velocity component in the s direction
v_χ	divergent part of v
v_ψ	nondivergent part of v
V	characteristic horizontal velocity
$\underset{\sim}{V}$, $\underset{\sim}{V}_H$	horizontal wind velocity = $u\hat{i} + v\hat{j}$
$\underset{\sim}{V}_\chi$	$u_\chi\hat{i} + v_\chi\hat{j}$ on a constant pressure surface
$\underset{\sim}{V}_\psi$	$u_\psi\hat{i} + v_\psi\hat{j}$ on a constant pressure surface
x	horizontal coordinate of Lambert conformal projection; at grid center, x-axis is oriented east-west
x_o	x coordinate of a divergence source (Section 2.3.4)
y	horizontal coordinate of Lambert conformal projection; at grid center, y-axis is oriented north-south
y_o	y coordinate of a divergence source (Section 2.3.4)
z	vertical coordinate
Z	generalized vertical coordinate = $-\ln(p/p_o)$
α	specific volume
β_1	df/dy
β	$\partial f/\partial y$ on a rectangular grid
γ	lapse rate = $-\partial T/\partial z$
γ_1	$\partial f/\partial x$ on a rectangular grid
γ_d	dry adiabatic lapse rate = g/c_p

LIST OF SYMBOLS (Continued)

Γ	static stability in Z coordinates
$\delta(\ )$	vertical finite-difference operator defined by (5.4b)
ϵ	0.622
ζ	relative vorticity = $\hat{k}\cdot\nabla \times \underset{\sim}{V}$
ζ_a	$\zeta + f$
θ	potential temperature
κ	R/c_p; wavenumber (Section 2.1.5)
μ	damping factor
π	3.14159 ...
ρ	density of air
ρ_s	surface density of air
σ	$(p - p_t)/p_*$ = a vertical coordinate
σ_s	static stability
$\dot{\sigma}$	vertical velocity in sigma coordinates
Σ	summation symbol
$\underset{\sim}{\tau}$	$\tau_{zx}\hat{i} + \tau_{zy}\hat{j}$
τ_{zx}	surface stress component in the x direction
τ_{zy}	surface stress component in the y direction
ϕ	geopotential = gh
ϕ_n	geopotential at level n
ϕ'	perturbation geopotential
$\phi_{RB}(x,y)$	when a Poisson equation is solved on a rectangular domain, ϕ_{RB} is that portion of ϕ (a general variable) on the interior of the domain due to the value of ϕ on the right boundary of the domain

LIST OF SYMBOLS (Continued)

Φ	latitude
χ	velocity potential
ψ	stream function
ω	vertical velocity in pressure coordinates = dp/dt
ω_{max}	maximum omega in the convective omega profile
Ω	rate of rotation of the earth = 7.292×10^{-5} s^{-1}
Δx	grid increment; characteristic model grid increment (Chapter 1)
Δx_1	characteristic synoptic model grid increment
Δx_2	characteristic upper meso-β scale grid increment
Δx_3	characteristic meso-γ scale grid increment
$\nabla_n(\nabla)$	horizontal gradient measured on a surface of constant n where n = p, σ, or Z
$\nabla_n^2(\nabla^2)$	horizontal Laplacian measured on a surface of constant n where n = p, σ, or Z
∇^2	finite-difference Laplacian
$\overline{(\ )}$	mean value of ( )
$\overline{(\ )}^x$	finite-difference average defined by (5.2c)
$\overline{(\ )}^y$	finite-difference average defined by (5.2d)
$\overline{(\ )}^\sigma$	finite-difference average defined by (5.4a)
$\dot{(\ )}$	d( )/dt
$(\ )_a$	actual or known value of ( ) (Section 2.3.4)
$(\ )_c$	current value of ( ) (Section 2.3.4)
$(\ )_g$	geostrophic ( )
$(\ )_B$	boundary value of ( )

LIST OF SYMBOLS (Continued)

$( )_{B-1}$	value of ( ) at the first interior grid point
$( )_{i,j,k}$	value of ( ) at point (i,j,k)
$( )_{i,j}$	value of ( ) at point (i,j)
$( )_{k}$	value of ( ) at level k
$( )_{obs}$	observed value of ( )
$( )_{p}$	( ) on a pressure surface
$( )_{t}$	value of ( ) due to terrain
$( )_{x}$	finite-difference operator defined by (5.2a); partial differentiation with respect to x
$( )_{y}$	finite-difference operator defined by (5.2b); partial differentiation with respect to y
$( )_{\sigma}$	( ) on a sigma surface
$\widehat{( )}^{x}$	finite-difference operator defined by (5.3a)
$\widehat{( )}^{y}$	finite-difference operator defined by (5.3b)
$\equiv$	is identical to, is defined by
$\sim$	approximately, on the order of
$<<$	at least two orders of magnitude smaller than
$\lvert \underset{\sim}{G} \rvert$	magnitude of vector $\underset{\sim}{G} = (\underset{\sim}{G} \cdot \underset{\sim}{G})^{\frac{1}{2}}$

LIST OF ABBREVIATIONS

AW	Anthes and Warner, 1978 (a reference)
CFL	Courant-Friedrichs-Lewy
DI	dynamic initialization
FD	finite-difference
FNWC	Fleet Numerical Weather Central, Monterey, California
GCM	general circulation model
GMT	Greenwich Mean Time
LHS	left hand side of the equation
MDR	manually digitized radar (data)
NCAR	National Center for Atmospheric Research, Boulder, Colorado
NMC	National Meteorological Center, Silver Spring, Maryland
NWP	numerical weather prediction
NWS	National Weather Service
PBL	planetary boundary layer
PDE	partial differential equation
PE	primitive equation
PSU	The Pennsylvania State University
RHS	right hand side of the equation
RMS	root mean square
SI	static initialization
SLP	sea level pressure
WAM	Warner, Anthes, and McNab, 1978 (a reference)

ACKNOWLEDGEMENTS

The author wishes to thank Richard J. Shaginaw for processing most of the data used in this thesis and for his helpful discussions on the overall synoptic situation, Susan A. Tarbell and Erih-Yu Hsie for helping to compile and analyze the observed rainfall data, Daniel Baldwin for programming the objective precipitation scoring method, Dr. Alan L. McNab for helping familiarize the author with the original initialization program and the NCAR computer system, and Daniel Keyser for reviewing portions of the manuscript.

The author wishes to thank his committee for their helpful discussions and constructive criticisms. Special thanks are due to Dr. Richard A. Anthes for providing the original omega equation program and for his numerous beneficial discussions and suggestions. The author extends his sincere appreciation to his advisor, Dr. Thomas T. Warner, for his patient guidance, continual encouragement, and countless discussions throughout the course of this work.

This research was made possible under Environmental Protection Agency Grant R805659-01 and National Aeronautics and Space Administration Grant NSG5205. The computer facilities of The Pennsylvania State University and the National Center for Atmospheric Research (NCAR), Boulder, Colorado, were used for this research. NCAR is sponsored by the National Science Foundation.

My attendance at the Graduate School of The Pennsylvania State University was under the auspices of the Air Force Institute of Technology. Finally, this work would not have been possible without

ACKNOWLEDGEMENTS (Continued)

the encouragement and understanding of my family, who endured many lonely nights and weekends.

1.0 INTRODUCTION

Perhaps the four most important events to influence meteorology in the twentieth century are:

(1) the development of the concept of a front,

(2) the development of a global rawinsonde network for the twice-daily sampling of the atmosphere,

(3) the invention of the electronic computer, and

(4) the use of earth-orbiting satellite platforms for the observation of the atmosphere.

Simultaneously, meteorologists have gained increased knowledge and insight into the physics of the atmosphere. All of this, coupled with the very rapid developments in computer technology, has led to an ever increasing interest in the mathematical modeling of atmospheric structures in general and in numerical weather prediction (NWP) in particular.

Primitive equation models of the atmosphere require initial conditions for the mass and momentum variables. The initial conditions are derived from a limited number of observations, particularly at synoptic times. Many observations which are available, including some at synoptic times, are not used to assist in defining the initial conditions. Additionally, most observations that are used contain errors. After a meteorological field is analyzed, it must then be interpolated vertically and/or horizontally to define the field at

the model grid points. This interpolation process also introduces errors. Therefore, the entire data analysis process introduces errors even though the process itself is essential for a model integration.

Once the model variables have been analyzed to the model grid points, it is usually desirable to balance the mass and momentum fields. Balancing means that the mass and momentum fields are made compatible with one another so that the nonmeteorological accelerations produced at the beginning of a forecast are minimized. Normally, balancing is accomplished by requiring that the mass and momentum fields initially obey some diagnostic relationship. Examples of diagnostic relationships include the geostrophic wind equation, the gradient wind equation, and the balance equation. An initialization procedure of this kind, i.e., one which uses data primarily from one time and that does not use the model equations for balancing, is known as a static initialization (SI).

For complex baroclinic models that contain complex parameterizations of diabatic, frictional, and radiational effects, it is usually difficult if not impossible to find simple but adequate diagnostic relationships between the mass and momentum fields. This fact has led to a new kind of initialization procedure known as dynamic initialization (DI). The distinguishing feature of DI is that the model equations themselves are used for the balancing step.

In a standard SI, the initial conditions are customarily nondivergent because of the diagnostic balance relationship usually employed. Although they are relatively simple, nondivergent initial conditions do not permit a model to initially forecast precipitation at the observed rate. Since mesoscale NWP models will be used

primarily for short-range (6- to 24-hour) forecasts, it is especially desirable for the model to accurately forecast the initial precipitation rate. If the initial precipitation rate is greatly underforecast, then the model probably will not forecast precipitation correctly for periods on the order of twelve hours because the model should not overforecast precipitation late in the 12-hour period.

A method of correcting this precipitation rate problem, previously employed primarily on the synoptic scale, has been the addition of a divergent component to the nondivergent initial conditions. Normally, this procedure consists of using the omega equation to get vertical velocities. Then the continuity equation with appropriate boundary conditions is solved to get the velocity potential and the divergent wind field. The divergent wind component is then added to the nondivergent initial conditions. Generally, results with this technique on the synoptic scale have produced little change over results based on nondivergent initial conditions. The objective of this thesis is to study how the divergent wind component can be incorporated in a static initialization on the mesoscale in such a way as to improve the initial forecast precipitation rate. This should in turn improve the model's forecast precipitation amounts for varying time periods.

1.1 Review of the numerical model initialization problem

Development of initialization techniques has paralleled the development of numerical models themselves. Therefore, it is

appropriate to review briefly the history of NWP before discussing initialization.

1.1.1 Brief history of numerical weather prediction

The discovery leading to modern NWP was the realization that the forecast problem can be treated mathematically as an initial value-boundary value problem for the nonlinear partial differential equations which govern atmospheric motion. L. F. Richardson (1922) was the first to apply this idea. Richardson encountered several problems which we are careful to avoid today. One of the problems that led to his failure was the use of observed rather than balanced data. The resultant large-amplitude nonmeteorological waves destroyed the meteorological forecast. Additionally, since computers were not yet invented, a large amount of time was required for the calculations. Richardson's failure resulted in a lack of interest in NWP that lasted about 25 years.

Renewed interest in NWP occurred in the late 1940's. By then the use of rawinsondes made more accurate and more spatially and temporally numerous observations available. Also, the electronic computer had been invented. Simple "filtered" models, which eliminated the large-amplitude fast moving waves (and thus permitted larger time steps) that destroyed Richardson's forecast, were developed.

As computer size and speed increased, primitive equation (PE) models came into use because they permit greater flexibility. Gravity-inertia waves, which are meteorologically important in the atmosphere,

are allowed to exist in PE models. The philosophy is that the model which most closely resembles the atmosphere will best forecast the atmosphere. However, this added flexibility requires much greater care in the formulation of the initial conditions. One aspect of that formulation is addressed in this thesis.

Improved numerical forecasts are hampered by three constraints (Haltiner and Williams, 1975):

(1) The temporally and spatially continuous atmosphere must be represented by data at discrete points. Therefore, the entire spectrum of atmospheric motions cannot be resolved. In addition, numerous problems arise due to the approximation of derivatives by finite differences.

(2) We do not completely understand the physics of the atmosphere. Processes which make important contributions to the evolution of the atmosphere are not adequately represented. Also, computers are limited in terms of their size and speed in spite of the very rapid advances in computer technology.

(3) Inappropriate specification of the initial conditions will limit forecast accuracy because a numerical forecast is an initial value problem.

Dutton (1976) pointed out that even if the initial conditions are perfect, the model's ability is limited because imperfectly handled nonlinear interactions lead to forecast error growth.

Nonlinear interactions produce unresolvable wavelengths which erroneously appear on the grid at resolvable scales (this phenomenon is called aliasing). Because the nonlinear interactions are always there, the error increases with each time step. Lorenz (1965) stated that the difference between the forecast and actuality will eventually be that of two random states for the appropriate time of day and year.

1.1.2 Stages of the initialization process

The initialization problem has defied easy solution. The basic stages of the process for grid-point models are:

(1) observation,

(2) analysis to grid points, and

(3) balancing the mass and momentum fields.

The first stage has often been a problem because the observation density is usually low. The observations also contain human and instrumental errors as well as information on unresolvable scales.

The second stage consists of interpolation from observation locations to grid-point locations and to a fixed time. Cressman (1959) stated that interpolation should

(1) ensure internal consistency among variables,

(2) reduce observation errors, and

(3) smooth subgrid-scale features.

The third stage in the initialization process can be crucial. Thompson (1961) noted that large-scale accelerations are due primarily to small differences between forces. That is, the net accelerations are 10 percent of the magnitude of the individual accelerations. Therefore, to determine the accelerations within 10 percent, the wind and horizontal pressure gradient force must be known within 1 percent. This accuracy has not been attainable with most present-day observations so observed data cannot be used directly as initial conditions.

A dynamic balance may be defined as follows: mass (temperature and pressure) and momentum fields are compatible (in "balance") when the only accelerations produced by the mass and momentum fields generate features of meteorological importance. When an imbalance exists between the mass and momentum fields, the atmosphere tends to reduce the incompatibility through a mutual adjustment process. The theory of this process has been developed by Rossby (1938), Cahn (1945), and Washington (1964), among others. This theory, called the geostrophic adjustment theory, predicts that on the mesoscale, the wind field dominates the height field in the adjustment process.

One of the mechanisms which accomplishes the adjustment process is the gravity-inertia or gravity wave. A gravity wave is a wave driven by the force of gravity which can redistribute mass and kinetic energy. Gravity waves that are generated by imbalances in the initial state traverse and then leave the domain and hence usually do not have a major influence on the forecast after 12 to 24 hours. However, unrealistic pressure fluctuations and accompanying vertical motions can completely obscure meteorologically important motions during the

first twelve hours (Sasaki, 1969; Haltiner and Williams, 1975). This fact has made short-term forecasting difficult. If the model initial conditions have not been balanced to an adequate degree, the meteorologically important part of the forecast can be permanently and adversely altered by the model's response to the initial imbalance.

Incompatibility between the mass and momentum fields can be generated in many ways:

(1) errors are contained in the observations,

(2) observations have contained information on scales of motion not represented,

(3) interpolations, both vertical and horizontal, have reduced the balance, and

(4) a balanced state in the atmosphere does not necessarily correspond to a balanced state in the model because of the numerous approximations contained in the model.

As an example of (4), Nitta and Hovermale (1967) pointed out that boundary conditions and finite difference methods employed in the numerical formulation of the model atmosphere can produce gravity-inertia waves.

1.1.3 Balancing of the mass and momentum fields in PE models

The purpose of balancing is to reduce the generation of nonmeteorological gravity-inertia waves without altering the meteorologically important motions. Unfortunately, the balanced state

for complicated models that include friction, cumulus convection, radiation, etc., is usually unknown.

There are two common and several less common types of balancing methods (Bengtsson, 1975; Baer, 1977). The types of balancing methods are:

(1) static initialization (SI),

(2) dynamic initialization (DI),

(3) initialization by statistical methods,

(4) initialization utilizing dynamical integral constraints, and

(5) normal mode initialization.

They can be summarized as follows:

(1) SI. In a static initialization (SI), information applicable primarily at one time is used. Time derivatives in the equation of motion are usually neglected to get a diagnostic approximation to the balanced state. Examples of diagnostic relationships that have been used are the geostrophic wind equation, the gradient wind equation, and the balance equation.

(2) DI. The other common balancing method has been dynamic initialization (DI). In DI, the actual model equations are used complete with time derivatives. A DI may utilize data from one time only. However, some DI techniques employ data from two or more times. In this type of DI, sometimes called four-dimensional data assimilation, a preforecast integration, usually forward in time, is performed.

(3) Initialization by statistical methods. The National Meteorological Center (NMC) of the National Weather Service (NWS) has

used no separate initialization for their operational 6-level PE model. The forecast is started directly from the products of the objective analysis. The model is initialized with analyzed geopotentials, analyzed nondivergent winds, and 12-hour forecast divergent winds. This procedure was adopted because the short-range forecast errors were smaller than when the balance equation was used.

(4) Initialization with dynamic integral constraints. To minimize noise, the initial analyses can be adjusted to each other such that they satisfy some given equation(s). The most successful approach has been that of Sasaki (1958) which is based on the calculus of variations. First, for each meteorological variable, the difference between adjusted and observed quantities at a point is expressed as a sum of squares. Then the integral over the volume of all the sums of squares is minimized such that a given constraint is satisfied. This method's major drawback has been its complexity.

(5) Normal mode initialization. First, the normal modes of response for the model to be initialized must be determined. For example, a simple baroclinic model may have one fast external gravity-inertia wave mode and one slow internal gravity-inertia wave mode. The observations are then resolved into a series expansion of the normal modes in such a way as to detect the fast and slow modes. Then the coefficients of the fast modes are set equal to zero. With this method, the initial vorticity field is presumed correct and the corresponding geopotential and divergence fields that would eliminate high-frequency noise are found. This initialization technique is extremely complex, time consuming, and is just beginning to be used.

1.2 Previous research on the initialization of PE models

1.2.1 Historical review of initialization

The early work on initialization consisted primarily of replacing subjective techniques for the analysis of observations to grid points by objective analysis. The first objective initialization technique was due to Panofsky (1949). Panofsky approximated wind and pressure observations by third-degree polynomials requiring 10 coefficients. Boundaries and data-sparse regions were difficulties encountered with this method.

The successive correction type of objective analysis was first introduced by Bergthórsson and Döös (1955). First-guess values of geopotential were obtained. These values were then corrected by geopotential and wind observations in one additional scan over the grid.

Cressman (1959) also employed the successive correction method of objective analysis. He made several passes with an increasingly small radius of influence. Because of the method's simplicity and its applicability to most atmospheric variables, even in data-sparse regions, it was the primary analysis tool of the NWS until its replacement in 1974.

As models became more sophisticated, research on balancing became more important. One of the earliest studies of mass-momentum balancing was by Hinklemann (1951). Using a linear barotropic model, he showed that the amplitude of the undesired gravity-inertia waves was reduced by replacing the observed winds with geostrophic winds.

Charney (1955) utilized the balance equation to obtain geopotentials from the wind field. Using a primitive equation model and artificial winds, he showed that the generation of large amplitude gravity-inertia waves was greatly suppressed when geostrophic winds were replaced by balanced winds.

1.2.2 Dynamic initialization

Dynamic initialization was first studied by Nitta and Hovermale (1967). To balance the mass and momentum fields, the initial conditions on mass and momentum were forecast one time step forward followed by one time step backward. Then the mass or momentum field was restored to its initial value. The cycle was repeated numerous times. The resulting gravity-inertia waves were damped by the Matsuno (1966) time differencing scheme. It was shown that the model equations could be used to achieve balanced initial conditions.

A dynamic initialization technique was also studied by Hoke and Anthes (1976). In this technique, a 12-hour pre-forecast integration is performed in which the model variables are nudged toward the observed value of the variables at each grid point and time step. Subsequent 12-hour forecasts were better than those forecasts started from a SI. However, this kind of DI had disadvantages. First, it required additional computer time (in this case 24 hours of simulated time for a 12-hour forecast). Second, at the end of the pre-forecast integration, the model variables have not necessarily been close to the known grid point values.

Temperton (1976) performed experiments in dynamic initialization with a 5-level hemispheric model. The model was run 10 days to achieve a balanced state which was considered the control run. Temperton found that external gravity waves led to smaller forecast rain amounts than occurred without external gravity waves. Additionally, he found that dynamic initialization yielded smaller rain amounts than the control. Temperton showed that external gravity waves should be rapidly damped by DI while the low frequency internal modes are relatively unaffected.

1.2.3 Normal mode analysis and initialization

Phillips (1960) and Blumen (1975) have suggested incorporating the model's normal modes of response into the initialization process. Flattery (1970) employed Hough functions in his analysis scheme in which atmospheric data are expanded in terms of the Rossby modes of free oscillation of the shallow fluid equations. This implied that no gravity-inertia waves should be generated in an exact integration of the linear equations.

Dickinson and Williamson (1972) suggested linear normal mode initialization and determined the normal modes of a 2-level model based on the shallow fluid equations expanded in terms of spherical harmonics. Williamson (1976) then applied a normal mode initialization to a shallow water grid-point model. He found reduced gravity-inertia oscillations in nonlinear integrations but the gravity-inertia waves were not eliminated.

Williamson and Dickinson (1976) determined the normal response modes (vertical and latitudinal) for the linearized National Center for Atmospheric Research (NCAR) general circulation model (GCM). The ensuing integrations were found to contain less noise.

Machenhauer (1977) and Baer (1977) have extended normal mode initialization to include nonlinearity. Machenhauer first determined the free normal modes of a spectral, hemispheric, shallow fluid model. He then determined which nonlinear interactions between normal modes lead to gravity-inertia waves. The time derivative for the normal mode coefficients for unwanted modes was set to zero. Machenhauer also stated that normal mode initialization produced significant changes in the forecasts and is complicated and time consuming. Another disadvantage of this type of initialization has been that if the model is changed, the normal response modes are changed, and the model normal modes must be reanalyzed.

Baer (1977) applied normal mode initialization by allowing nonlinearity to affect the initial conditions in such a way as to eliminate gravity-inertia waves in the initial conditions and prevent most of them from occurring during the time integration. Baer assumed the initial vorticity was accurate. He then adjusted the geopotentials and divergence so they were compatible with the vorticity field. In effect, the high-frequency waves (external gravity and fastest internal gravity waves) were eliminated. However, the slower gravity-inertia modes have speeds comparable to Rossby modes and were not affected.

Baer and Tribbia (1977) extended Baer's (1977) technique to any prediction model of a planetary fluid of reasonably small Rossby number.

1.2.4 Geostrophic adjustment

Geostrophic adjustment was discussed briefly in Section 1.1.2. However, Økland (1970) reached some conclusions which are important to this work and they will be presented here.

Økland found a linear solution to a simple linear baroclinic model for given initial conditions. The solution consisted of two parts: (1) high-frequency gravity-inertia waves, and (2) low-frequency gravity-inertia waves which effect a balance between the mass and momentum fields. Økland believed that the solution to the general analogous initial-value problem, if it could be derived, would consist of two parts; the one being high-frequency gravity-inertia waves and the other the balanced mass and wind fields which exhibit much lower frequency.

Økland stated that gravity waves may be suppressed by damping or propagation away from the area of interest. A damping integration scheme such as the Euler-backward scheme could be used but the slower internal gravity waves move at about the same speed as the Rossby modes. Hence damping the slower gravity-inertia waves would also damp the waves of interest. Dispersion of the wave energy from the source would be effective for waves with high group velocities. If the initial data created waves of small group velocity, then those waves would

disperse slowly and the adjustment would be slow, a situation to be avoided. In contrast with baroclinic models, barotropic models of deep motions contain only one mode and it is fast (an external gravity wave with a speed of about 300 m s^{-1}). Therefore, the adjustment in barotropic models is relatively rapid.

Økland conducted two experiments with a 2-level baroclinic model. The model was allowed to run for 24 hours. Experiment I was the next 24 hours of the forecast. In Experiment II, the divergence was removed from the initial conditions before the second 24-hour forecast was begun. He plotted the root-mean-square (RMS) values of the local rate of change of surface pressure and the RMS values of omega (the vertical velocity in pressure coordinates) at about 500 mb. The pressure curves were more indicative of external gravity wave activity. Gravity wave activity can be visualized as the effect of all gravity waves simultaneously acting to modify the balance between the mass and momentum fields. This activity was greatest for the nondivergent initial conditions (Experiment II). The RMS omega graphs were more indicative of the internal gravity-inertia wave activity. This activity contained less noise in the case that contained the divergence (Experiment I).

1.2.5 Balancing on sigma versus pressure surfaces

Most PE models today employ pressure or normalized pressure (sigma) as the vertical coordinate. Reasons include: upper air data are reported on standard pressure levels; density does not appear explicitly

in the model equations; and, the boundary conditions at the ground are easier to formulate. The mesoscale model developed at Penn State (see, e.g., Anthes and Warner, 1978, hereafter referred to as AW) uses the sigma coordinate system. In the initialization of this model, geopotentials are calculated on pressure surfaces. Balanced temperatures are then derived and the winds and temperatures are interpolated to the model sigma surfaces.

Since the nonlinear balance equation has been used, the model initial conditions have been nondivergent and the initial vertical velocity (omega) at each grid point should have been zero. However, Warner et al. (1978, hereafter referred to as WAM) reported that small omega values on the order of 10 mb d^{-1} are introduced on the sigma surfaces in the interpolation from pressure to sigma surfaces. In other words, the initial balance has been altered. These omega values on sigma surfaces are largest where terrain slopes are greatest and hence have not necessarily corresponded to meteorological features. Since the model-generated omega values were much larger, the small initial omega values have not been considered to be a problem.

An alternative approach has been to interpolate the model variables to sigma surfaces prior to balancing. Sundqvist (1975) interpolated observed geopotentials to sigma surfaces and then used the nonlinear balance equation to calculate the stream function on sigma surfaces. He used a hemispheric five-level model with a grid length of 300 km at 60°N. His scale analysis of the divergence equation in sigma coordinates indicated that the nonlinear balance equation was appropriate for his model. The initialization on sigma surfaces

reduced initial gravity-inertia wave oscillations when compared with initialization on pressure surfaces and interpolation to sigma surfaces. However, an initialization on sigma surfaces with orography included produced more gravity-inertia wave oscillations than an initialization with no terrain.

1.2.6 Effect of divergent initial conditions

Phillips (1960) pointed out that the removal of gravity-inertia waves from even simple models is not just a matter of specifying initial geostrophic or nondivergent flow. Small values of divergence were actually needed in the initial conditions to suppress these waves. To specify the initial divergence in baroclinic models, Phillips proposed various forms of the geostrophic omega equation. The adiabatic geostrophic omega equation relates vertical motion to the advection of temperature and vorticity.

Warner (1972) initialized jets in barotropic channel and hemispheric models. He used the following initializations:

(1) geostrophic,

(2) mass field in balance with the fully divergent wind field,

(3) mass field in balance with the nondivergent wind field,

(4) quasi-gradient, and

(5) backward-forward integration about the initial time (a type of DI).

The geostrophic initialization was clearly inferior as curvature is neglected. The most important finding relevant here was that the initializations including divergence in the initial conditions ((2) and (5)) produced the least gravity-inertia wave noise.

1.2.7 Previous divergent initialization techniques and their effect on precipitation predictions

The initialization of the divergent component (hereafter referred to as divergent initialization) has been attempted by several researchers. Houghton et al. (1971) obtained omega values from a diagnostic equation similar to the omega equation. Their omega equation did not contain a diabatic term. The coarse-mesh grid used had grid points at five degree intervals in latitude and longitude. The divergent initial conditions had a small effect on the dynamic variables at first, no effect after 12 hours, and the same level of noise as the nondivergent initial conditions. The initial conditions were not saturated where vertical motion was present and the effect of divergent initialization on precipitation was not evaluated. They stated that it may be that poor model resolution of the small scales inherent in the vertical motion field contributed significantly to the lack of forecast improvement.

Lejenäs (1977) used the quasi-geostrophic omega equation without a diabatic term to obtain omega fields on a coarse-mesh grid (grid increment 300 km). The continuity equation was then used along with a relaxation procedure to convert the omega values to velocity

potentials. After adding the divergent component to the initial conditions, he found a higher precipitation rate than the nondivergent forecast for the first four hours, a lower precipitation rate from 4 to 10 hours, and the same noise level as nondivergent initial conditions. The moisture field initially was not saturated. The effect of divergent initialization on the dynamic variables was not reported. Although the precipitation forecast was more realistic, it was significantly less than the observed precipitation. We would expect that after the model has reached a balanced state internally, the initial divergent component would no longer be important. Instead the model would have produced a divergent component compatible with the model's nondivergent component.

Dey and McPherson (1977) initialized the divergent component in the NMC coarse-mesh hemispheric PE model. The initial balanced state was derived from observations. The divergent component was derived from a model forecast valid at the same time. A vertical velocity equation was not used. Dey and McPherson had thought that divergent initialization might be beneficial if applied over several forecast cycles, but the divergent initialization caused only small changes in both the global analyses and forecasts. The only differences in the precipitation forecasts occurred in areas of very light precipitation and therefore the significance was difficult to assess. They concluded that divergent initialization neither degraded nor improved the performance of the NMC global system. Additionally, Dey (personal communication) reported that a forecast divergent component that was applicable 5 days before the initialization time was inadvertently

added to balanced initial conditions in one experiment and no significant change in the forecast resulted.

Lubeck et al. (1977) have performed divergent initialization experiments with a global spectral model. They concluded that the divergent initialization had a relatively small effect on the forecast dynamic variables. A semi-implicit integration scheme was used to smooth the high frequency oscillations. Orography was not included in the experiments. Also, the model was dry and therefore the effect of the divergent initialization on precipitation could not be evaluated.

Smagorinsky et al. (1967) did experiments with a global 9-level PE model. They used a form of the omega equation with no diabatic term. The experiments started with a divergent initialization produced almost the same precipitation as forecasts started from nondivergent initial conditions.

Benwell et al. (1971) used a 10-level PE model for divergent initialization experiments. They reported slightly larger precipitation amounts with nondivergent initial conditions.

Divergent initialization has also been used in hurricane models. In hurricanes, the divergent part of the wind is large and forecasts beginning with the total wind have been more successful than those started from the nondivergent component only. Miller et al. (1972) obtained the stream function and then temperatures were derived. The quasi-geostrophic omega equation with a diabatic term was solved for omega values which are in turn used in the continuity equation to obtain velocity potentials (presumably the relaxation boundary condition was one of constant velocity potential). The total wind was obtained by

combining the divergent and nondivergent parts. Temperatures and winds were then forecast. From that forecast, the time dependent terms in the complete divergence and omega equations could be evaluated. The heights, temperatures, and omega values were recalculated. The process was repeated until the heights and omega fields were relatively stable. This process was similar to DI. The areal extent of their precipitation forecasts agreed with the observed rainfall. However, the forecast precipitation amounts were too low. The model atmosphere was not saturated initially and the forecast model did not contain a convective precipitation parameterization. The adequacy of the initial precipitation rate was not evaluated.

Mathur (1974) used an omega equation similar to the quasi-geostrophic omega equation but it did not contain a diabatic term. The omega values were then used in the continuity equation to obtain velocity potentials. Again, presumably a constant value was used as the boundary condition on the velocity potential. The meshed grid increments were 37 km on the interior and 74 km on the exterior. The hurricane studied occurred entirely over the ocean and observed precipitation fields were not available.

In summary, there has been a lot of work on the various aspects of the initialization problem. The work to date on divergent initialization has been primarily on the large or synoptic scale. On that scale, the divergent initialization has had little if any effect on the forecast. The divergent initializations on the mesoscale have been for hurricane models. The resulting forecasts were evaluated by comparing forecast versus observed track and intensification. The

adequacy and suitability of the divergent initializations as compared with nondivergent initializations were not evaluated. The effect of divergent initialization on precipitation forecasts was not closely scrutinized. Finally, diabatic heating information and asynoptic data were not utilized in the initialization schemes.

1.3 Synoptic scale versus mesoscale divergence values

Before any further discussion of the differences between the synoptic and mesoscales, we will present a more quantitative definition of the scales. In Table 1, we adopt Orlanski's (1975) scale definitions but we have subdivided the meso-β scale into upper and lower portions. In subsequent sections, synoptic scale will refer to meso-α and larger scales and the term mesoscale will refer to the upper meso-β scale unless otherwise noted.

Table 1. Scale Definitions.

Scale designation	Scale range (km)
meso-γ	2-20
meso-β	20-200
lower meso-β	20-60
upper meso-β	60-200
meso-α	200-2000
macro-β	2000-10000

As discussed in Section 1.2, divergent initialization on the synoptic scale had little if any influence on the precipitation forecasts. We will now attempt to gain some insight into why divergent initialization has not been successful on the synoptic scale but might be successful on the mesoscale and smaller scales. Let V be a characteristic velocity and Δx a characteristic horizontal model grid increment. For the scales in Table 1, 10 m s^{-1} is a characteristic velocity. For characteristic grid increments, let us compare a synoptic model grid increment Δx_1 = 300 km, an upper meso-β scale grid increment Δx_2 = 100 km, and a lower meso-β scale grid increment Δx_3 = 30 km. We can now compare typical divergence values for the three different grid increments.

We know from the divergence theorem that the net divergence over the global 500-mb surface is zero. We would expect the same result to be approximately correct for a hemisphere. In fact, as we will discuss in more detail in Chapter 2, the net divergence on a constant pressure surface over an area of about 3500 km on a side averages almost to zero. However, at grid increments on the order of Δx_3, there exist phenomena such as thunderstorms that possess large divergences. These divergence patterns could easily dominate over a small grid and produce large net divergence at a given level.

Since V is the same for each length scale, and since divergence is of order $V/\Delta x$, we expect an order of magnitude larger divergence values as we progress from Δx_1 to Δx_3. The grid increments Δx_1, Δx_2, and Δx_3 each differ by a factor of three but the area contained within each grid square is almost an order of magnitude different. That is,

$(\Delta x_1)^2 \sim 10^5$ km^2, $(\Delta x_2)^2 \sim 10^4$ km^2, and $(\Delta x_3)^2 \sim 10^3$ km^2. Therefore, we can visualize a much larger net divergence over an area $(\Delta x_3)^2$ than over an area $(\Delta x_1)^2$.

Thus, the divergence at a grid point can be larger in mesoscale models than in synoptic scale models. Because divergence is the forcing function in the Poisson equation for velocity potential (and hence the divergent component), we expect a mesoscale divergent component of greater magnitude than on the synoptic scale. In other words, the divergent component may well be a significant ingredient in mesoscale model initial conditions while previous research has indicated that it is not significant in that respect on the synoptic scale. We will accomplish a scale analysis in Chapter 2 to see how significant the divergence can be expected to be on the mesoscale but we have demonstrated here in qualitative terms that, if divergent initialization is to significantly affect a precipitation forecast, it would most likely occur on the mesoscale and smaller scales.

1.4 Research objectives

To date, precipitation forecasting with NWP models has not been very accurate, especially in cases of significant precipitation. Accurate and timely precipitation forecasts on the mesoscale would be of great economic and other value in times of flash floods, squall lines, heavy precipitation over large areas such as hurricanes, etc. Therefore, a divergent initialization procedure which improves mesoscale NWP model precipitation forecasts would be an important contribution.

A general divergent initialization procedure developed in this thesis can be described as follows: a vertical velocity equation diagnoses vertical velocities from observed meteorological fields. Velocity potentials are then derived from the vertical velocities with the continuity equation and knowledge of appropriate boundary conditions on velocity potential. Next, the divergent wind components are obtained from the velocity potential. Geopotentials are calculated on sigma surfaces using a balance equation with contributions from both the nondivergent and divergent wind components. Finally, balanced temperatures are derived via the hydrostatic equation. Note that the vertical velocity and divergence fields are diagnosed. We cannot accurately measure divergence directly because the errors in the wind observations are on the order of magnitude of the divergent wind component. Therefore, we derive a vertical velocity equation that defines what vertical velocity field would exist for a given set of dynamic and thermodynamic variables.

Questions to be addressed in this thesis include:

General:

(1) What are the differences between divergent initialization on the synoptic and mesoscales?

(2) Does the inclusion of a divergent component on the mesoscale improve the ensuing forecast, especially precipitation rate and amount? Analogously, does the model remember the divergence as introduced by the initialization?

(3) Do modeled precipitation systems recover their "correct" intensity later in the forecast, after a nondivergent initialization, or are the precipitation rates throughout the forecast adversely affected by the incorrect vertical velocities and latent heat release produced early in the forecast by the lack of initial divergence?

(4) What form of the omega and balance equations should be used on the mesoscale?

Specific:

(5) Can the vertical velocities be diagnosed to sufficient accuracy to be useful in the divergent initialization procedure?

(6) What boundary conditions should be used on stream function, omega, and geopotential?

(7) The continuity equation is used to derive velocity potential from vertical velocity. How should the boundary conditions on velocity potential be specified to achieve maximum accuracy on the domain interior?

The forecast model that will be used for these experiments is the mesoscale NWP model developed at The Pennsylvania State University (see WAM, AW). In Chapter 2 a scale analysis of the relevant equations as well as a thorough analysis of the appropriate boundary conditions for the required dependent variables will be provided. In Chapter 3, a brief description of the forecast model will be given. The data at the initial and final synoptic times, the observed precipitation, and

a discussion of the synoptic situation chosen for study will be presented in Chapter 4. In Chapter 5, we will develop the finite-difference form of the omega equation which will be used to determine vertical velocities. The omega equation will then be applied to the data set. In Chapter 6, the finite-difference form of the balance equation will be derived from the model equations. In Chapter 7, the finite-difference balance equation will be applied to the chosen data set. Chapter 8 will contain the summary and conclusions.

2.0 DEVELOPMENT OF THE DIVERGENT INITIALIZATION PROCEDURE

In this chapter, we will first state which forces are considered in the forecast model developed at The Pennsylvania State University (PSU). Then we will perform a scale analysis of the complete vertical velocity and divergence equations. These scale analyses will specify which terms must be retained in the respective equations for use in the specific divergent initialization procedure. Finally, we will examine which boundary conditions should be employed for the various second-order elliptic partial differential equations (PDEs) which arise in this scheme. We shall see that the proper specification of boundary conditions is important to this initialization procedure. The general framework for the divergent initialization procedure will be outlined whereas the specific technique for the initialization of the PSU model will be addressed in later chapters.

Before we can perform the required scale analyses, we need to know what forces are considered by the PSU model. That is, we need to know what form of the equation of motion is used so that we can derive consistent vertical velocity and divergence equations. The PSU model considers the pressure gradient force, the Coriolis force, gravity, and the vertical frictional force in the planetary boundary layer (PBL) only. Additionally, horizontal frictional forces are used by the model at every level, but for numerical rather than physical reasons.

2.1 Scale analysis of the vertical velocity equation

Scale analysis is a technique which permits the determination of what terms in a given equation are important, based on characteristic values of physical variables and characteristic scales in space and time of the class of phenomena of interest. Here, we are interested in the upper meso-β and larger scales (e.g., baroclinic waves).

The scale analysis presented here, through (2.19), closely follows that of Williams (personal communication). We define

L = characteristic horizontal scale (roughly a quarter wavelength of the disturbances considered)

T = characteristic time scale

V = characteristic horizontal velocity

The approximate magnitudes of derivatives can be estimated as follows:

$$\frac{\partial u}{\partial x} \sim \frac{\partial v}{\partial y} \sim \frac{V}{L} \quad , \tag{2.1a}$$

$$\frac{\partial u}{\partial t} \sim \frac{V}{T} \quad . \tag{2.1b}$$

The time scale is generally given by

$$T \sim \frac{L}{V} \quad . \tag{2.2}$$

Here we will use $V \sim 10$ m s^{-1} for the synoptic and mesoscales, $L \sim 1000$ km for synoptic-scale motions and $L \sim 100$ km for mesoscale features.

The Helmholtz theorem states that a velocity vector can be separated into nondivergent and divergent (irrotational) parts:

$$\underset{\sim}{V} = \underset{\sim}{V}_{\psi} + \underset{\sim}{V}_{\chi} \tag{2.3}$$

where

$$\underset{\sim}{V}_{\psi} = \hat{k} \times \nabla\psi \tag{2.3a}$$

and

$$\underset{\sim}{V}_{\chi} = \nabla\chi \quad . \tag{2.3b}$$

In (2.3a) and (2.3b), ψ is the stream function and χ is the velocity potential. Since we know that the magnitude of the nondivergent wind is on the order of the observed wind for the scales (upper meso-β and larger) considered, we use

$$V_{\psi} \sim V \tag{2.4}$$

for the scale of the nondivergent wind. On the other hand, the divergent wind is generally an order of magnitude smaller. Therefore, we use

$$V_{\chi} \sim R_1 V \tag{2.5}$$

where $R_1 \sim 0.1$, but for the upper meso-β and larger scales of motion which we consider here, R_1 could be as small as zero or as large as 0.3.

In addition to those scaling parameters, we will use

$$\nabla \sim \frac{1}{L} \quad , \tag{2.6a}$$

$$Ro = \frac{V}{fL} \quad \text{or} \quad f = \frac{1}{Ro}\frac{V}{L} \quad , \tag{2.6b}$$

$$D \sim R_1 \frac{V}{L} \quad , \tag{2.6c}$$

$$\zeta \sim \frac{V}{L} \quad , \tag{2.6d}$$

and

$$\beta = \nabla f = \frac{df}{dy} = 2\Omega \cos \phi \frac{d\phi}{dy} \sim \frac{f}{a} \tag{2.6e}$$

for mid-latitudes. If the wind were geostrophic, then

$$\nabla\phi \sim fV \quad . \tag{2.6f}$$

Now we separate the geopotential into two parts.

$$\phi = \bar{\phi}(z) + \phi' \tag{2.6g}$$

In (2.6g), ϕ' is the perturbation geopotential and $\bar{\phi}(z)$ is taken from the standard atmosphere. With (2.6a), (2.6f), and (2.6g), we obtain (2.6h).

$$\frac{\phi'}{L} \sim fV \quad \text{or} \quad \phi' \sim fVL \tag{2.6h}$$

Even though the wind is not geostrophic on the upper meso-β scale, (2.6h) is adequate for scaling purposes.

2.1.1 Pertinent equations in Z coordinates

We utilize the vertical coordinate Z which was first used by Phillips (1963):

$$Z \equiv - \ln\left(\frac{p}{p_o}\right) \quad . \tag{2.7}$$

Z is related to actual height, h, and geopotential ϕ by the equation of state and the hydrostatic equation:

$$RT = p\alpha = - pg \frac{\partial h}{\partial p} = \frac{\partial \phi}{\partial Z} \quad . \tag{2.8}$$

From (2.8) we see that

$$- p \frac{\partial}{\partial p} = \frac{\partial}{\partial Z} \quad . \tag{2.9}$$

One advantage of Z is that it approximately equals the actual height divided by the scale height. That is,

$$Z \sim \frac{h}{H} \tag{2.10}$$

where $H = RT/g$ is the scale height. For the atmosphere, $H \sim 8$ km. Therefore, for the troposphere,

$$Z \sim 1 \tag{2.10a}$$

and

$$\frac{\partial}{\partial Z} \sim 1 \quad . \tag{2.10b}$$

From (2.7) we see

$$\dot{Z} = -\frac{\dot{p}}{p} = -\frac{\omega}{p} \quad . \tag{2.11}$$

The horizontal vector equation of motion in Z coordinates which contains the forces considered by the PSU model is

$$\frac{\partial \underset{\sim}{V}}{\partial t} + \underset{\sim}{V}\cdot\nabla\underset{\sim}{V} + \dot{Z}\,\frac{\partial \underset{\sim}{V}}{\partial Z} + \nabla\phi + f\hat{k} \times \underset{\sim}{V} - \underset{\sim}{Fr} = 0 \quad . \tag{2.12}$$

The continuity equation in p coordinates is

$$\nabla\cdot\underset{\sim}{V} + \frac{\partial \omega}{\partial p} = 0 \quad . \tag{2.13}$$

Using (2.11) and (2.9) to modify (2.13), we obtain the continuity equation in Z coordinates:

$$\nabla\cdot\underset{\sim}{V} + \frac{\partial\dot{Z}}{\partial Z} - \dot{Z} = 0 \quad . \tag{2.14}$$

With the hydrostatic equation, the first law of thermodynamics can be written

$$\frac{\partial}{\partial t}\frac{\partial\phi}{\partial Z} + \underset{\sim}{V}\cdot\nabla\frac{\partial\phi}{\partial Z} + \dot{Z}\frac{\partial}{\partial Z}\left(\frac{\partial\phi}{\partial Z} + \kappa\phi\right) = \kappa Q \tag{2.15}$$

where $\kappa = R/c_p$ and Q is the heat added per unit time and mass.

2.1.2 Derivation of the vertical velocity equation

To obtain a vertical velocity equation, we must first have a vorticity equation. Operating on (2.12) with ∇ x yields

$$\begin{aligned}&\frac{\partial\zeta}{\partial t} + \underset{\sim}{V}_\psi\cdot\nabla\zeta + \underset{\sim}{V}_\chi\cdot\nabla\zeta + \underset{\sim}{V}_\psi\cdot\nabla f \\ &\quad + \underset{\sim}{V}_\chi\cdot\nabla f + \dot{Z}\frac{\partial\zeta}{\partial Z} + fD + \zeta D \\ &\quad + \hat{k}\cdot\nabla\dot{Z} \times \frac{\partial\underset{\sim}{V}_\psi}{\partial Z} + \hat{k}\cdot\nabla\dot{Z} \times \frac{\partial\underset{\sim}{V}_\chi}{\partial Z} - \nabla \times \underset{\sim}{Fr} = 0 \quad .\end{aligned} \tag{2.16}$$

With (2.6g), (2.15) can be rewritten as

$$\frac{\partial}{\partial t}\frac{\partial \phi'}{\partial Z} + \underset{\sim}{V}_{\psi}\cdot\nabla\frac{\partial \phi'}{\partial Z} + \underset{\sim}{V}_{\chi}\cdot\nabla\frac{\partial \phi'}{\partial Z} + \dot{Z}\Gamma(Z)$$

$$+ \dot{Z}\frac{\partial}{\partial Z}\left(\frac{\partial \phi'}{\partial Z} + \kappa\phi'\right) - \kappa Q = 0 \qquad (2.17)$$

where

$$\Gamma(Z) = \frac{\partial}{\partial Z}\left(\frac{\partial \bar{\phi}}{\partial Z} + \kappa\bar{\phi}\right)$$

$$= R\left(\frac{\partial \bar{T}}{\partial Z} + \kappa\bar{T}\right) \qquad (2.18)$$

$$= \frac{H^2 g}{\bar{T}}\left(\frac{g}{c_p} + \frac{1}{H}\frac{\partial \bar{T}}{\partial Z}\right) \quad .$$

Γ is a static stability because it is proportional to the difference between the dry adiabatic lapse rate and the standard atmospheric lapse rate.

We derive the vertical velocity equation by operating on (2.16) with $f_o \frac{\partial}{\partial Z}$, subtracting ∇^2 of (2.17), and reordering terms:

$$\underset{T1}{\Gamma(Z)\nabla^2\dot{Z}} - \underset{T2}{f_o^2\frac{\partial D}{\partial Z}} + \underset{T3a}{\nabla^2\dot{Z}\frac{\partial}{\partial Z}\left(\frac{\partial \phi'}{\partial Z} + \kappa\phi'\right)}$$

$$= \underset{T4}{f_o\frac{\partial}{\partial Z}\underset{\sim}{V}_{\psi}\cdot\nabla\zeta} + \underset{T5}{f_o\frac{\partial}{\partial Z}\underset{\sim}{V}_{\chi}\cdot\nabla\zeta} - \underset{T6}{\nabla^2\underset{\sim}{V}_{\psi}\cdot\nabla\frac{\partial \phi'}{\partial Z}} \qquad (2.19)$$

Ia II Ia

$$- \nabla^2 \underset{\sim}{V}_\chi \cdot \nabla \frac{\partial \phi'}{\partial Z} + \kappa \nabla^2 Q + f_o \frac{\partial}{\partial Z} \dot{Z} \frac{\partial \zeta}{\partial Z}$$

T7 T8 T9

II I II

$$+ f_o \frac{\partial}{\partial Z} \nabla x \underset{\sim}{Fr} + f_o \frac{\partial}{\partial Z} \underset{\sim}{V}_\psi \cdot \nabla f + f_o \frac{\partial}{\partial Z} \underset{\sim}{V}_\chi \cdot \nabla f$$

T10 T11 T12

II III III

$$+ f_o \frac{\partial}{\partial Z} \zeta D + f_o \frac{\partial}{\partial Z} \hat{k} \cdot \nabla \dot{Z} \times \frac{\partial \underset{\sim}{V}_\psi}{\partial Z} + f_o \frac{\partial}{\partial Z} \hat{k} \cdot \nabla \dot{Z} \times \frac{\partial \underset{\sim}{V}_\chi}{\partial Z} \qquad (2.19)$$
(cont.)

T13 T14 T15

II II III

$$+ f_o \frac{\partial}{\partial t} \frac{\partial \zeta}{\partial Z} - \frac{\partial}{\partial t} \nabla^2 \frac{\partial \phi'}{\partial Z} \quad .$$

T16 T17

In the derivation of vertical velocity equations, it is usually assumed that the local rate of change of the actual vorticity equals the time rate of change of the geostrophic vorticity (hereafter called the geostrophic vorticity assumption), where the geostrophic vorticity is

$$\zeta_g = \frac{1}{f} \nabla^2 \phi \quad . \qquad (2.20)$$

We make this assumption here, and will return to it in Section 2.1.5.

2.1.3 Scale analysis of the vertical velocity equation

From the continuity equation (2.14), we obtain

$$\dot{Z} \sim R_1 \frac{V}{L} \tag{2.21}$$

since $D \sim R_1 \frac{V}{L}$.

Table 2 contains a scale analysis of (2.19) which includes a scaling factor for each forcing function. First, consider the synoptic scale, where $L \sim 1000$ km. For mid-latitudes, that implies $Ro \sim 0.1$. The value of C_D is taken to be ~ 0.001 (Anthes, 1978) and H is ~ 10 km. For this length scale, $L/a \sim 0.1$. We choose a precipitation rate of 0.1 cm h^{-1} as typical of a synoptic-scale grid square ($R_2 = 0.1$ in T8 in Table 2). Examination of the scale factors of (2.19) reveals that the forcing functions T4, T6, T8, and T11 are of order 10^{-14} while terms T5, T7, T9, T10, T12, T13, and T14 are an order of magnitude smaller. The largest forcing functions represent differential vorticity advection by the nondivergent wind, the Laplacian of temperature advection by the nondivergent wind, the diabatic term, and the beta or Coriolis term. These are important physical processes on the large scale. For divergent initialization on the large scale, the four largest forcing functions should be used in the vertical velocity equation. It should be noted that three of the four largest terms (T4, T6, and T11) are the forcing functions of the quasi-geostrophic vertical velocity equation. This is a well-known result (e.g., see Haltiner, 1971).

Table 2. Scale analysis of the forcing functions in the vertical velocity equation.

Term designator	Scale factor
T4	$T4 \sim \frac{1}{Ro}\frac{V}{L} V \frac{1}{L}\frac{V}{L} \sim \frac{1}{Ro}\frac{V^3}{L^3}$
T5	$T5 \sim R_1\, T4 \sim \frac{R_1}{Ro}\frac{V^3}{L^3}$
T6	$T6 \sim \frac{1}{L^2} Vf\, VL \sim \frac{1}{Ro}\frac{V^3}{L^3}$
T7	$T7 \sim R_1\, T6 \sim \frac{R_1}{Ro}\frac{V^3}{L^3}$
T8	Let R_2 be a precipitation rate of 1 cm h^{-1}. Then, for each cm^2, $R_2 = 1$ g h^{-1} $\sim$ 600 cal h^{-1} $\sim$ 2400 joule h^{-1} $\sim$ 1 joule s^{-1}. Therefore, $Q \sim R_2$ per unit mass in mks units and $T8 \sim \frac{\kappa R_2}{L^2} \sim \frac{R_1 R_2}{L^2}$
T9	$T9 \sim \frac{1}{Ro}\frac{V}{L} R_1 \frac{V}{L}\frac{V}{L} \sim \frac{R_1}{Ro}\frac{V^3}{L^3}$

Table 2 (Continued)

Term designator	Scale factor
T10	The model friction term in the bulk-PBL parameterization (see AW) can be scaled

$$\frac{Fr}{p_*} \sim \frac{g}{p_*}\frac{1}{\sigma}\frac{\partial \tau}{\partial Z} \sim \frac{g}{p_*}\frac{1}{\sigma}\frac{\partial}{\partial Z} p_s C_D V^2$$

$$\sim \frac{g}{RT}\frac{1}{\sigma} C_D V^2 \sim \frac{C_D V^2}{H}$$

Therefore, $T10 \sim \frac{1}{Ro}\frac{V}{L}\frac{1}{L}\frac{1}{H} C_D V^2 \sim \frac{1}{Ro}\frac{C_D}{H}\frac{V^3}{L^3}$

T11 $\quad T11 \sim \frac{1}{Ro}\frac{V}{L} V\beta \sim \frac{1}{Ro}\frac{f}{a}\frac{V^2}{L} \sim \frac{1}{Ro^2}\frac{L}{a}\frac{V^3}{L^3}$

T12 $\quad T12 \sim R_1\, T11 \sim \frac{R_1}{Ro^2}\frac{L}{a}\frac{V^3}{L^3}$

T13 $\quad T13 \sim \frac{1}{Ro}\frac{V}{L}\frac{V}{L} R_1 \frac{V}{L} \sim \frac{R_1}{Ro}\frac{V^3}{L^3}$

T14 $\quad T14 \sim T13 \sim \frac{R_1}{Ro}\frac{V^3}{L^3}$

T15 $\quad T15 \sim R_1\, T14 \sim \frac{R_1^2}{Ro}\frac{V^3}{L^3}$

T16 $\quad T16 \sim \frac{1}{Ro}\frac{V}{L}\frac{V}{L}\frac{V}{L} \sim \frac{1}{Ro}\frac{V^3}{L^3}$

T17 $\quad T17 \sim \frac{V}{L}\frac{1}{L^2} fVL \sim \frac{1}{Ro}\frac{V^2}{L^2}\frac{V}{L} \sim \frac{1}{Ro}\frac{V^3}{L^3}$

2.1.4 Determination of the mesoscale vertical velocity equation

On the mesoscale, L $\sim$ 1000 km. For mid-latitudes, that implies Ro $\sim$ 1 and L/a $\sim$ 0.01. We take a precipitation rate of 1 cm h^{-1} as being typical of a mesoscale grid square (R_2 = 1 in Table 2). Using these values, the relative order of magnitude of the forcing functions in (2.19) except for T16 and T17 is indicated in Roman numerals underneath the terms in (2.19). The largest forcing function is the diabatic term, T8, with a value of order 10^{-11}. Therefore, in areas where precipitation is occurring, the diabatic term dominates the other forcing functions on the mesoscale. Terms with a Ia (T4 and T6) are an order of magnitude smaller in precipitation areas. These terms represent differential vorticity advection and the Laplacian of temperature advection. Note that these terms will be the most important terms in areas where no precipitation is occurring. Terms with a II (T5, T7, T9, T10, T13, and T14) are of the same order but are an order of magnitude smaller than the terms with a Ia. Forcing functions with a III (T11, T12, and T15) are of the same order but are an order of magnitude smaller than the terms labeled II.

The goal of this research is to develop and test a divergent initialization technique on the mesoscale. Since the divergent component is an order of magnitude smaller than the nondivergent component on the mesoscale, and since we desire to diagnose the vertical velocities as accurately as possible, we will retain terms of first and second order and discard only those terms at least two orders of magnitude smaller than the most significant terms. That is,

we will keep terms labeled I, Ia, and II while discarding terms labeled III. Therefore, the final mesoscale vertical velocity equation consists of terms T1, T2, T3a, T4, T5, T6, T7, T8, T9, T10, T13, and T14 of (2.20) and will be referred to as (2.22).

The omega equation corresponding to (2.22) is

$$\nabla^2(\sigma_s\omega) + f\zeta_a \frac{\partial^2\omega}{\partial p^2} = f \frac{\partial}{\partial p} \underset{\sim}{V}_\psi \cdot \nabla\zeta$$

T1 T2 T3

I

$$+ f \frac{\partial}{\partial p} \underset{\sim}{V}_\chi \cdot \nabla\zeta + \frac{R}{p} \nabla^2 \underset{\sim}{V}_\psi \cdot \nabla T + \frac{R}{p} \nabla^2 \underset{\sim}{V}_\chi \cdot \nabla T$$

T4 T5 T6

II I II

$$- f \frac{\partial}{\partial p} \zeta D + f \frac{\partial}{\partial p} \omega \frac{\partial\zeta}{\partial p} + f \frac{\partial}{\partial p} \nabla\omega \cdot \nabla \frac{\partial\psi}{\partial p} \qquad (2.23)$$

T7 T8 T9

II II II

$$- \frac{R}{c_p p} \nabla^2 Q + f \frac{\partial}{\partial p} g \frac{\partial}{\partial p} \nabla \times \underset{\sim}{\tau}$$

T10 T11

I II

where σ_s is the static stability.

$$\sigma_s \equiv - \frac{RT}{p\theta} \frac{\partial\theta}{\partial p} \qquad (2.23a)$$

Beneath each term is a Roman numeral indicating the term's relative importance on the mesoscale. Eq. (2.23) with appropriate boundary conditions will be used in Chapter 5 to diagnose omega fields from real data.

It is interesting to note the differences between the synoptic and mesoscales. The beta or Coriolis term is a first-order term on the synoptic scale but is negligible on the mesoscale. That is, as we go to smaller scales, the Coriolis force is less important and the wind is less geostrophic. The other significant difference between the scales is that although the diabatic term is important on the synoptic scale, it is relatively more important on the mesoscale. While the diabatic term should be included on the synoptic scale, it is even more important to include it on the mesoscale. In other words, local forcing by latent heating is more important on smaller scales. We expect that the vertical velocities to be diagnosed on the mesoscale in Chapter 5 will reflect the diabatic effect to a larger degree than the other forcing functions.

For divergent initialization to succeed, the initial divergence must be remembered by the model. That is, it must be supported by the model. Otherwise, the initial divergence will be dissipated by internal gravity waves. The initial divergence must be balanced by latent heating, especially on the mesoscale. If the divergence is not maintained by latent heating, it will not be remembered. Latent heating should occur immediately (in the first time steps of the forecast) in areas of upward motion. Therefore, those areas should

initially be saturated for stable layers and the convective parameterization scheme should produce convective heating in unstable moist layers.

As stated in Chapter 1, divergent initialization on the synoptic scale has had little effect. There was little effect on the dynamic variables and a slight if any effect on the initial precipitation rates. Where the omega equation was used in the determination of the divergent component, the omega equation did not contain a diabatic term. Although the initial moisture fields were not given, we speculate they were not initially saturated in areas of upward motion. Hence the initial divergence would not be sustained by the release of latent heat. Also, some of the terms in the vertical velocity equation that are most important on the synoptic scale such as vorticity advection are more susceptible to initialization-related noise. It is therefore possible that the initial divergence was dissipated before it could effect the initial precipitation rate. We will later show that on the mesoscale, the initial divergence is retained by the forecast model. It is possible that the divergent initialization procedure presented here could produce better results than those previously obtained if applied on the synoptic scale.

2.1.5 The geostrophic vorticity assumption

In the derivation of the vertical velocity equation in Section 2.1.2, we assumed that the local temporal rates of change of the actual vorticity and the geostrophic vorticity were equal. Without

this assumption, the vertical velocity equation would be predictive rather than diagnostic.

It is well known that the geostrophic vorticity assumption is a good approximation on the synoptic scale where quasi-geostrophic theory applies. In fact, this assumption has often been used to obtain the vorticity field from the observed height field rather than from wind observations. Scale analysis was applied to terms T16 and T17 of (2.19) as shown in Table 2. We see immediately that the terms are almost equal in magnitude and opposite in sign. It first appears that the geostrophic assumption will be valid at all scales. We know, however, that where the effects of curvature become important or where the divergent component is large such as in gravity waves, the geostrophic vorticity assumption is not at all accurate. For gravity waves, the scale analysis breaks down because the advective time scale is no longer appropriate for terms T16 and T17 of (2.19). Therefore, if this divergent initialization scheme were applied in the future to smaller scales, terms T16 and T17 may have to be included in the vertical velocity equation used.

Finally, on length scales where the geostrophic vorticity assumption breaks down, the terms labeled with a III in (2.19) may not be negligible in comparison with the I and II terms. In other words, the specific vertical velocity equation used for the divergent initialization of the PSU model depends on the smallest length-scale feature that will be permitted. The smallest permissible length scale depends on the grid increment, the data availability, the method of analysis, and the degree of smoothing.

2.2 Scale analysis of the divergence equation

This scale analysis will be conducted analogously to the one in Section 2.1. The same scaling relationships will be used.

2.2.1 Derivation of the divergence equation

Recall that (2.12) is the equation of motion in Z coordinates. We obtain the divergence equation by operating on (2.12) with $\nabla\cdot$ to obtain

$$\nabla\cdot\frac{\partial \underset{\sim}{V}}{\partial t} + \nabla\cdot[(\underset{\sim}{V}\cdot\nabla)\underset{\sim}{V}] + \nabla\cdot(\dot{Z}\,\frac{\partial \underset{\sim}{V}}{\partial Z}) + \nabla^2\phi' + \nabla\cdot(f\hat{k}\times\underset{\sim}{V}) - \nabla\cdot\underset{\sim}{F_r} = 0 \quad . \tag{2.24}$$

Using (2.3), (2.24) becomes

$$\begin{array}{ccccc} \dfrac{\partial D}{\partial t} + \nabla\cdot[\underset{\sim}{V}_\psi\cdot\nabla\underset{\sim}{V}_\psi & + & \underset{\sim}{V}_\chi\cdot\nabla\underset{\sim}{V}_\psi & & \\ \text{T1} & & \text{T2a} & & \text{T2b} \\ & & \text{I} & & \text{II} \end{array}$$

$$\begin{array}{ccccc} + \underset{\sim}{V}_\psi\cdot\nabla\underset{\sim}{V}_\chi & + & \underset{\sim}{V}_\chi\cdot\nabla\underset{\sim}{V}_\chi] & + & \nabla\cdot\dot{Z}\,\dfrac{\partial \underset{\sim}{V}_\psi}{\partial Z} \\ \text{T2c} & & \text{T2d} & & \text{T3a} \\ \text{II} & & \text{III} & & \text{II} \end{array} \tag{2.25}$$

$$+ \nabla\cdot\dot{Z}\frac{\partial \underset{\sim}{V}_\chi}{\partial Z} + \nabla^2\phi' - f\zeta - \hat{k} \times \nabla f\cdot\underset{\sim}{V}_\psi$$

T3b T4 T5a T5b

III I I II

(2.25) (cont.)

$$- \hat{k} \times \nabla f\cdot\underset{\sim}{V}_\chi - \nabla\cdot\underset{\sim}{Fr} = 0$$

T5c T6

III III

which is the complete divergence equation in Z coordinates.

As is customarily done, we will neglect the time-dependent term T1. This leaves a diagnostic relationship which can be termed the complete balance equation. In Section 2.2.4, we will analyze the effect of neglecting this term.

2.2.2 Scale analysis of the balance equation

We will examine (2.25), term by term (see Table 3). For the synoptic scale, where L $\sim$ 1000 km and Ro $\sim$ 0.1, terms T2a, T4, T5a, and T5b are at least an order of magnitude larger than the other terms. These terms are the advection of momentum, the Laplacian of geopotential, the Coriolis parameter times the relative vorticity, and the beta term, respectively. The equation containing only these terms is commonly referred to as the nonlinear balance equation. A form of that equation has been used in the nondivergent initialization of the PSU model (WAM; Keyser, 1978; Anthes, 1978). It has been previously

Table 3. Scale analysis of the divergence equation.

Term designator	Scale factor
T1	$T1 \sim \frac{V}{L} R_1 \frac{V}{L} \sim R_1 \frac{V^2}{L^2}$
T2a	$T2a \sim \frac{1}{L} V \frac{1}{L} V \sim \frac{V^2}{L^2}$
T2b	$T2b \sim R_1 \; T2a \sim R_1 \frac{V^2}{L^2}$
T2c	$T2c \sim R_1 \; T2a \sim R_1 \frac{V^2}{L^2}$
T2d	$T2d \sim R_1 \; T2b \sim R_1^2 \frac{V^2}{L^2}$
T3a	$T3a \sim \frac{1}{L} R_1 \frac{V}{L} V \sim R_1 \frac{V^2}{L^2}$
T3b	$T3b \sim R_1 \; T3a \sim R_1^2 \frac{V^2}{L^2}$
T4	$T4 \sim \frac{1}{L^2} fVL \sim \frac{1}{Ro} \frac{V^2}{L^2}$
T5a	$T5a \sim \frac{1}{Ro} \frac{V}{L} \frac{V}{L} \sim \frac{1}{Ro} \frac{V^2}{L^2}$
T5b	$T5b \sim \beta V \sim \frac{f}{a} V \sim \frac{1}{Ro} \frac{V}{L} \frac{1}{a} V \sim \frac{1}{Ro} \frac{L}{a} \frac{V^2}{L^2}$
T5c	$T5c \sim R_1 \; T5b \sim \frac{R_1}{Ro} \frac{L}{a} \frac{V^2}{L^2}$
T6	$T6 \sim \frac{[T10 \text{ of } (2.19)]}{f} \sim Ro \frac{L}{V} \frac{1}{Ro} \frac{C_D}{H} \frac{V^3}{L^2} \sim \frac{C_D}{H} \frac{V^2}{L}$

substantiated that the above terms dominate on the large scale (see, e.g., Haltiner, 1971).

2.2.3 Determination of the mesoscale balance equation

As in Section 2.1.4, we use for mid-latitudes and the mesoscale, $L \sim 100$ km, $Ro \sim 1$, $L/a \sim 0.01$, $H \sim 10$ km, and $C_D \sim 0.001$. With these values, the relative order of magnitude of the terms in (2.25) is indicated in Roman numerals underneath each term. As with (2.19), the difference between I and II is an order of magnitude. Because we are interested in a divergent initialization, we include the terms containing the divergent component and, because we are interested in accuracy to second order, we neglect terms labeled III (T2d, T3b, T5c, and T6). Therefore, the final mesoscale balance equation is composed of terms T2a, T2b, T2c, T3a, T4, T5a, and T5b, and will be referred to as (2.26). The difference between the synoptic and mesoscale balance equations is the relative importance of the Coriolis force on these scales. On the synoptic scale, the beta term is a first-order term. On the mesoscale, the beta term becomes two orders of magnitude smaller than the first-order terms.

In order to achieve maximum consistency with the forecast model, which should help the model "remember" the divergent component, the balance equation will be applied on sigma surfaces. Sigma is defined by

$$\sigma \equiv \frac{p - p_t}{p_s - p_t} \equiv \frac{p - p_t}{p_*} \tag{2.27}$$

where p is the pressure of the sigma level, p_t is the pressure at the model top, p_s is the surface pressure, and $p_* = p_s - p_t$. Now, for $p_t = 0$, we can show

$$\dot{\sigma} \frac{\partial}{\partial \sigma} = \dot{Z} \frac{\partial}{\partial Z} \quad . \tag{2.28}$$

With (2.28), term T3a of (2.26) becomes

$$\nabla \cdot \dot{\sigma} \frac{\partial \underset{\sim}{V}_\psi}{\partial \sigma} \tag{2.29}$$

and T4 becomes

$$\nabla \cdot \left[\nabla \phi + \frac{RT}{p_*} \nabla p\right] \quad . \tag{2.30}$$

Therefore, the mesoscale balance equation in sigma coordinates is

$$\begin{aligned} &\nabla \cdot [\underset{\sim}{V}_\psi \cdot \nabla \underset{\sim}{V}_\psi + \underset{\sim}{V}_\psi \cdot \nabla \underset{\sim}{V}_\chi + \underset{\sim}{V}_\chi \cdot \nabla \underset{\sim}{V}_\psi] \\ &\qquad + \nabla \cdot \dot{\sigma} \frac{\partial \underset{\sim}{V}_\psi}{\partial \sigma} + \nabla \cdot \left[\nabla \phi + \frac{RT}{p_*} \nabla p\right] \\ &\qquad - f\zeta - \hat{k} \times \nabla f \cdot \underset{\sim}{V}_\psi = 0 \end{aligned} \tag{2.31}$$

where V_ψ and V_χ are defined on pressure surfaces. That is, if $\nabla_p \cdot \underset{\sim}{V}_\psi = 0$, then $\nabla_\sigma \cdot \underset{\sim}{V}_\psi$ is not necessarily zero because of the slope of the sigma surface. In this thesis, the terms nondivergent and divergent will always apply to pressure and not sigma surfaces.

2.2.4 Effect of neglecting the local rate of change of divergence

The local rate of change of divergence was neglected in the determination of the balance equation in Section 2.2.1. This assumption is often made on the synoptic scale. The scale analysis in Table 3 shows that Tl of (2.25) is an order of magnitude smaller than the largest terms. We will show that this assumption is reasonable on the upper meso-β scale.

We can examine the effect of the local rate of change of divergence term in the diagnosis of geopotential. Let the entire divergence equation be

$$\nabla^2\phi = -\frac{\partial D}{\partial t} \quad . \tag{2.32}$$

A one-dimensional analysis is sufficient and hence we can write (2.32) as

$$\frac{\partial^2\phi}{\partial x^2} = -\frac{\partial D}{\partial t} \quad . \tag{2.33}$$

Let $\frac{\partial D}{\partial t}$ be expressed with a spectral representation as

$$\frac{\partial D}{\partial t} = \hat{D}\, e^{i\kappa x} \tag{2.34}$$

where $\hat{D}$ has dimensions of s^{-2} and $\kappa = 2\pi/L$ is the wavenumber. Therefore, we can write (2.30) as

$$\frac{\partial^2 \phi}{\partial x^2} = - \hat{D} e^{i\kappa x} \quad . \tag{2.35}$$

Integration of (2.35) twice with respect to x yields

$$\phi = \frac{\hat{D}}{\kappa^2} e^{i\kappa x} + c_1 x + c_2 \tag{2.36}$$

where c_1 and c_2 are arbitrary constants. Therefore, the error in geopotential associated with the neglect of this term is on the order of

$$\phi_{error} \sim \frac{\hat{D}}{\kappa^2} \quad . \tag{2.37}$$

Choose a typical mesoscale divergence of 10^{-5} s^{-1}. The mesoscale length scale $L \sim 10^5$ m and the velocity scale $V \sim 10$ m s^{-1} imply a time scale of 10^4 s. Therefore,

$$\hat{D} \sim 10^{-9} \ s^{-2} \quad . \tag{2.38}$$

Now (2.37) becomes

$$\phi_{error} \sim \frac{L^2 \hat{D}}{4\pi^2} \quad . \tag{2.39}$$

With (2.38) and $L \sim 10^5$ m, (2.39) gives

$$\phi_{error} \sim 0.25 \ m^2 \ s^{-2} \quad . \tag{2.40}$$

Hence for the local rate of change of divergence term to be important on the upper meso-β scale, large values of divergence are required.

Fankhauser (1974) reported that $\frac{\partial D}{\partial t}$ was large in the vicinity of a squall line but was small away from the active convection. With this result and (2.40), we conclude that neglecting the $\frac{\partial D}{\partial t}$ term on the mesoscale is an acceptable approximation. The term might become important on smaller scales and may have to be included there.

2.3 Boundary conditions required by limited domains

The diagnostic equations for the mesoscale, derived in this chapter, are second-order elliptic PDEs. For purposes of this discussion of boundary conditions, they can be represented as Poisson equations. For global or hemispheric models, boundary conditions have not been a major problem. However, the attainable resolution has been coarse at best. Limited-area models have been developed primarily to obtain increased horizontal as well as vertical resolution. But, because the limited-area domains have boundaries, boundary conditions must be specified on the dependent variables or else the problem of solving the equation is not mathematically well posed (Ames, 1977). The specification of boundary conditions for limited-area NWP models and their initialization schemes has indeed been a problem. In this section we will examine the boundary conditions required by the divergent initialization scheme for the following variables: stream function, geopotential, omega, and velocity potential.

2.3.1 Boundary conditions on the stream function

Several of the terms in the omega and divergence equations require knowledge of the nondivergent wind. The nondivergent wind is related to the stream function by (2.3a) and the stream function is related to the vorticity field by

$$\nabla^2\psi = \zeta \quad . \tag{2.41}$$

Vorticity is calculated at the interior grid points and ψ can be calculated on the interior if we know ψ_B. There are numerous methods presented in the literature for the determination of ψ_B (see, e.g., Phillips, 1958; Anthes, 1976; Brown and Neilon, 1961; Bedient and Vederman, 1964; Hawkins and Rosenthal, 1965; Sangster, 1960; Shukla and Saha, 1974; Schaeffer and Doswell, 1979; Stephens and Johnson, 1978; Endlich, 1967). We will present an appropriate method after demonstrating what property the chosen method must possess. Before presenting that method, however, we will look at another means of avoiding boundary effects.

A method which may improve upon the results obtained by the aforementioned authors has been used by Anthes (1976), Anthes (1978), Keyser (1978), and Elsberry and Ley (1976), among others. The idea is to initialize on a domain larger than that over which the model will produce the forecast, thus minimizing boundary effects by moving them away from the forecast domain. However, we choose not to use this approach in this thesis for the following reasons:

(1) It is not always possible to enlarge the domain. For example, in certain situations, auxiliary rawinsonde measurements are taken over limited areas (Hill and Turner, 1977). Hence, there are no data on which the enlarged initialization domain could depend. Also, it is not always desirable to enlarge the initialization domain. Enlarging the domain could mean incorporating ocean or other data-sparse regions where the boundary values of the meteorological variables contain more uncertainty than in data-dense regions. Thus expanding the initialization domain could result in an inferior initialization on the forecast domain.

(2) It is computationally inconvenient to enlarge the domain.

(3) We will show that, by taking a few reasonable precautions, the boundary values of ψ (and χ) can be determined to sufficient accuracy for purposes of this thesis without expanding the initialization domain.

Keyser (1978) analyzed the effect of boundary conditions on the solution of a Poisson equation such as

$$\nabla^2\phi(x,y) = F(x,y) \tag{2.42}$$

where the rectangular domain is defined in x and y by $0 < x < L_1$ and $0 < y < D_1$. Following Morse and Feshbach (1953), that portion of the solution due to ϕ_B for the right boundary (ϕ_{RB}) can be written as

$$\phi_{RB}(x,y) = \frac{2}{D_1} \sum_{n=1}^{\infty} \frac{\sinh \frac{n\pi}{D_1} x}{\sinh \frac{n\pi}{D_1} L_1} \sin \frac{n\pi}{D_1} y \int_o^{D_1} \phi(L_1,y) \sin \frac{n\pi}{D_1} y \, dy \quad . \tag{2.43}$$

There are four other terms in the total solution, one for each of the other three boundaries and one for the forcing function. For this discussion, we need to consider only one boundary. Since (2.42) is linear, we may interpret (2.43) for a single harmonic without loss of generality. Define μ as

$$\mu = \frac{\sinh \frac{n\pi}{D_1} \frac{L_1}{L_1} \frac{x}{L_1}}{\sinh \frac{n\pi}{D_1} L_1} \quad . \tag{2.44}$$

For a given distance from the boundary, for increasing wavenumber, the value of μ decreases. Therefore, μ is called a damping factor. Keyser plotted

$$\mu = f\left(\frac{n\pi}{D_1} \frac{L_1}{L_1} \;,\; \frac{x}{L_1}\right) \tag{2.45}$$

and this is reproduced as Fig. 1. From this argument emerged two very important conclusions (Keyser, 1978):

(1) The influence of boundary conditions on the solution decreases exponentially with distance from the boundaries.

(2) It is most important to accurately specify the large-scale (low-wavenumber) variation of the boundary

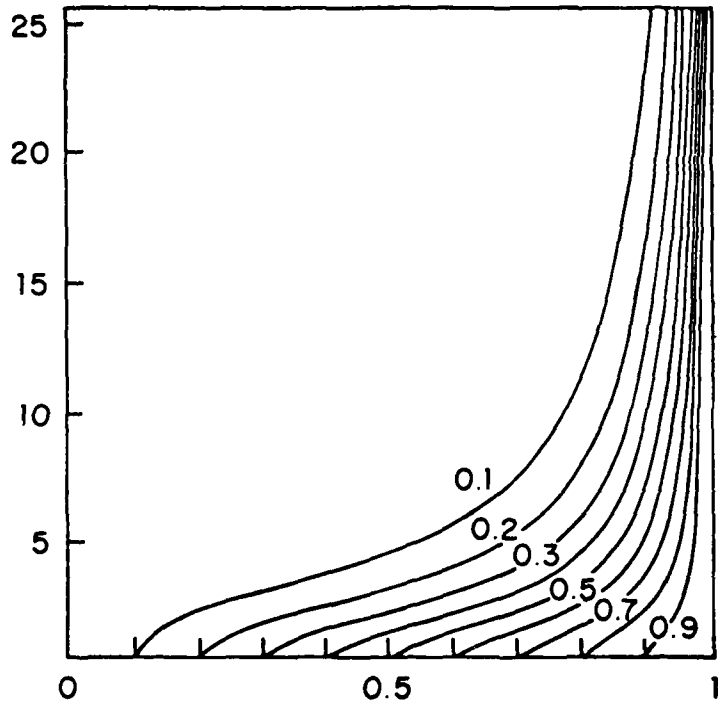

Fig. 1. Plot of contours of μ representing the fractional damping of the boundary condition at x/L = 1 as a function of distance normal to the boundary and wavenumber (Keyser, 1978).

conditions since amplitude errors for low-wavenumber components of the boundary conditions damp less rapidly with distance away from the boundary.

Keyser extended the analysis to a discrete domain but the conclusion regarding correct specification of the large-scale variation of the boundary conditions was unaltered.

Therefore, in examining the adequacy of the methods for determining ψ_B, we need only concern ourselves with choosing a method capable of correctly specifying the low-wavenumber variation of ψ_B. WAM, Anthes (1976), and Keyser (1978) report that when Anthes (1976) method was used to evaluate ψ_B, the required correction to $v_{n_{obs}}$ (observed boundary normal wind component) was on the order of a few tenths of a meter per second. Since the magnitude of v_n itself was about two orders of magnitude larger than the correction applied, then the large-scale features are retained in the corrected v_n. In other words, since the observed wind was predominantly nondivergent, $v_{n_{obs}}$ was almost v_{n_ψ}. We conclude that Anthes (1976) method may be used to solve (2.41) in the determination of the nondivergent wind for the scales studied here.

Anthes (1976) method is based on:

$$\frac{\partial \psi}{\partial s} = - (v_{n_{obs}} + c_B) \tag{2.46}$$

where

$$c_B = -\frac{1}{L_p} \oint v_{n_{obs}} \, ds \quad , \tag{2.47}$$

and where L_p is the length of the domain perimeter. First, c_B is computed from (2.47). Then, after one ψ_B value is specified, (2.46) is integrated around the boundary to obtain a complete set of ψ_B values. That is, the mean divergence over the domain is removed from $v_{n_{obs}}$ by applying an equal correction to each boundary observed normal wind component.

2.3.2 Boundary conditions on geopotential for the balance equation

We know from the discussion of the previous section that the large-scale variation in geopotential must be accurately specified. The usual method of calculating ϕ_B has been to assume that the boundary winds are geostrophic and integrate

$$\frac{\partial \phi}{\partial s} = \overline{f} \frac{\partial \psi}{\partial s} \tag{2.48}$$

around the boundary. WAM reported that this approach was unsatisfactory because wind analysis errors accumulated around the boundary. Therefore, WAM used the observed heights on the boundary. This did indeed preserve the large-scale geopotential variation.

Keyser (1978) and Anthes (1978) used FNWC (Fleet Numerical Weather Central, Monterey, California) analyses for numerous initializations and subsequent forecasts. They claimed that the large-scale geopotential boundary variation was preserved and hence

$\phi_B = \phi_{B_{obs}}$ was an adequate boundary condition. That is, it did not introduce any significant error in geopotential on the domain interior. Therefore, we adopt the use of observed boundary heights as the boundary condition for the balance equation in this thesis.

2.3.3 Boundary conditions on omega for the omega equation

The omega equation will be solved by three-dimensional relaxation and therefore boundary values of omega for the top, sides, and bottom of the domain volume are required.

For the top of the domain (250 mb), we set omega equal to zero. If the 250-mb level is the top of the features and circulations being modeled, then this choice makes meteorological sense. Since the 200-mb level is the top data level used, then there is really no other reasonable alternative. Also, the model itself requires zero omega at the top pressure level.

Omega is also set to zero on the side faces of the domain volume. This is mathematically expedient but probably somewhat unrealistic. The meteorologically interesting feature is normally placed near the center of the domain. Hence there are usually no large divergence values near the boundaries. With this precaution, omega values of zero at the side boundaries approximately represent the correct large-scale boundary variation of omega. We will adopt this precaution here.

The PSU model uses terrain heights as the lower boundary condition on geopotential. The terrain in turn induces an omega at the surface. The terrain-induced omega, ω_t, can be written

$$\omega_t = - \frac{gp}{RT} \underset{\sim}{V}_\psi \cdot \nabla h \tag{2.49}$$

where h is the terrain height. We use scale analysis to estimate the importance of this effect. From (2.11), we can write

$$\dot{Z}_t = - \frac{\omega_t}{p_s} \quad . \tag{2.50}$$

Therefore, (2.49) becomes

$$\dot{Z}_t = \frac{g}{RT} \underset{\sim}{V}_\psi \cdot \nabla h \sim \frac{1}{H} \frac{Vh}{L} = \frac{Vh}{HL} \quad . \tag{2.51}$$

Using the scales H $\sim$ 10 km, L $\sim$ 100 km, V $\sim$ 10 m s^{-1}, and a terrain gradient of 0.001 (*a 100 m rise in 100 km is not uncommon*), we get $\dot{Z}_t \sim 10^{-6}$ s^{-1}. Note that in mountainous terrain, a slope of 0.01 would be more appropriate and $\dot{Z}_t$ would be an order of magnitude larger.

These terrain-induced vertical velocities are indeed significant. In more familiar coordinates, we get

$$\begin{aligned} \omega_t &= - p_s \dot{Z}_t \sim 10^2 \text{ cb } 10^{-6} \text{ s}^{-1} \\ &= 10^{-4} \text{ cb s}^{-1} \sim 10 \text{ cb d}^{-1} \quad . \end{aligned} \tag{2.52}$$

Vertical velocities in the mid-troposphere normally don't exceed 10 cb d^{-1} except in sharp troughs and precipitation areas. We conclude that the terrain effect omega values should be used as the lower boundary condition for the omega equation relaxation.

2.3.4 Determination of appropriate boundary conditions on velocity potential

Velocity potentials are required so that the divergent wind component can be supplied to the omega and balance equations. Using (2.3b) and (2.13), we obtain

$$\nabla^2\chi = D \tag{2.53}$$

or

$$\nabla^2\chi = -\frac{\partial\omega}{\partial p} \quad . \tag{2.54}$$

We can solve (2.53) given values of omega and χ_B.

Several methods for the determination of χ_B have been used previously (see, e.g., Brown and Neilon, 1961; Bedient and Vederman, 1964; Shukla and Saha, 1974; Endlich, 1967; Schaeffer and Doswell, 1979; Stephens and Johnson, 1978). Most of the above methods involve at least one assumption. Two of the methods (Schaeffer and Doswell, 1979; Stephens and Johnson, 1978) have accurately separated observed wind fields into nondivergent and divergent components. However, here we will diagnose vertical velocities and therefore divergence values. We want a divergent component corresponding to these divergence values and not necessarily related to the observed or nondivergent winds. We will develop a means of accurately specifying the large-scale boundary variation of velocity potential.

The divergence theorem may be written

$$\iint \nabla\cdot\underset{\sim}{G}\ dA = \oint \hat{n}\cdot\underset{\sim}{G}\ ds \tag{2.55}$$

where $\underset{\sim}{G}$ is an arbitrary horizontal vector, A is the domain area, and s is distance along the domain perimeter, the line integral being positive in the counterclockwise sense. Applied to the velocity vector, (2.55) becomes

$$\iint \nabla\cdot\underset{\sim}{V}\ dA = \iint D\ dA = \oint \hat{n}\cdot\underset{\sim}{V}\ ds \quad . \tag{2.56}$$

In words, (2.56) states that the integral of the divergence over the entire domain can be calculated by integrating the normal boundary component around the boundary. That is, if the normal velocity component integrates to zero, there is no net divergence over the domain.

In finite difference form, (2.56) becomes

$$\Delta x \sum_{i=2}^{M-1} \sum_{j=2}^{N-1} D_{i,j} = \sum_{k=1}^{NBP} v_{n_k} \tag{2.57}$$

where M is the number of grid points in the y direction, N is the number of points in the x direction, and NBP is the total number of boundary points. Now, from the omega equation, we can calculate the left hand side of (2.57). Therefore, we know the mean value of the normal velocity component. Since $\overline{\frac{\partial X}{\partial s}} = 0$, it follows that

$$\overline{v}_n = \hat{n}\cdot\overline{\underset{\sim}{V}\chi} = \hat{n}\cdot\overline{\nabla\chi} = \overline{\frac{\partial\chi}{\partial n}} \quad . \tag{2.58}$$

Now we know the mean boundary value of $\frac{\partial\chi}{\partial n}$ since

$$\overline{v}_n = \overline{\frac{\partial\chi}{\partial n}}\Big|_c \tag{2.59}$$

where the subscript c means the correct value.

The complete method for obtaining χ_B with correct low-wavenumber variation is as follows:

(1) Use (2.57) and (2.59) to compute the exact mean value of the normal derivative of velocity potential required to satisfy the known forcing function.

(2) Set χ over the domain and χ_B equal to zero.

(3) Begin to solve

$$\nabla^2\chi = D \tag{2.60}$$

by relaxation where

$$\nabla^2\chi \equiv \frac{\chi_{i,j+1} + \chi_{i,j-1} + \chi_{i+1,j} + \chi_{i-1,j} - 4\chi_{i,j}}{4(\Delta x)^2} \tag{2.61}$$

where Δx is the grid increment. Apply n iterations.

(4) With a one-sided difference, compute the mean boundary value of $\frac{\partial\chi}{\partial n}$ that currently exists on the domain after n iterations ($\overline{\frac{\partial\chi}{\partial n}}\Big|_a$, where the subscript a means the actual mean boundary value).

(5) Compute

$$\text{BADJ} = \bar{v}_n - \overline{\frac{\partial \chi}{\partial n}}\Big|_a \tag{2.62}$$

where the LHS of (2.62) is the mean correction that must be applied to the existing $\frac{\partial \chi}{\partial n}$ so that the known boundary value, $\bar{v}_n$, will be realized.

(6) Apply the mean normal derivative correction by extrapolating outward from the first interior grid point. That is, for each boundary point, compute

$$\chi_B = \chi_{B-1} + \Delta x \cdot \text{BADJ} \tag{2.63}$$

where χ_{B-1} is the value of χ at the first interior grid point.

(7) Return to step (3). Repeat this cycle m times.

(8) χ_B now has the correct large-scale boundary variation. Apply a direct solver (Rosmond and Faulkner, 1976; Swarztrauber and Sweet, 1975) to obtain χ over the entire domain for the given χ_B values and forcing function.

The advantages of this procedure are:

(1) It imposes no arbitrary boundary conditions.

(2) The method is physically realistic and mathematically sound. It is physically realistic because information

about the known forcing function is transmitted to χ_B through the relaxation procedure. It is well-founded mathematically because it forces the boundary value of $\overline{\frac{\partial \chi}{\partial n}}$ to approach the value it must have for the given forcing field. We are interested in the correct gradient of velocity potential and not χ itself since only the χ gradient has physical meaning. The boundary values of χ that result are those that would exist if the domain were infinite. The method is mathematically equivalent to using a Green's function solution of (2.53) (Hayek, personal communication; Morse and Feshbach, 1953). The applicable Green's function for Cartesian coordinates is

$$G(x,x_o,y,y_o) = \frac{1}{4\pi} \ln \left[(x-x_o)^2 + (y-y_o)^2\right] \tag{2.64}$$

The solution to (2.53) is therefore (Morse and Feshbach, 1953)

$$\chi(x,y) = \int\int D(x_o,y_o)\, G(x,x_o,y,y_o)\, dx_o\, dy_o \tag{2.65}$$

where (x,y) is a boundary point and (x_o,y_o) is any interior point where the divergence D is defined. For each boundary point, (2.65) must be applied for every interior point. Green's function solutions have the advantage that no boundary conditions on χ are required.

However, (2.64) becomes infinite as x approaches x_o and y approaches y_o. Therefore, (2.65) is computationally difficult to use in practice. Since we will now demonstrate that the method presented here is effective, we will use it in this thesis for the determination of χ_B.

To demonstrate the validity of the χ_B method, several numerical experiments were performed on a 15 by 15 grid with a grid increment of 100 km. The scenario was to generate an analytic χ field, compute the divergence (forcing function) at each grid point, and calculate $\bar{v}_n$. Then the χ values over the entire domain were zeroed and the method was applied. Table 4 contains a summary of the experiments. Figures, however, are included only for Experiments 2.2a through 2.2d since they are the most severe meteorological tests. For each experiment the value of n in step (3) was nine. That is, nine relaxation scans were made over the domain for each boundary normal component adjustment.

In Experiment 2.1, a circular initial velocity potential pattern was placed at the center of the domain. For Experiment 2.2, the center of the circular velocity potential pattern was shifted left to a position near the left boundary (Fig. 2). For Experiment 2.3, the initial χ field was given by

$$\chi = A \sin \frac{0.75\ \pi}{L_1} j\Delta x \qquad (2.66)$$

Table 4. Summary of experiments performed to demonstrate the validity of the new method for the determination of χ_B. MAXBDY is the number of iterations through which χ_B was corrected.

Experiment Number	Initial χ pattern	$\overline{v_n}$ ($m s^{-1}$)	MAXBDY	BADJ ($m s^{-1}$)	RMS error ($m s^{-1}$)			Percentage reduction in average RMS error (over first experiment in each set)
					u_χ	v_χ	$\overline{u_\chi + v_\chi}$	
2.1a	Circular; centered at grid center	-0.88	0	-0.427	0.15	0.15	0.15	--
2.1b	"	"	54	-0.141	0.021	0.021	0.021	84
2.1c	"	"	100	-0.137	0.03	0.03	0.03	80
2.2a	Circular; centered at i=8, j=4	"	0	-0.327	0.52	0.19	0.35	--
2.2b	"	"	54	-0.126	0.30	0.035	0.17	51
2.2c	"	"	100	-0.123	0.22	0.045	0.13	63
2.2d	"	"	300	-0.123	0.11	0.068	0.09	74
2.3a	Sine wave (2.66)	0.30	0	-0.400	1.07	0.59	0.83	--
2.3b	"	"	100	-0.167	0.81	0.58	0.69	17
2.3c	"	"	200	-0.160	0.76	0.58	0.67	19

AD-A105 501 AIR FORCE INST OF TECH WRIGHT-PATTERSON AFB OH F/G 7/2
THE INITIALIZATION OF THE DIVERGENT COMPONENT OF THE HORIZONTAL--ETC(U)
MAY 79 T C TARBELL
UNCLASSIFIED AFIT-CI-79-294D-S NL

2 OF 3
AD A105501

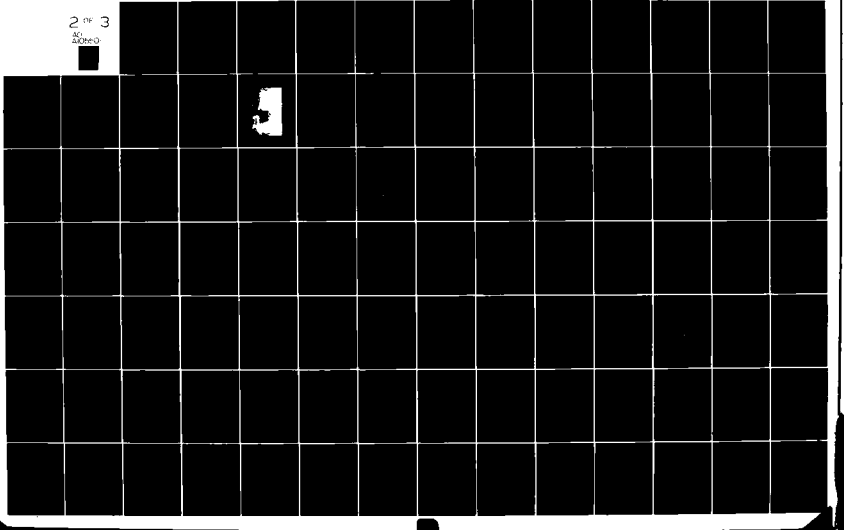

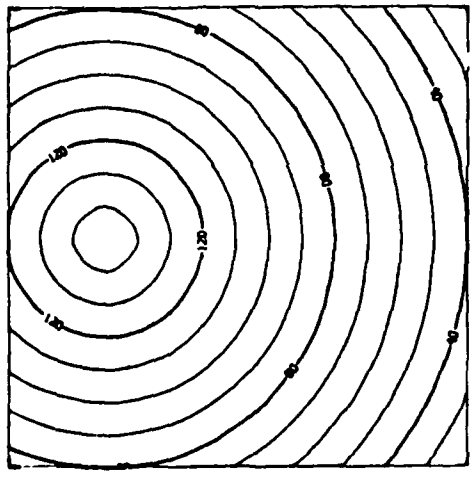

Fig. 2. Initial velocity potential field for Experiments 2.2a through 2.2d. The contour interval is 10^5 m^2 s^{-1} corresponding to a divergent wind speed of 1 m s^{-1}.

where A is the amplitude of the sine wave and here corresponds to a divergent wind speed of 5 m s^{-1}. Note there is no y variation of χ.

In Table 4, MAXBDY is the number of iterations for which χ_B was corrected. For each experiment, Table 4 gives the $\bar{v}_n$ adjustment applied (BADJ), the RMS (root-mean-square) error in u_x and v_x, the average RMS error, the percentage reduction in RMS error, and the number of iterations (MAXBDY) for each experiment in which the method was applied. The percentage reduction in RMS error is the percentage by which the RMS error of the χ gradient was reduced after Experiments 2.1a, 2.2a, and 2.3a.

In Experiment 2.2a, the final χ pattern (Fig. 3a) has little resemblance to the initial pattern (Fig. 2). The average gradient error corresponds to a velocity of 0.35 m s^{-1}. In Experiment 2.2b, with the method applied for 54 iterations, the final χ pattern (Fig. 3b) looks much closer to the initial pattern. Experiments 2.2c (Fig. 3c) and 2.2d (Fig. 3d) show additional improvement in the χ_B accuracy as well as the average RMS error.

When this method is used to compute χ_B and subsequently χ, the RMS error in the gradient of χ is not completely eliminated. Instead, the error decreases and then oscillates around some value as the value of the boundary correction (BADJ) levels off. For example, Experiment 2.1b actually has a slightly smaller RMS error than Experiment 2.1c. The maximum percentage RMS error reduction occurred at iteration 54 and oscillated between 79 percent and 84 percent for subsequent iterations through iteration 300. Therefore, it seems reasonable to establish a

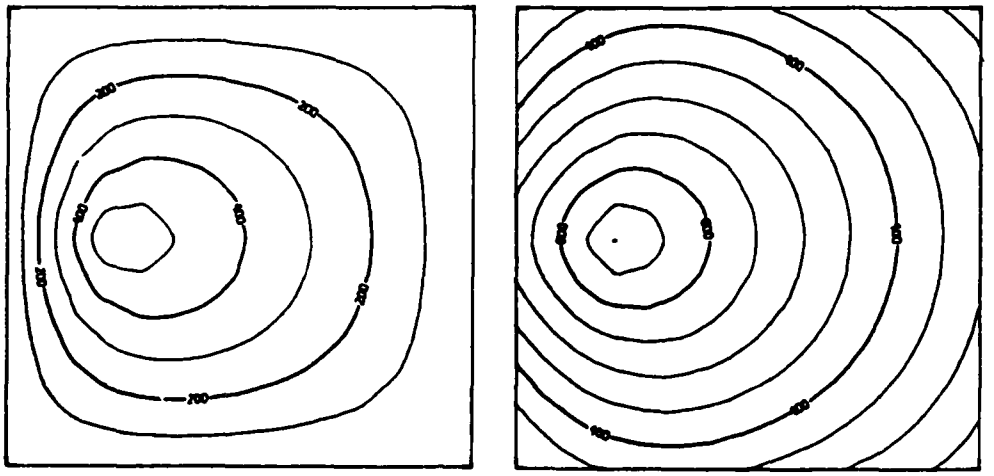

a. Experiment 2.2a.

b. Experiment 2.2b.

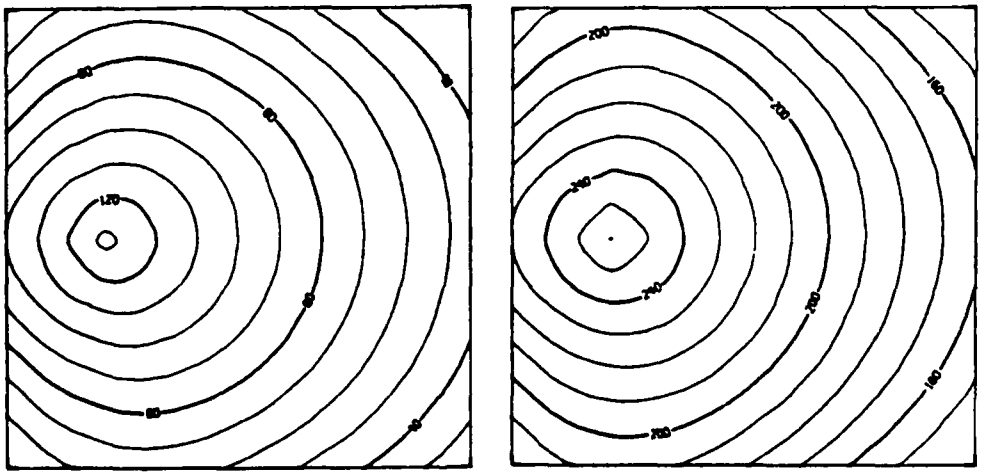

c. Experiment 2.2c.

d. Experiment 2.2d.

Fig. 3. Final velocity potential field for Experiments 2.2a through 2.2d. The contour interval is 10^5 m^2 s^{-1} corresponding to a divergent wind speed of 1 m s^{-1}.

criterion that is a compromise between increased accuracy and increased computational time. We observe that when BADJ changes by less than 10 percent over its previous value of nine iterations earlier, the majority of RMS error reduction has already occurred. BADJ changed by less than 10 percent at iteration number 45, 64, and 64 for Experiments 2.1b, 2.2c, and 2.3b, respectively. We conclude that, when the method is used in a subsequent chapter to determine χ_B, the criterion for when χ_B has been determined to sufficient accuracy is when BADJ changes by less than 10 percent. At that point, a direct solver will be applied to obtain the velocity potential on the domain interior.

We should also note that the initial χ patterns for Experiments 2.1 (a, b, and c) and 2.2 (a through d) are severe tests of the method. An average $v_{n_{obs}}$ of almost 1 m s^{-1} is larger than values normally encountered (WAM; Keyser, 1978).

This method for the determination of χ_B has several disadvantages:

(1) The method is an iterative technique and hence requires more computation time than most noniterative techniques. However, once the method determines a set of χ_B values with the correct low-wavenumber variation, iteration is no longer required and a direct solver is used to obtain velocity potential on the domain interior.

(2) Some forcing function fields require more normal derivative boundary corrections (MAXBDY) than others. This is especially true if small values of the forcing function occur near the boundary or if a large range of forcing

function values occur over the domain (both conditions true in Experiments 2.2a through 2.2d). We normally do not place a boundary in the vicinity of large values of the forcing function (the meteorologically interesting feature). That precaution will help minimize the effect of this disadvantage.

To summarize this section, we should first state that for purposes of divergent initialization, the methods which have been used previously may be unacceptable because they do not accurately specify the low-wavenumber variation in χ_B. We have developed a method to determine χ_B in such a way as to insure the correct large-scale χ_B variation. As previously stated, Keyser (1978) demonstrated that if the low-wavenumber χ_B variation was correct, then χ errors due to χ_B were insignificant in the domain interior. Therefore, this method for the determination of χ_B in conjunction with a direct solver can be used to obtain an accurate solution of the Poisson equation for velocity potential on a limited domain.

2.4 Chapter summary

The purpose of this chapter was to establish the divergent initialization procedure that will be used. Since we will initialize the PSU model, we stated which forces are considered in the model's equation of motion.

In the first section, we derived a complete generalized vertical velocity equation. Scale analysis was applied to demonstrate that the

quasi-geostrophic vertical velocity equation resulted for the synoptic scale. We then established the vertical velocity equation appropriate for the upper meso-β scale. The diabatic term was an important term in precipitation areas on the synoptic scale but it was even more important on the upper meso-β scale. In fact, on the upper meso-β scale, the diabatic term dominated the other forcing functions. Also, the Coriolis term was significantly less important than on the synoptic scale.

In the second section, we derived the complete generalized divergence equation. The nonlinear balance equation was shown by scale analysis to be valid on the large scale. The balance equation required for the upper meso-β scale was established and presented in sigma coordinates. On the upper meso-β scale, the Coriolis term was not as important as on the synoptic scale. We showed that the neglect of typical values of the local rate of change of divergence was an acceptable assumption on the upper meso-β and larger scales.

In the last section, using theoretical and mathematical tools, we established what boundary conditions should be used for stream function, geopotential, omega, and velocity potential. A new method for the correct low-wavenumber specification of χ_B was presented and its effectiveness was demonstrated for severe cases. A criterion for the termination of the method was determined experimentally. This new application was mathematically equivalent to a Green's function solution of the Poisson equation.

3.0 THE MESOSCALE MODEL

The PSU model is a general, predictive, hydrostatic, primitive equation, meteorological model formulated in sigma coordinates. For a complete description of the model, see AW and their references. The model has many options available such as variable terrain, a moisture cycle, and high- and low-resolution PBL physics. The model is suitable for forecasting flows with characteristic horizontal wavelengths of about 10-2500 km (meso-γ through macro-β scales) under a variety of meteorological conditions. It is indeed a versatile tool.

3.1 General description of the model

The model equations described in AW are in flux form, where the vertical coordinate σ is defined by (2.27). A Lambert conformal map projection will be used. There are equations for the u and v velocity components, a thermodynamic equation, and continuity equations for mass and water vapor.

For lateral boundary conditions during the model integration, a linear interpolation in time between the balanced conditions at the two nearest synoptic times is used. For example, for a 00 GMT (Greenwich Mean Time) to 06 GMT forecast, the model uses boundary values on u, v, T, ϕ, and q that are linearly interpolated in time between the boundary values at 00 GMT and 12 GMT. These "open"

boundaries allow features to enter the domain at the inflow boundaries and leave the domain at the outflow boundaries, without significant reflection of wave energy.

A staggered grid is employed with u and v defined at points ("dot points") midway between where the other variables are defined ("cross points"; reference Fig. 4). At the lowest sigma level ($\sigma = 1$), p_*, ϕ, and $\dot{\sigma}$ are defined while p and $\dot{\sigma}$ are specified at the top ($\sigma = 0$) sigma level. The dependent variables themselves (u, v, T, ω, ϕ, and q) are defined at the forecast levels whereas at the intermediate sigma levels, $\dot{\sigma}$ and the vertical fluxes of u, v, T, and q are defined (reference Fig. 5).

The time-differencing scheme used is the pressure-averaging technique of Brown and Campana (1978). This scheme permits a larger time step while meeting the linear stability (Courant-Friedrichs-Lewy or CFL) criterion for the advection term. However, in preliminary forecasts with the model, time splitting (the separation of the odd time-step solution from the even time-step solution) was a problem. As a result, Anthes (1978) and McNab (unpublished) incorporated a low-pass time smoother (Asselin, 1972; Robert, 1966) into the model. The subsequent model performance was improved. Unfortunately, because of numerical stability considerations, the time smoother requires a smaller time step.

The model employs both vertical and horizontal diffusion. In the low-resolution PBL version of the model used here, a simplified version of Deardorff's (1972) bulk PBL parameterization is used. No

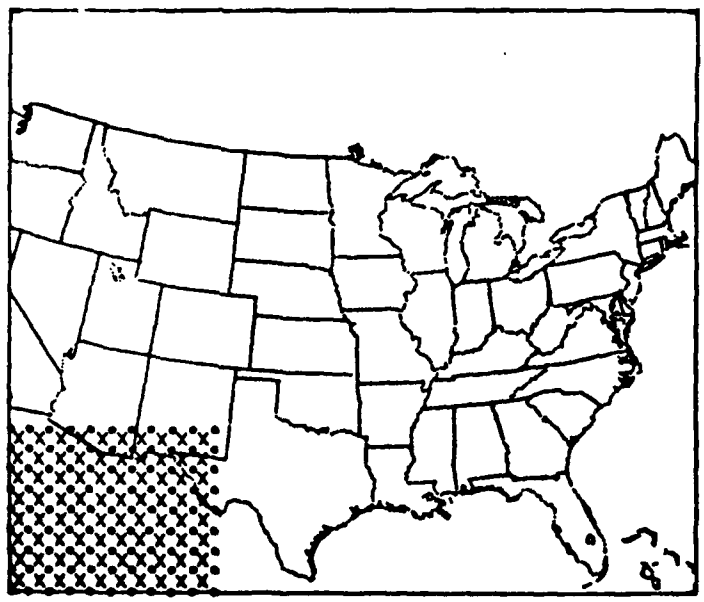

Fig. 4. A portion of the staggered horizontal grid. The horizontal velocity components are defined at the dot points. All other variables are defined at the cross points.

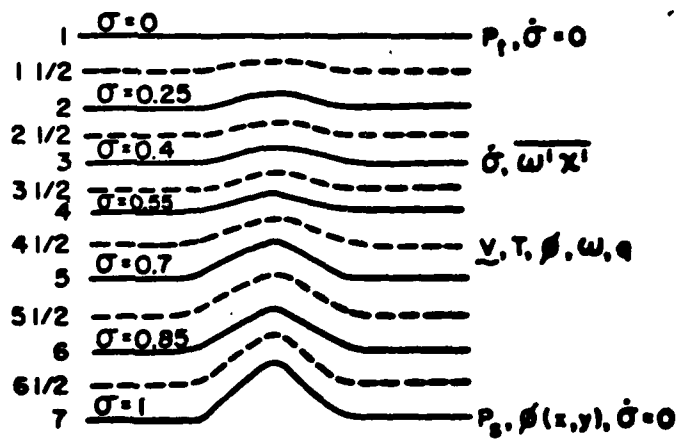

Fig. 5. Vertical grid structure of the mesoscale model showing vertical indexing and the levels at which the variables are defined.

other levels have vertical diffusion. The horizontal diffusion is applied to each variable and level and is required for numerical stability because the model permits nonlinear interactions. The horizontal diffusion scheme is that used by Smagorinsky et al. (1965) plus a constant background value for additional smoothing if desired. Additionally, Warner and McNab (unpublished) added the capability to enhance the horizontal diffusion near the boundaries. For a variable-size elliptical area defining the domain interior, the horizontal diffusion is not enhanced. Outside that area, the variable portion of the diffusion term is multiplied by a coefficient. The value of that coefficient is one at the edge of the ellipse. For every grid increment of distance away from the ellipse, the value is increased by a specified amount (variable name SPONGE). That is, the enhancement coefficient is equal to SPONGE times the distance in grid units that the grid point is outside the ellipse. Therefore, the horizontal diffusion increases as the boundary is approached. However, the total value of the horizontal diffusion coefficient is restricted to 40 percent of the maximum allowed by a linear stability analysis.

The model's moisture and cumulus cloud parameterizations are a simplified version of Anthes' (1977) scheme.

The PSU model has been tested and verified for a relatively large number of cases (WAM; Anthes, 1978; Shaginaw, 1979).

3.2 Specific model parameters used in this thesis

The domain chosen is a 30 by 35 grid with a grid increment (Δx) of 120 km. The domain is centered at 41N and 95W and therefore covers most of the contiguous 48 United States (US). The time step required for computational stability is 180 s.

The pressure at the top model sigma surface is fixed at 250 mb. There are six layers between the seven sigma levels of 0.0, 0.25, 0.4, 0.55, 0.7, 0.85, and 1.0.

The specific value of the surface drag coefficient, C_D, to be used was difficult to determine. Anthes (1978) reported that the value of C_D consistent with the bulk PBL parameterization should be between 0.001 and 0.003. Therefore, a value of 0.002 will be used here for C_D.

The variable enhanced horizontal diffusion scheme was tested for SPONGE values of 0.0, 1.0, 5.0, 12.5, and 25.0 for a 120-km Δx and the data set to be described in the next chapter. In the version used here, the size of the ellipse is such that the ellipse passes within $4\Delta x$ of the center of each boundary. The value of SPONGE chosen was 5.0. That is, midway between the corner points on any one side of the grid, the enhancement factor would be 20. The SPONGE value of 5.0 was chosen because it represents a compromise between smoothing the $2\Delta x$ noise that can penetrate the domain from the outflow boundary and not noticeably smoothing the large-scale features of interest.

3.3 Static initialization procedure

The initialization procedure utilized by WAM in previous forecasts will be briefly covered here. Winds were subjectively analyzed at the 850-, 700-, 500-, 400-, 300-, and 200-mb levels. Vorticity fields were obtained directly from these wind analyses using (3.1).

$$\zeta = \frac{\partial}{\partial x}\frac{v}{m} - \frac{\partial}{\partial y}\frac{u}{m} \tag{3.1}$$

In (3.1), x and y are the horizontal coordinates of the Lambert conformal map projection and m is the map factor. The stream function was then obtained using

$$\nabla^2\psi = \frac{\zeta}{m} \tag{3.2}$$

given ψ_B, the stream function on the lateral boundaries.

Geopotentials were calculated from the nonlinear balance equation

$$\nabla^2\phi = f\nabla^2\psi - 2m^2(\psi_{xy} - \psi_{xx}\psi_{yy}) + \beta_1\psi_y + \gamma_1\psi_x \tag{3.3}$$

where $\beta_1 = \frac{\partial f}{\partial y}$ and $\gamma_1 = \frac{\partial f}{\partial x}$. Of course to solve (3.3), ϕ_B is required. The observed boundary height values were used for ϕ_B in (3.3).

Finally, temperatures were calculated from the derived geopotentials through the hydrostatic equation. The nondivergent winds and balanced

temperatures were vertically interpolated from the levels at which they were calculated to the model sigma levels.

4.0 SYNOPTIC CASE CHOSEN FOR STUDY

We will use data for two synoptic times. For each time, the available data consist of vector winds on the synoptic rawinsonde network. Shaginaw (1979) subjectively analyzed the data for each of the six standard upper-level pressure surfaces and for sea level pressure. He then manually digitized the data for several hundred points at each level. The data were objectively analyzed with a Cressman (1959) scan. The data were digitized at enough points so that the Cressman scan reproduced well the sharp gradients and smaller features.

Shaginaw (1979) provided a comprehensive discussion of the synoptic situation for the period 17-21 November, 1975, and that discussion will not be repeated here. However, we will briefly summarize the meteorological conditions at the two synoptic times used here. Those times are 12191175 and 00201175, where the hhddmmyy format is broken down in hh = hour, dd = day, mm = month, and yy = year. For example, 12191175 represents 12 GMT, 19 November 1975.

A high pressure area (ridge) persisted over the southeastern US between the times 12191175 and 00201175. This ridge contributed to a severe pollution episode at Pittsburgh, PA. The ridge also provided a continuous supply of low-level moisture from the Gulf of Mexico to the Great Plains and adjacent states. This moisture supply was a key factor in the precipitation which occurred between 12191175 and 00201175. The moisture initialization used was provided by Wolcott (1979). He

developed a scheme incorporating satellite, surface, and rawinsonde data into the relative humidity analysis. The initial relative humidity fields for sigma levels 3½ and 5½ are given in Fig. 6. The satellite picture used for input into the moisture analysis is given in Fig. 7. It is important to note that the initial moisture field is saturated over a large portion of the central Plains states and the upper Midwest.

4.1 The synoptic situation at 12191175

The observed sea level pressure (SLP) is presented in Fig. 8a. A ridge dominates the eastern United States. A trough extends from a 1008-mb low near Big Bend through Minnesota.

The closed low at 500 mb (Fig. 8b) is centered at the "four corners" region. Although the ridge over the Southeast is weakening, the height gradient to the south and southeast of the closed low is increasing. Fig. 8c is the observed 500-mb wind velocity. There are relative minima associated with the closed low and the ridge over the Southeast. Of particular interest is the wind maximum entering the domain over the California-Mexico border. This wind maximum ("jet streak") will proceed to move around the south end of the trough and up the east side resulting in significant precipitation.

Fig. 8d is the observed 500-mb temperature field at 12191175. Note that the cold tongue extending southward from Montana reflects the trough position well.

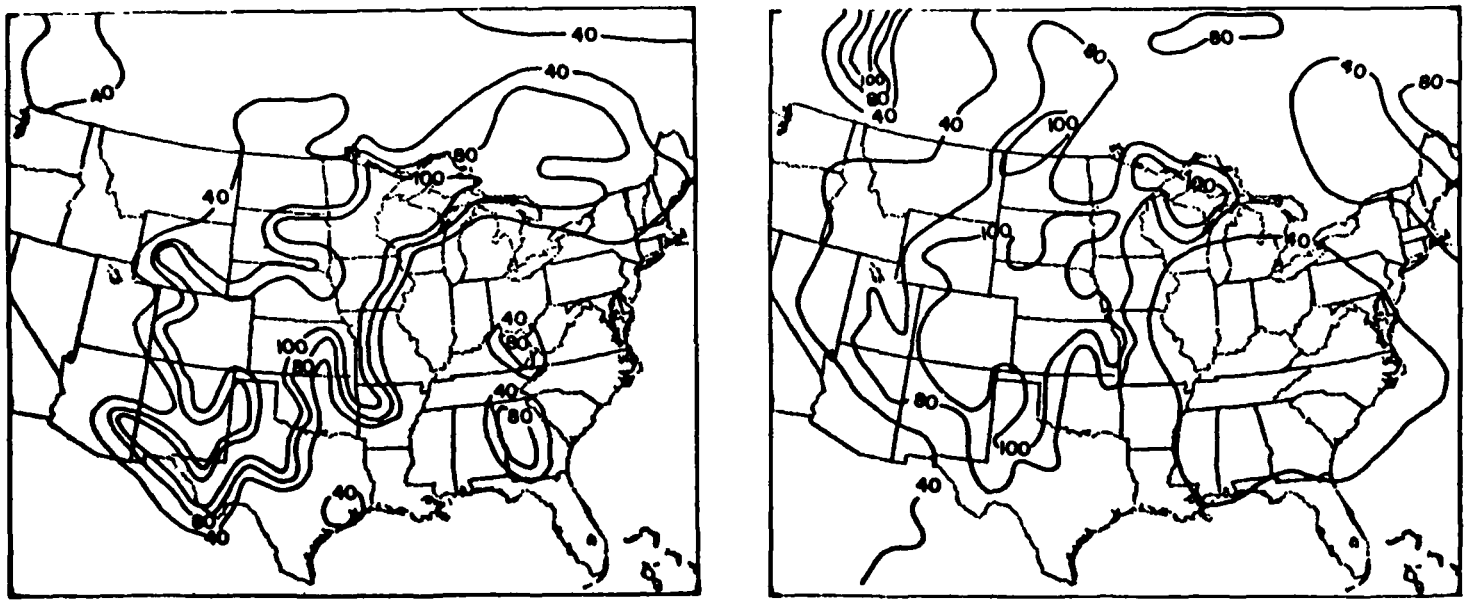

a. Sigma level 3½.

b. Sigma level 5½.

Fig. 6. Relative humidity analysis valid at 12191175 after Wolcott (1979). Areas of greater than or equal to 40, 80, and 100 percent relative humidity are shown.

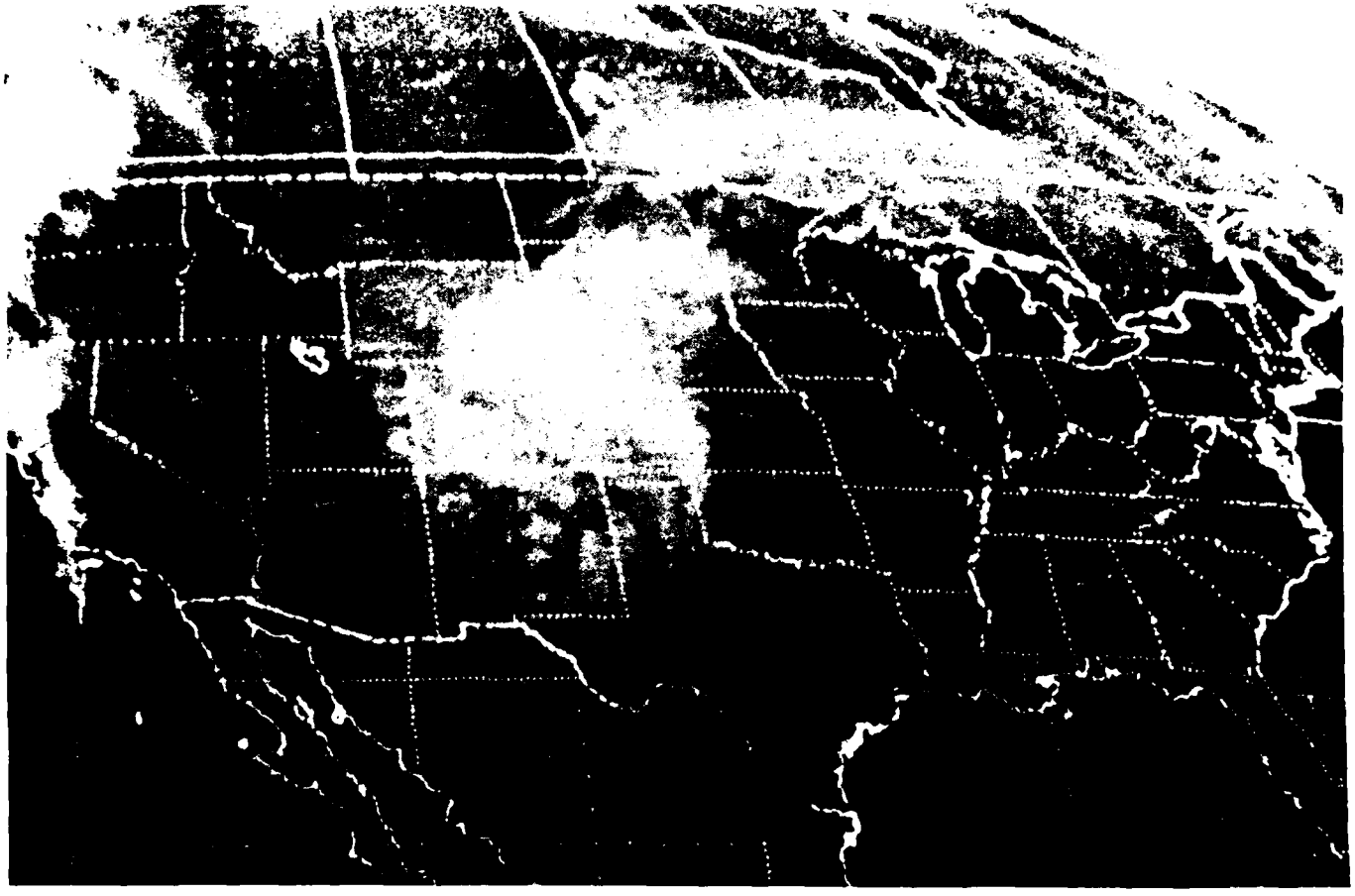

Fig. 7. Infrared-image satellite picture of the domain taken at 1145 GMT, 19 November 1975.

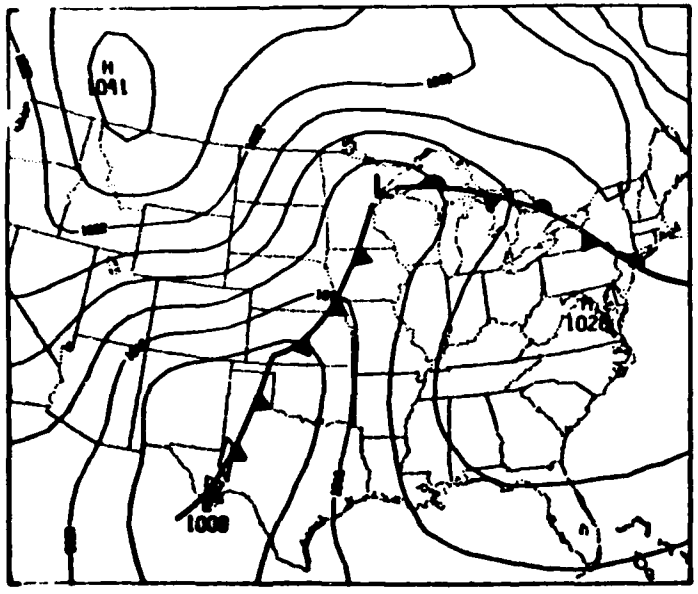

a. Sea level pressure. Surface fronts are indicated. The contour interval is 4 mb.

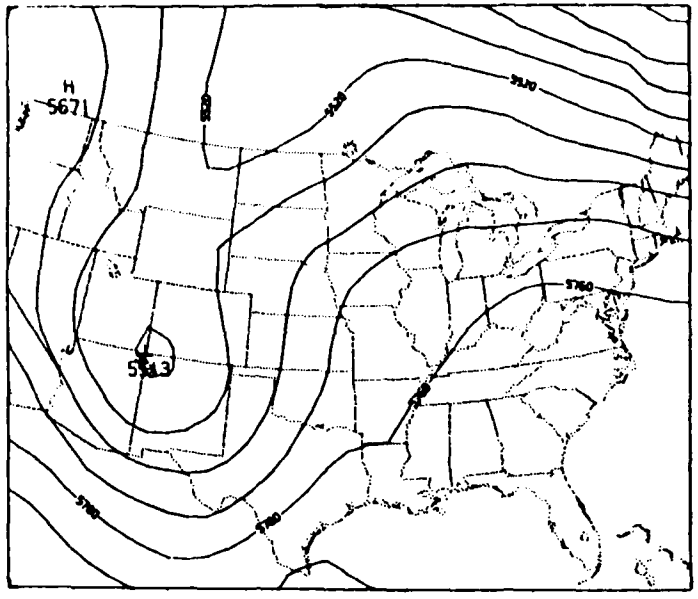

b. 500-mb heights. The contour interval is 60 m.

Fig. 8. Observed fields at 12191175.

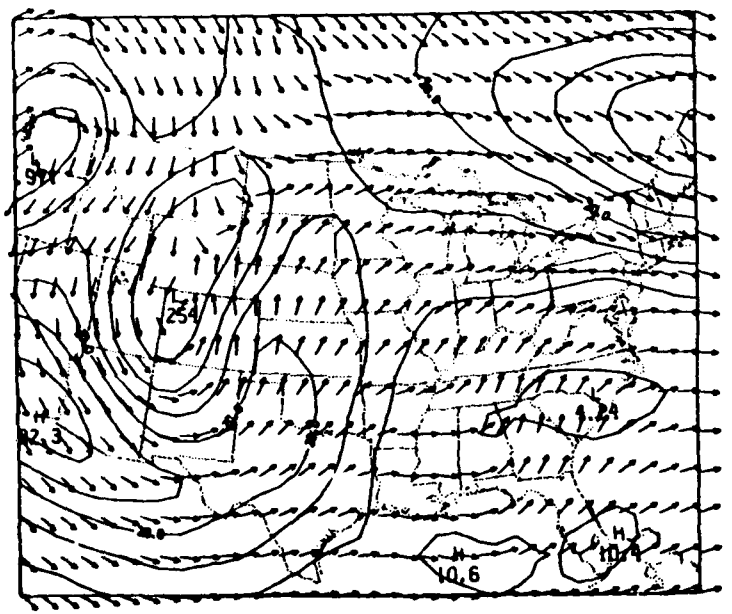

c. 500-mb winds. The contour interval is 5 m s^{-1}.

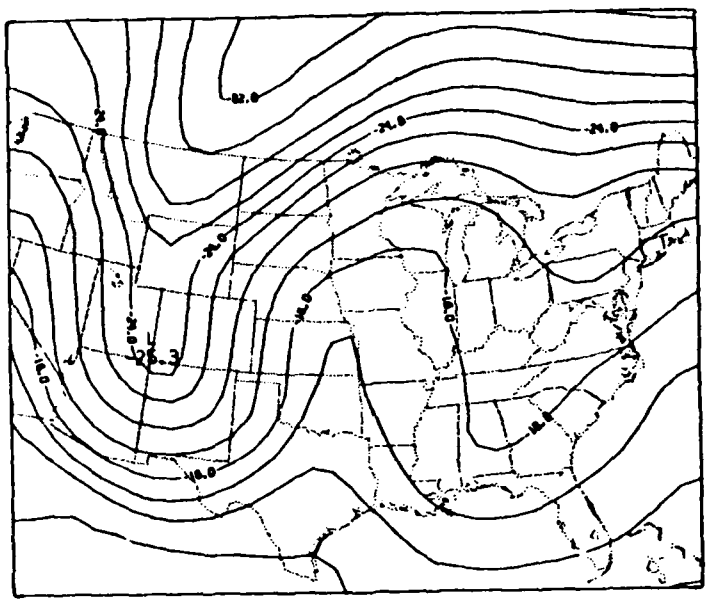

d. 500-mb temperatures. The contour interval is 2°C.

Fig. 8. (Continued).

Because we will attempt a divergent initialization at 12191175, we will now present for comparison, the results of the nondivergent initialization for 12191175 that was performed as outlined in Section 3.3. Fig. 9a is the nondivergent wind speed and direction. The differences between Figs. 9a and 8c in the vicinity of the trough are as expected. That is, the wind maximum from southern California through west Texas and up into the Plains states is not as strong in the nondivergent case. Also, the horizontal shear over New England is not as strong in the nondivergent case.

Fig. 9b is the balanced height field obtained from the nondivergent winds of Fig. 9a. When compared with the observed heights (Fig. 8b), the balanced heights are smoother, the trough is broader, the height at the center of the closed low is 21 m higher, and the height gradient southeast of the trough is slightly weaker.

The balanced temperatures are given in Fig. 9c. When compared with the observed temperatures (Fig. 8d), we note the same kinds of differences as in the height fields. For the balanced temperatures, the trough is warmer, the horizontal temperature gradient north of New England is weaker, and the ridge over the Southeast is slightly warmer.

4.2 The synoptic situation at 00201175

Relatively rapid changes occurred between 12191175 and 00201175. A low developed over the Texas panhandle and moved as well as deepened

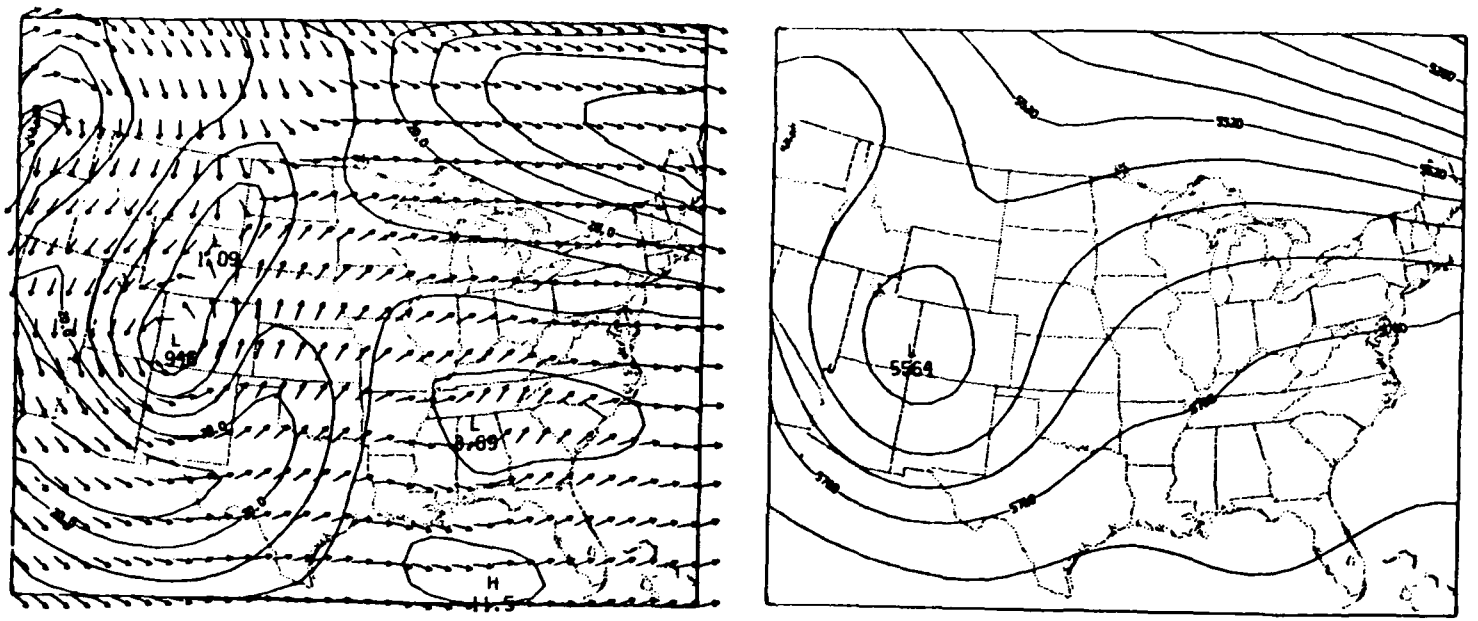

a. Nondivergent winds. The contour interval is 5 m s^{-1}.

b. Balanced 500-mb heights. The contour interval is 60 m.

Fig. 9. 500-mb fields used for the standard nondivergent initialization at 12191175.

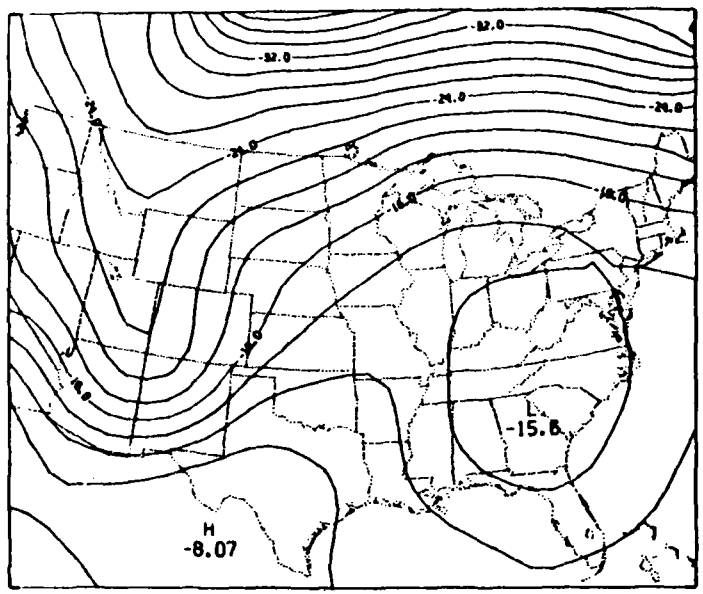

c. Derived temperatures. The contour interval is 2°C.

Fig. 9. (Continued).

rapidly to a 1004-mb low over eastern Kansas at 00201175 (Fig. 10a). The trough now extends from south Texas through the Kansas low and then through Lake Huron and into New England. The cold air has now penetrated into the northern Rocky Mountain states and the surface pressure gradient from Wyoming to Kansas is much stronger than 12 hours before.

From the observed height field in Fig. 10b, we see the closed low has moved eastward to southwest Kansas at a speed of about 17 m s^{-1}. The height of the low center fell about 40 m. The height gradient to the southeast of the trough has strengthened. This is reflected in the wind speeds and directions in Fig. 10c. The wind maximum previously over southern California has increased nearly 12 m s^{-1} while moving around the southern end of the trough and is now centered over Abilene, Texas. Precipitation occurred on the cold side and ahead of this jet streak. Also note that the wind maximum north of Maine has increased in intensity. The position of this maximum was probably responsible for the precipitation which occurred in the western Great Lakes region.

The temperature field (Fig. 10d) shows an increased temperature gradient to the south and southeast of the trough with the cold air advancing over Kansas and Oklahoma while the relatively warm air still resides over the Midwest.

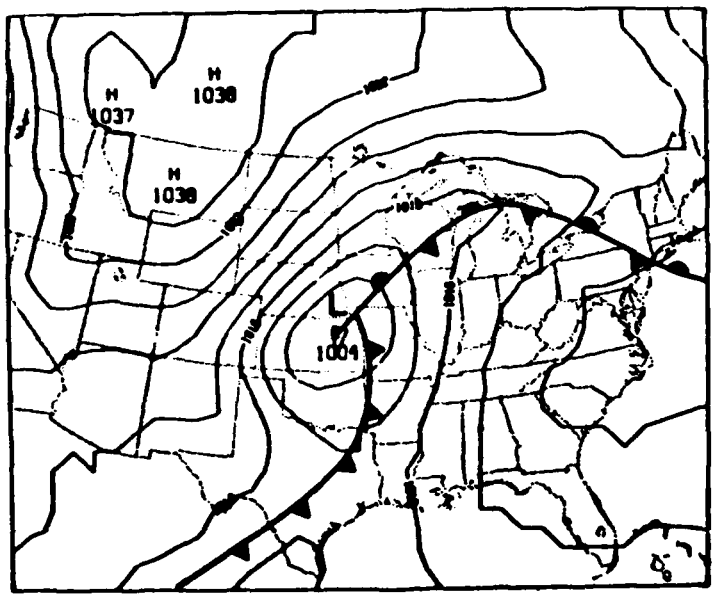

a. Sea level pressure. Surface fronts are indicated. The contour interval is 4 mb.

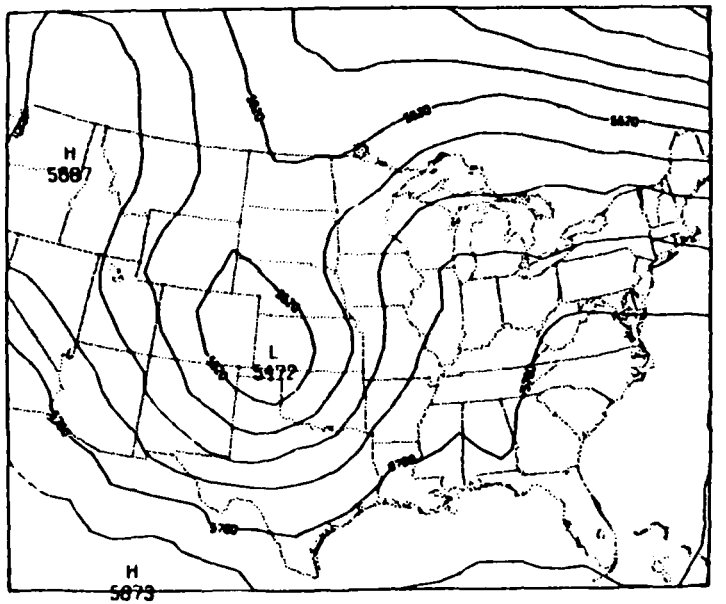

b. 500-mb heights. The contour interval is 60 m.

Fig. 10. Observed fields at 00201175.

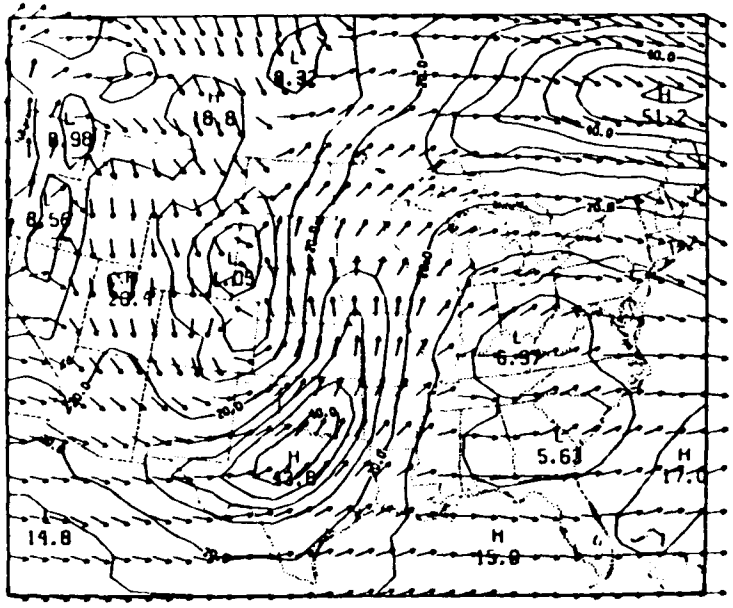

c. 500-mb winds. The contour interval is 5 m s^{-1}.

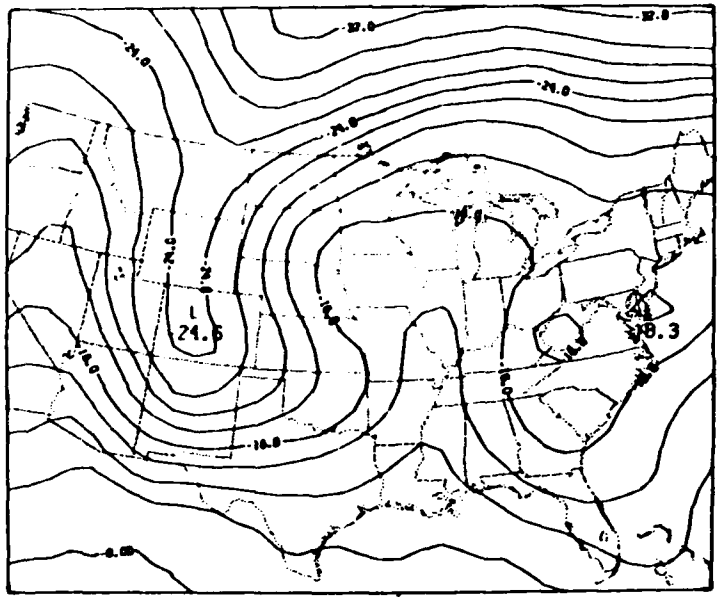

d. 500-mb temperatures. The contour interval is 2°C.

Fig. 10. (Continued).

4.3 The observed precipitation amounts

Precipitation data for the period 12191175 to 00201175 were extracted from the National Climatic Center's November, 1975, Hourly Precipitation Data (Volume 25, Number 11) booklets for each state. For each hour, the data were analyzed at grid points using a Cressman (1959) scan with a radius of influence of 1.0.

The total precipitation for the first three hours (12 GMT to 15 GMT, 19 November 1975) is given in Fig. 11a and the total precipitation for the 12-hour period is given in Fig. 11b. We observe that the heaviest 12-hour precipitation (just over 2.5 cm) occurred from south central Nebraska to northwestern Kansas.

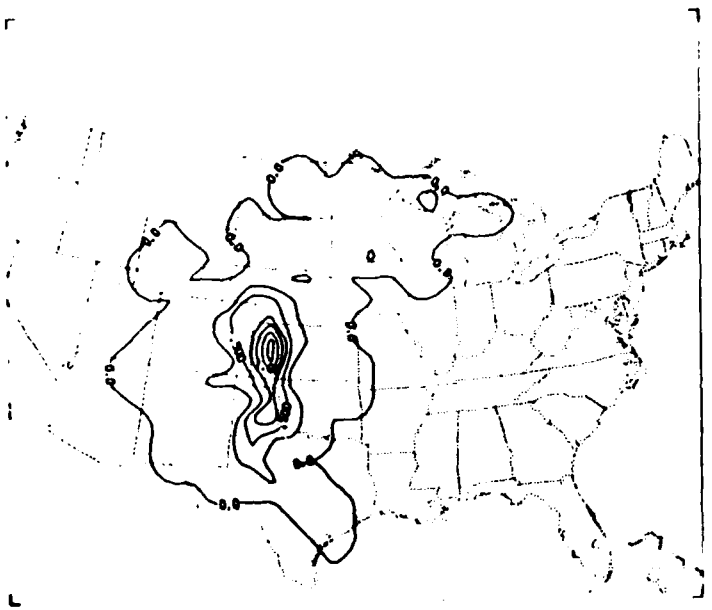

a. 12191175 to 15191175. The maximum rainfall amount is about 1.5 cm in west central Kansas. The contour interval is 0.25 cm.

b. 12191175 to 00201175. The highest rainfall amount is about 2.6 cm in south central Nebraska and northwestern Kansas. The contour interval is 0.5 cm.

Fig. 11. Observed precipitation fields.

5.0 USE OF THE OMEGA EQUATION IN THE DETERMINATION OF THE DIVERGENT WIND COMPONENT

The first objective of this chapter is to review previous work on the use of the omega equation to diagnose vertical velocities. Then we will derive the finite-difference (FD) version of (2.23), the mesoscale omega equation. The FD omega equation will then be applied to the 12191175 data described in Chapter 4. Experiments will be performed to confirm the validity of the relative order of magnitude of the terms in (2.23). Finally, sensitivity experiments will be conducted which will provide information on how accurately the divergent wind component can be determined.

5.1 Previous diagnostic studies using the omega equation

The omega equation equivalent to that of Krishnamurti (1968a) can be written:

$$\begin{aligned} &\underset{\text{T1}}{\nabla^2(\sigma_s \omega)} + \underset{\text{T2}}{f^2 \frac{\partial^2 \omega}{\partial p^2}} = \underset{\substack{\text{T3}\\ \text{I,I,I}}}{f \frac{\partial}{\partial p} \underset{\sim}{V}_{\psi} \cdot \nabla \zeta} + \underset{\substack{\text{T4}\\ \text{II,II,III}}}{f \frac{\partial}{\partial p} \underset{\sim}{V}_{\chi} \cdot \nabla \zeta} \\ &\quad + \underset{\substack{\text{T5}\\ \text{I,I,I}}}{\frac{R}{p} \nabla^2 \underset{\sim}{V}_{\psi} \cdot \nabla T} + \underset{\substack{\text{T6}\\ \text{II,II,III}}}{\frac{R}{p} \nabla^2 \underset{\sim}{V}_{\chi} \cdot \nabla T} - \underset{\substack{\text{T7}\\ \text{II,II,II}}}{f \frac{\partial}{\partial p} \zeta D} + \underset{\substack{\text{T8}\\ \text{II,II,III}}}{f \frac{\partial}{\partial p} \omega \frac{\partial \zeta}{\partial p}} \end{aligned} \tag{5.1}$$

$$+ f \frac{\partial}{\partial p} \nabla\omega \cdot \nabla \frac{\partial \psi}{\partial p} - \frac{R}{c_p p} \nabla^2 Q + f \frac{\partial}{\partial p} g \frac{\partial}{\partial p} \nabla \times \underset{\sim}{\tau}$$

T9 T10 T11

II,II,III I,I,I II,II,II

$$- \frac{R}{c_p p} \nabla^2 H_s - 2 \frac{\partial}{\partial t} \frac{\partial}{\partial p} J\left(\frac{\partial \psi}{\partial x}, \frac{\partial \psi}{\partial y}\right) - \beta \frac{\partial}{\partial p} \frac{\partial}{\partial y} \frac{\partial \psi}{\partial t} \qquad (5.1)\ \text{(cont.)}$$

T12 T13 T14

X,IV,X X,II,X X,III,X

where H_s is the sensible heat added per unit time from a water surface. Note that terms T1 through T11 correspond exactly to those of (2.23) except that Krishnamurti assumes $\zeta << f$ in T2. Under each term in (5.1), the first Roman numeral is the order of magnitude of that term from the scale analysis of Chapter 2 (X indicates not given). Krishnamurti found that T12 was small except over large water bodies and hence T12 will not be discussed here. Terms T13 and T14 correspond to terms T13 and T14, respectively, of (2.19), and were assumed to cancel in (2.23) by virtue of the geostrophic vorticity assumption.

Krishnamurti (1968b) applied (5.1) on a 2.5-degree latitude by 2.0-degree longitude grid for four synoptic times covering the development of a cyclone in mid-latitudes. To examine the magnitude of omega, he chose eight points in the vicinity of a 500-mb trough at one of the four synoptic times. First, the omega values at the eight points were computed and then averaged. From this average value, the relative order of importance to the total omega of each term is given as the second Roman numeral under each forcing function in (5.1). We note that the relative importance of each term found

by Krishnamurti is exactly that determined by the scale analysis for synoptic scales (Krishnamurti's average grid increment was about 200 km). He also pointed out that T8 and T9 tend to cancel and, to a lesser extent, so do T4 and T6. The largest vertical velocity found at any point was at a point where the latent heating contribution was the largest.

Baumhefner (1968) used Krishnamurti's (1968a) diagnostic model in the tropics on a 2.0-degree latitude by 2.0-degree longitude grid. He studied an easterly wave spanning four synoptic times in August, 1961. The third set of Roman numerals under the terms on the RHS of (5.1) were Baumhefner's results at the 500-mb level. We see that terms T4, T6, T8, T9, and T13 were found to be an order of magnitude smaller than Krishnamurti's results.

Hawkins (1972) developed a diagnostic model for computing omega which he applied to three disparate cases on a 206-km grid mesh. He reported that the omega values obtained from the complete, relatively sophisticated model were similar to the first-guess values diagnosed with the quasi-geostrophic omega equation with the latent-heating term added. That is, Hawkins' findings agreed with the other researchers.

In summary, we conclude that previous research supported the scale analysis used in Section 2.1 in the determination of the omega equation appropriate on the synoptic scale. When the FD form of the mesoscale omega equation is applied to the 12191175 data, we expect the relative importance of the terms will be the same as that indicated by the scale analysis for the mesoscale.

5.2 Derivation of the finite-difference (FD) form of the omega equation

Before we can present or discuss FD equations, we need to define some FD operations. We use Shuman and Hovermale's (1968) notation for the FD operators

$$\alpha_x \equiv (\alpha_{i,j+\frac{1}{2}} - \alpha_{i,j-\frac{1}{2}})/\Delta x \tag{5.2a}$$

$$\alpha_y \equiv (\alpha_{i+\frac{1}{2},j} - \alpha_{i-\frac{1}{2},j})/\Delta y \tag{5.2b}$$

$$\overline{\alpha}^x \equiv (\alpha_{i,j+\frac{1}{2}} + \alpha_{i,j-\frac{1}{2}})/2 \tag{5.2c}$$

$$\overline{\alpha}^y \equiv (\alpha_{i+\frac{1}{2},j} + \alpha_{i-\frac{1}{2},j})/2 \tag{5.2d}$$

where j is the east-west index and i is the north-south index.

We will use the "four-point" operators

$$\overline{\overline{\alpha}}^y \equiv (\alpha_{i+1,j} + 2\alpha_{i,j} + \alpha_{i-1,j})/4 \tag{5.3a}$$

$$\overline{\overline{\alpha}}^x \equiv (\alpha_{i,j+1} + 2\alpha_{i,j} + \alpha_{i,j-1})/4 \tag{5.3b}$$

Vertical differences and averages are defined by

$$\overline{\alpha}^\sigma \equiv (\alpha_{k+\frac{1}{2}} + \alpha_{k-\frac{1}{2}})/2 \tag{5.4a}$$

$$\delta\alpha \equiv (\alpha_{k+\frac{1}{2}} - \alpha_{k-\frac{1}{2}}) \tag{5.4b}$$

Omega will be calculated on a 30 by 35 by 7 grid. Each 30 by 35 horizontal section has a grid increment of 120 km and is centered at 41N and 95W. Fig. 12 illustrates the vertical structure of the omega equation domain. Note that velocity, temperature, omega, and static stability are defined at standard constant-pressure levels while the forcing functions for the three-dimensional relaxation are defined at the mid-levels.

Because the derivation of the FD form of the omega equation is long and detailed, it is presented in Appendix 1.

5.3 Application of the FD omega equation to the 12191175 data

In this section we will use the FD omega equation to compute omega values for the 12191175 data set. We will first examine the diabatic term. Then we will try to determine to what accuracy the vertical velocities can be determined.

5.3.1 The diabatic term and the parabolic omega profile

As described in Appendix 1, we use a parabolic omega profile and the observed rain rate to calculate omega values due to the diabatic term only. Hereafter, these omega values will be termed convective omegas.

Since precipitation amounts were measured hourly at synoptic stations, and since a rainfall rate valid at 12191175 was desired, rainfall amounts from 2 hours before and 2 hours after 12191175 were averaged to obtain a more representative rainfall rate. Fig. 13 presents that precipitation rate in cm d^{-1}.

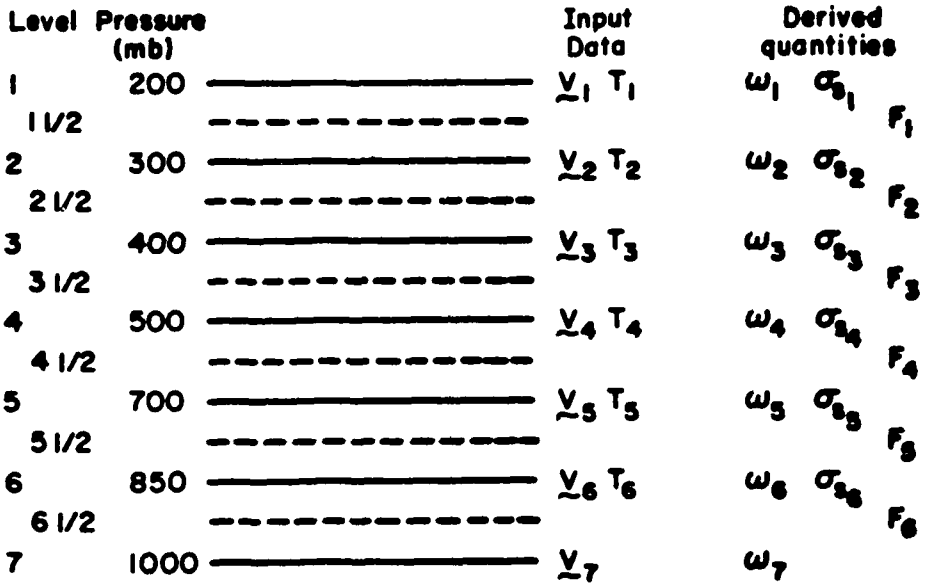

Fig. 12. Vertical structure of grid used to calculate the omega field. The forcing functions F are calculated at half levels and omega is obtained at the standard pressure levels.

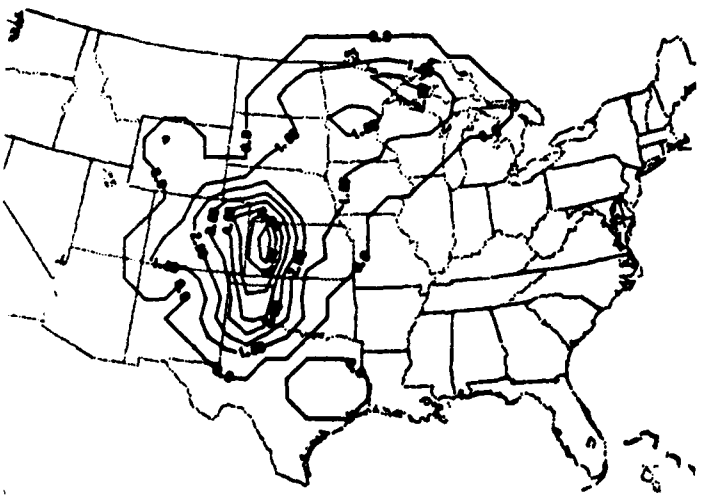

Fig. 13. Observed rainfall rate in cm d^{-1} valid at 12191175. This rate was derived from the observations for the period 10191175 to 14191175. The contour interval is 1 cm d^{-1}.

We should mention here that observed precipitation rates, the input data for the omega equation diabatic term, can be obtained from other than rainguage measurements. For the eastern US, rain rates can be obtained from NWS manually digitized radar (MDR) data (Moore et al., 1974). Over the oceans, meteorological satellites have provided precipitation rate observations (Adler and Rodgers, 1977). A scanning microwave radiometer on the satellite measures a "brightness" temperature. The dominating factor in the determination of this temperature over water is liquid water drops of rainfall size. The brightness temperatures are then translated into rainfall rates using previously derived rainfall rate-brightness temperature relationships. In the future, satellites may also provide rainfall rates over land. Therefore, satellites provide a means of obtaining data required for the diabatic term.

We will use the rainfall rate in Fig. 13 in the solution of the finite-difference form of the omega equation. Before solving the entire equation, we will conduct four experiments to determine convective omegas. The purpose of these experiments is to determine the effect of uncertainty in the observed rainfall rate and the effect of including a terrain-induced omega as the lower boundary condition for the parabolic omega profile.

Table 5 gives a summary of the convective omega experiments. The column labeled "RAMT" is the fraction of the rainfall amount of Fig. 13 that was used for that particular experiment. Fig. 14 is the 500-mb convective omega field for Experiment 5.1. The purpose of Experiments 5.1 through 5.3 was to determine if there exists a significant variability in the omega values calculated for the computational domain

Table 5. Summary of convective omega experiments.

Experiment Number	RAMT (fraction of Fig. 13 rain rate used)	ω_t Included	$\lvert\bar{\omega}\rvert$ ($cb\ d^{-1}$)	
			500 mb	850 mb
5.1	1.0	yes	13.7	8.5
			RMS difference in omega ($cb\ d^{-1}$) from Experiment 5.1	
			500 mb	850 mb
5.2	0.90	yes	1.38	0.90
5.3	0.75	yes	3.45	2.24
5.4	1.0	no	0.29	1.58

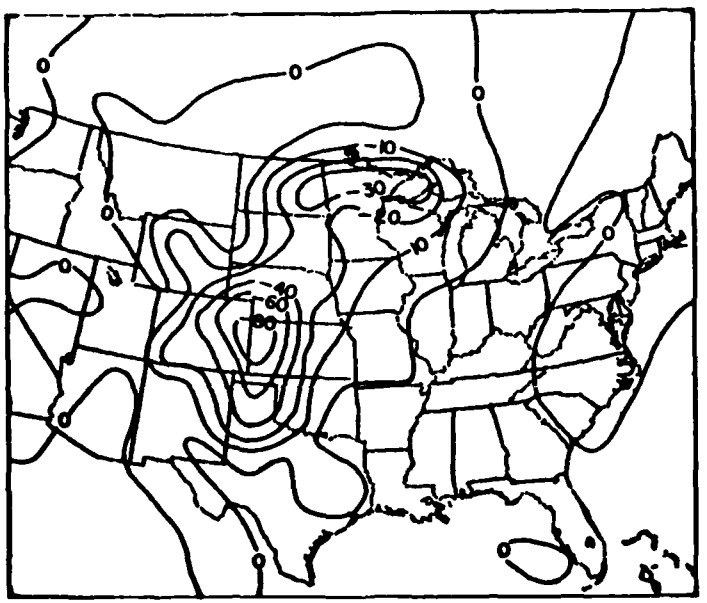

Fig. 14. 500-mb convective omega field in cb d^{-1} from Experiment 5.1. This field was derived from the observed rain rate and the assumed parabolic omega profile.

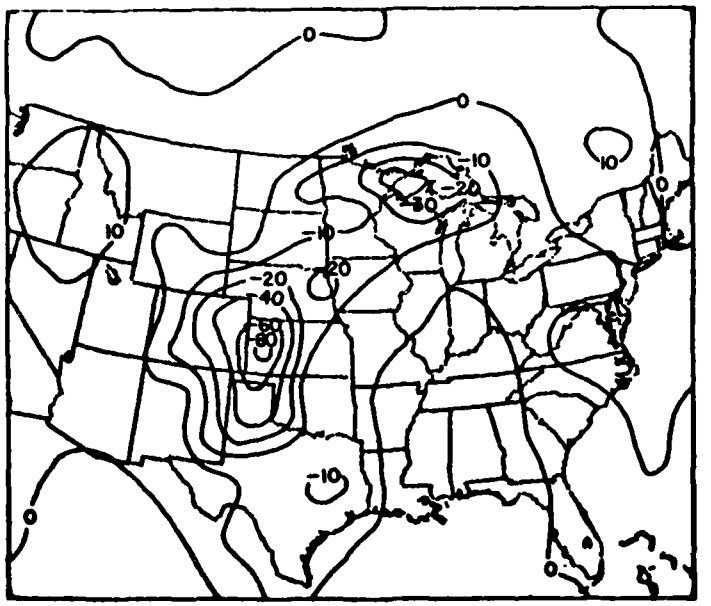

Fig. 15. 500-mb omega field in cb d^{-1} from Experiment 5.5. This field was obtained from the complete mesoscale omega equation.

at 500 mb when the precipitation rate was altered. Since precipitation amounts over large areas are determined by very few observations in time and space, the precipitation amounts themselves at grid points possess a sizable uncertainty. This uncertainty is largest in areas of strong convective activity. A 25 percent difference between the "observed" precipitation amount and the precipitation amount that would be representative of a grid square can easily be imagined. For a 25 percent error in precipitation rate (represented by Experiment 5.3), there was approximately a 20 percent error in the 500-mb RMS omega value over the entire domain. Therefore, the significance of the diabatic term was critically dependent on the accuracy of the rainfall amounts themselves. Experiment 5.4 demonstrated that when terrain-induced omega values were not used as the lower boundary condition, there was only a small effect at 500 mb but there was a significant effect at 850 mb. We conclude that the terrain effect did indeed produce significantly different omegas in the lower levels. Terrain-induced omegas should be used since they are consistent with the forecast model which contains variable terrain.

5.3.2 Experiments with various terms in the FD omega equation

Experiment 5.5 consisted of obtaining omega values using the finite-difference version of (2.23), the mesoscale omega equation. The resultant 500-mb omega values are presented in Fig. 15. From the figure we can see the strong influence of the diabatic term over eastern Colorado, the Texas panhandle to southwestern Nebraska, and over Lake Superior and vicinity.

Several experiments were performed to support the scale analysis used in obtaining (2.23). For example, experiments were completed with the quasi-geostrophic omega equation, with differential vorticity advection only, and with the Laplacian of temperature advection only. From these experiments the following conclusions were reached:

(1) The omega equation experiment without a diabatic term greatly underestimated the omega values in the precipitation areas. In fact, the diabatic term was the largest single term in the areas of precipitation. Therefore, a diabatic term must be included on the mesoscale.

(2) The quasi-geostrophic omega equation with a diabatic term overestimated the omega values in the precipitation areas.

(3) An experiment with random uncertainty in the wind field produced only small RMS changes in the omega values.

(4) The scale analysis in Section 2.1.4 was supported. That is, the various forcing functions had the expected relative influence on the omega values. Therefore, (2.23) is an appropriate form of the omega equation for the mesoscale.

(5) An experiment was conducted in which the precipitation rate used for the diabatic term was 25 percent less than that for Experiment 5.5. At 500 mb, the RMS difference between this experiment and Experiment 5.5 was 15 percent of the mean absolute value of omega for the entire field. At 600 mb, this produced a 10 and 15 percent RMS difference in u_χ and v_χ, respectively. That is, with a reasonable estimate of the uncertainty inherent in

precipitation observations, the percentage change in the divergent wind components was almost as large.

The omega values used to determine the divergent wind component were those from Experiment 5.5. Then, to obtain velocity potential, the method described in Section 2.3.4 was applied with the boundary normal derivative adjusted for 100 iterations. The resultant divergent wind fields for the 925-, 775-, 350-, and 250-mb levels are given in Fig. 16. In Fig. 16a, there is a narrow zone of convergence from central Wisconsin to southwestern Kansas and on toward the south. This same pattern is evident at the 775-mb level (Fig. 16b). The low-level convergence is supported by the divergence aloft depicted in Figs. 16c and 16d. The zone of divergence extends from Lake Superior to western Kansas and to the south. The divergent wind fields appear to be vertically consistent. In Chapter 7, we will see if the region of maximum vertical motion is reflected in the forecast started from a divergent initialization.

In the next chapter, the FD form of the balance equation which will be used in the divergent initialization will be derived.

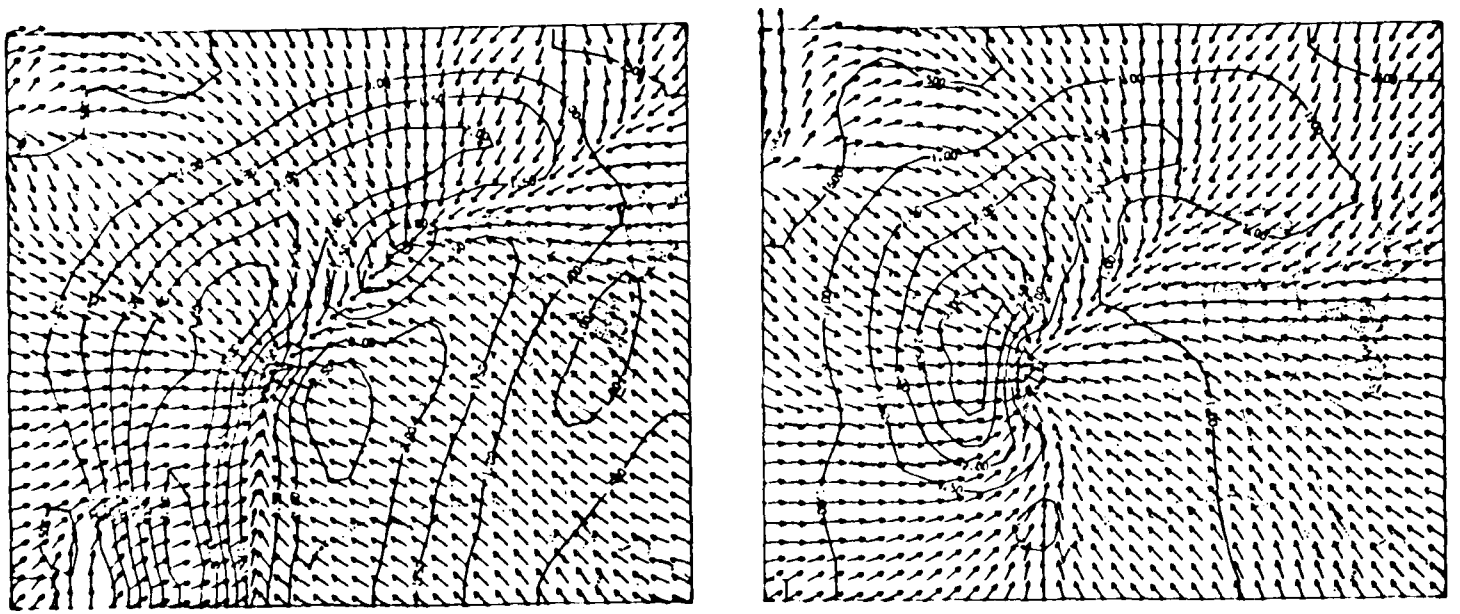

a. 925-mb level.

b. 775-mb level.

Fig. 16. Divergent wind fields at 4 constant-pressure levels from Experiment 5.5. The contour interval is 0.5 m s^{-1}.

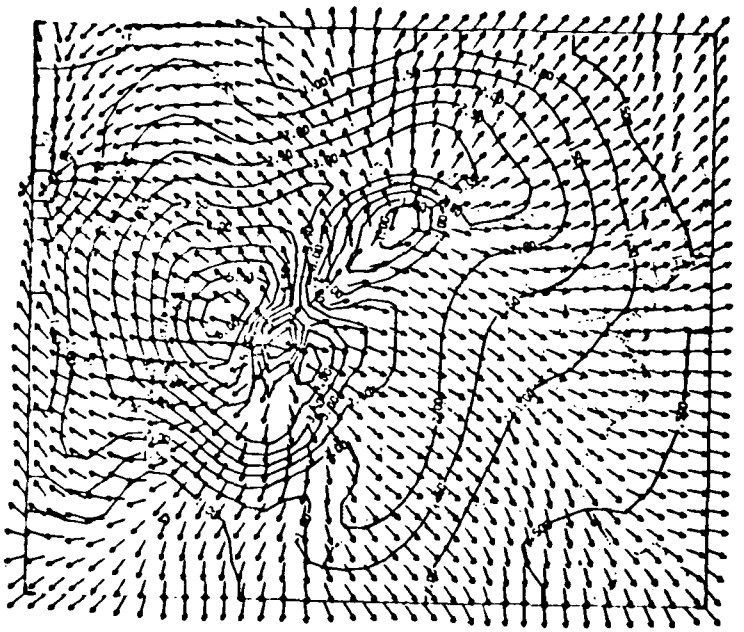

c. 350-mb level.

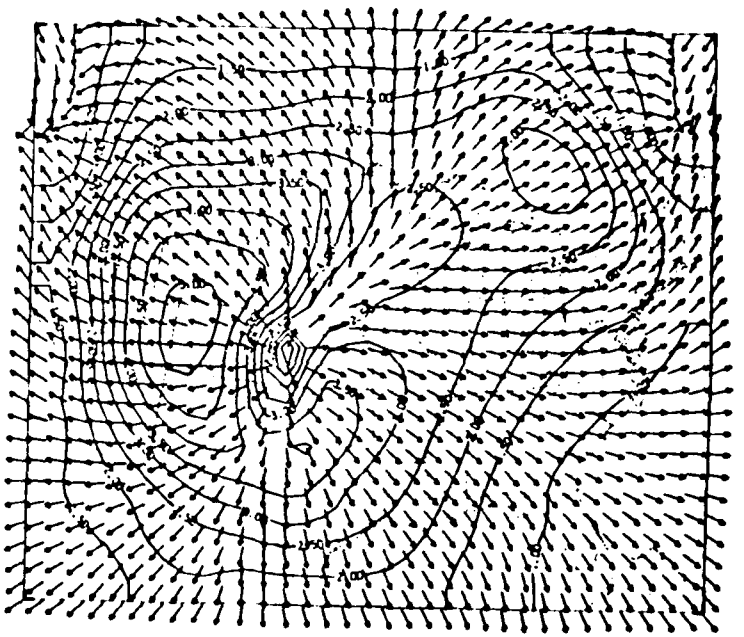

d. 250-mb level.

Fig. 16. (Continued).

6.0 DERIVATION OF THE FINITE-DIFFERENCE (FD) BALANCE EQUATION

The purpose of this chapter is to derive the FD form of the balance equation to be used for the divergent initialization of the PSU model. The balance equation in sigma coordinates appropriate for this purpose is given by (2.31).

At this point we will examine how balance equations in general have been used in the initialization of numerical models. The common practice, especially on the large scale, has been to use observed geopotentials and solve the balance equation for stream function. For example, this procedure was used by Sundqvist (1975). There are, however, at least two reasons why an alternative approach should be employed.

First, Paegle and Paegle (1976) reported that, for the year beginning 1 June 1969, virtually every Northern Hemisphere 200-mb chart exhibited nonelliptic geopotential data at some points. The nonelliptic geopotentials were especially prevalent in the summer above severe weather events. The balance equation was not solvable in regions where the geopotentials are nonelliptic and some approximation must be made there.

Second, WAM, Fankhauser (1974), and AW have pointed out that typical errors in surface pressure and rawinsonde temperatures led to large errors in the horizontal gradients of geopotential heights on the mesoscale (10-100 km). Fankhauser reported that errors in height observations of more than 30 m were common on the mesoscale. Therefore, we will follow WAM and supply the nondivergent wind to the

balance equation and solve for geopotential. We now proceed to the derivation of the FD balance equation.

One possible approach for the FD form of the balance equation would be to write each term of (2.31) directly in its FD form. Although that approach is conceptually simple and relatively easy to do, it will not be used here. One objective of any balancing scheme should be to retain the maximum degree of consistency with the model being initialized. This should help minimize noise generated during the adjustment phase of the prediction. That is, the more consistency between the initialization scheme and the model, the nearer the balanced initial conditions are to those conditions exactly compatible with the model. Therefore, we will derive the FD form of the balance equation directly from the model FD equations themselves. In this chapter, we will present the PSU model FD equations, derive the consistent FD balance equation, and outline how the equation should be used in the initialization procedure.

6.1 The PSU model FD equations

AW provide the complete set of the FD model equations, and most will not be repeated here. We present only those which are essential to this chapter.

The finite-difference equations associated with the u and v component equations of motion (minus those terms which do not correspond to a term in (2.28)) are:

$$0 = -m^2\left[\left(\overline{u^x}\,\overline{\overbrace{\frac{p_* u}{m}}^{y}}^{x}\right)_x + \left(\overline{u^y}\,\overline{\overbrace{\frac{p_* v}{m}}^{x}}^{y}\right)_y\right] - \frac{\delta\left(\dot{\sigma}^{xy}\,\overline{p_* u}^{\sigma}\right)}{\delta\sigma}$$

T1 T2 T3

$$- m\overline{p_*}^{xy}\,\overline{\phi}_x^{y} - \frac{mR\overline{T}^{xy}\,\overline{p_*}_x^{y}}{1 + \dfrac{p_t}{\sigma\overline{p_*}^{xy}}} + fp_* v \qquad (6.1)$$

T4 T5 T6

$$0 = -m^2\left[\left(\overline{v^x}\,\overline{\overbrace{\frac{p_* u}{m}}^{y}}^{x}\right)_x + \left(\overline{v^y}\,\overline{\overbrace{\frac{p_* v}{m}}^{x}}^{y}\right)_y\right] - \frac{\delta\left(\dot{\sigma}^{xy}\,\overline{p_* v}^{\sigma}\right)}{\delta\sigma}$$

T7 T8 T9

$$- m\overline{p_*}^{xy}\,\overline{\phi}_y^{x} - \frac{mR\overline{T}^{xy}\,\overline{p_*}_y^{x}}{1 + \dfrac{p_t}{\sigma\overline{p_*}^{xy}}} - fp_* u \qquad (6.2)$$

T10 T11 T12

where the terms $p_* u$ and $p_* v$ represent $\overline{up_*}^{xy}$ and $\overline{vp_*}^{xy}$, respectively.

The FD form of the continuity equation is

$$\frac{\partial p_*}{\partial t} = -\left(\overline{m}^{xy}\right)^2\left[\left(\frac{\overline{p_* u}^{y}}{m}\right)_x + \left(\frac{\overline{p_* v}^{x}}{m}\right)_y\right] - p_* \frac{\delta\dot{\sigma}}{\delta\sigma} \quad . \qquad (6.3)$$

The FD equation relating omega and $\dot{\sigma}$ is

$$\omega = p_*\dot{\sigma} + \left(\frac{\partial p_*}{\partial t} + \overline{u}^{xy}\,\overline{p_*}_x^{x} + \overline{v}^{xy}\,\overline{p_*}_y^{y}\right) \quad . \qquad (6.4)$$

Finally, the hydrostatic equation is

$$\frac{\partial \phi}{\partial \ln(\sigma + p_t/p_*)} = - R\overline{T}^{\sigma} \quad . \tag{6.5}$$

6.2 Derivation of the FD balance equation for the PSU model

We know that a divergence equation can be formed from the u and v equations of motion by operating on the u equation with $\frac{\partial}{\partial x}$ and on the v equation with $\frac{\partial}{\partial y}$ and summing the result. To form the FD balance equation, the procedure must be slightly modified. In the p_*u and p_*v component equations, each individual term is defined at a dot point because p_*u and p_*v are defined at dot points. However, we will use the balance equation to solve for geopotential and on the staggered grid, geopotential is defined at cross points. Therefore, in deriving the balance equation, we must make a modification such that the terms are defined at cross points rather than dot points.

The result of differentiation of Tl in (6.1) with respect to x is Tl_x in FD notation. However, the resultant derivative applies midway between dot points. In order for the derivative to apply at the desired cross point, Tl must first be averaged in the y direction (FD operation $\overline{Tl}^y$). For Tl at point (i,j), the result of $(\overline{Tl}^y)_x$ applies at cross point $(i+\frac{1}{2}, j+\frac{1}{2})$ as desired, where integer values of i and j refer to dot points. To summarize, the desired balance equation is derived by first dividing (6.1) and (6.2) by mp_*. Eqs. (5.2d) and then (5.2a) are applied to (6.1) and that result is added to the result of applying (5.2c) and then (5.2b) to (6.2). Transposing the

terms containing geopotential to the LHS of the equation yields equation (6.6), the complete FD balance equation.

$$\overline{(\overline{\phi_x}^{\,y})}_x + \overline{(\overline{\phi_y}^{\,x})}_y = -\Bigg[\overline{\left(\frac{m}{\overline{p_*}^{xy}}\,\overline{(\overline{u}^{\,x}\,\overline{\frac{p_* u}{m}}^{\,y})}_x\right)}^{\,x}\Bigg]_x$$

T1 T2 T3

$$+\overline{\left(\frac{m}{\overline{p_*}^{xy}}\,\overline{(\overline{u}^{\,y}\,\overline{\frac{p_* v}{m}}^{\,x})}_y\right)}^{\,y}{}_x + \overline{\left(\frac{m}{\overline{p_*}^{xy}}\,\overline{(\overline{v}^{\,x}\,\overline{\frac{p_* u}{m}}^{\,y})}_x\right)}^{\,x}{}_y$$

T4 T5

$$+\Bigg[\overline{\left(\frac{m}{\overline{p_*}^{xy}}\,\overline{(\overline{v}^{\,y}\,\overline{\frac{p_* v}{m}}^{\,x})}_y\right)}^{\,x}{}_y\Bigg] + \overline{\left(\frac{1}{m\overline{p_*}^{xy}}\,\frac{\delta(\overline{\sigma}^{xy}\,\overline{p_* u}^{\sigma})}{\delta\sigma}\right)}^{\,y}{}_x \qquad (6.6)$$

T6 T7

$$-\overline{\left(\frac{1}{m\overline{p_*}^{xy}}\,\frac{\delta(\dot{\overline{\sigma}}^{xy}\,\overline{p_* v}^{\sigma})}{\delta\sigma}\right)}^{\,x}{}_y - \overline{\left(\frac{\overline{RT}^{xy}\,\overline{p_*}^{y}{}_x}{\overline{p_*}^{xy}\,(1+\frac{p_t}{\sigma\overline{p_*}^{xy}})}\right)}^{\,y}{}_x$$

T8 T9

$$-\overline{\left(\frac{\overline{RT}^{xy}\,\overline{p_*}^{x}{}_y}{\overline{p_*}^{xy}\,(1+\frac{p_t}{\overline{p_*}^{xy}})}\right)}^{\,x}{}_y + \left(\frac{\overline{fp_* v}^{\,y}}{m\overline{p_*}^{xy}}\right)_x - \left(\frac{\overline{fp_* u}^{\,x}}{m\overline{p_*}^{xy}}\right)_y$$

T10 T11 T12

For a nondivergent initialization on sigma surfaces, the u and v appearing in terms T3 through T6 represent the nondivergent wind components u_ψ and v_ψ, respectively. For a divergent initialization on sigma surfaces, terms T3 through T6 are each applied three times because the u and v in those terms represent the total wind components. That is,

$$u = u_\psi + u_\chi \tag{6.7a}$$

and

$$v = v_\psi + v_\chi \quad . \tag{6.7b}$$

For example, if we use functional notation to express T3 as a function of u and p_*u, then we can write T3 as

$$T3 = f(u, p_*u) \quad . \tag{6.8}$$

Substitution of (6.7a) into (6.8) produces

$$T3 = f(u_\psi, p_*u_\psi) + f(u_\psi, p_*u_\chi) + f(u_\chi, p_*u_\psi) + f(u_\chi, p_*u_\chi) \quad . \tag{6.9}$$

The fourth term in (6.9) is neglected because the scale analysis of Chapter 2 indicates that it is two orders of magnitude smaller than the first term. The three applications of T3 required by divergent

initialization on sigma surfaces are represented by the first three terms of (6.9). We write these terms as

$$T31 = f(u_{\psi}, p_{*}u_{\psi})$$

$$T32 = f(u_{\psi}, p_{*}u_{\chi})$$

$$T33 = f(u_{\chi}, p_{*}u_{\psi}) \quad .$$

Similarly, for terms T4 through T6, we can write

$$T41 = f(u_{\psi}, p_{*}v_{\psi})$$

$$T42 = f(u_{\psi}, p_{*}v_{\chi})$$

$$\vdots$$

$$T62 = f(v_{\psi}, p_{*}v_{\chi})$$

$$T63 = f(v_{\chi}, p_{*}v_{\psi}) \quad .$$

It is important to realize that the "nondivergent" or "divergent" velocity components refer to pressure surfaces even though the model is formulated on sigma surfaces. We calculate the velocity components on pressure surfaces and interpolate them to sigma surfaces. We do

not compute χ or ψ on sigma surfaces. Thus in the "nondivergent" initialization, $\nabla_p \cdot \underset{\sim}{V} = 0$ but $\nabla_\sigma \cdot \underset{\sim}{V}$ does not equal zero because of the slope of sigma surfaces over variable terrain.

Performing the above FD operations on the terms of (6.6) is a long, complex, and tedious enterprise and is therefore presented in Appendix 2.

6.3 Application of the FD balance equation

To apply (6.6), we need $\dot{\sigma}$ at σ levels and cross points, T at half-sigma levels and cross points, and u_ψ, u_χ, v_ψ, v_χ, m, and f at half-sigma levels and dot points.

The available data consist of surface observations and observations on constant-pressure surfaces. Therefore, the data will be interpolated to sigma surfaces before applying (6.6). This will provide T at half-sigma levels. We obtain u_χ and v_χ at half-sigma levels by interpolating the divergent components computed in Chapter 5 from constant pressure to sigma levels. We will use the observed u and v at pressure levels in

$$\nabla^2 \psi = \frac{\zeta}{m} \tag{6.10}$$

to obtain ψ at the mandatory pressure levels. The resultant nondivergent wind components are then interpolated to the half level sigma surfaces.

To determine $\dot{\sigma}$, we first calculate $\frac{\partial p_*}{\partial t}$ from a finite-difference form of the vertical integral of mass divergence. Then, for each layer, we apply

$$\dot{\sigma}_{k+1} = \dot{\sigma}_k - \left(\frac{\partial p_*}{\partial t} + \overline{u^{xy}}_{k+\frac{1}{2}} \overline{p_{*_x}}^{x} + \overline{v^{xy}}_{k+\frac{1}{2}} \overline{p_{*_y}}^{y}\right) \frac{\sigma_{k+1} - \sigma_k}{p_*} \qquad (6.11)$$

to obtain $\dot{\sigma}$ at the full intermediate sigma levels. By definition, $\dot{\sigma}$ is zero at the top and bottom sigma levels. We have now defined all of the quantities necessary to use (6.6).

Once geopotentials have been obtained at all the half-sigma levels, (6.5) is used to obtain the balanced temperatures. The geopotential at the ground is known from the terrain elevation. The balanced temperatures are then interpolated to the half-sigma levels and the initialization process is completed.

7.0 DIVERGENT INITIALIZATION APPLIED TO A REAL DATA CASE

The purpose of this chapter is to discuss in detail, five 12-hour forecasts, all of which began at 12191175. Forecast 1 is initialized with unbalanced data. The observed winds and temperatures are interpolated from pressure to sigma surfaces and are inserted into the model with no other processing. Forecast 2 is initialized with unbalanced data but differs from Forecast 1 in that the winds are nondivergent. The nondivergent winds and observed temperatures are interpolated from pressure to sigma surfaces. Forecast 3 is initialized by the nondivergent balance method described in Chapter 3. That is, geopotentials are calculated on pressure surfaces via the balance equation, temperatures are derived hydrostatically, and these temperatures are interpolated to sigma surfaces. Forecast 4 follows a nondivergent initialization on sigma surfaces. Geopotentials are calculated on sigma surfaces using only the nondivergent wind. Balanced temperatures are derived and interpolated to sigma surfaces. Forecast 5 follows a divergent initialization on sigma surfaces. It is similar to Forecast 4 except that the terms in the balance equation containing the divergent wind components are also used and the divergent wind component obtained in Chapter 5 is added to the nondivergent wind to obtain the total wind field. Forecasts 1 and 2 are considered control experiments because they are unbalanced. Forecasts 3, 4, and 5 are balanced in different ways. Figs. 17 through 20 are flow charts illustrating how the various initializations proceed. Fig. 17 shows how the nondivergent wind components are

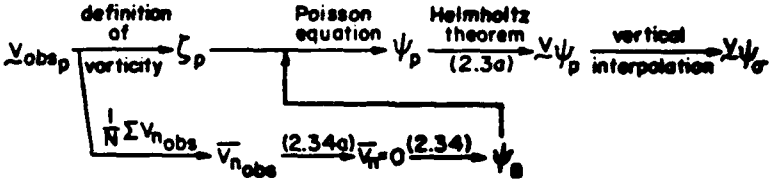

Fig. 17. Flow chart depicting the calculation of stream function on pressure surfaces and the nondivergent wind components on sigma surfaces.

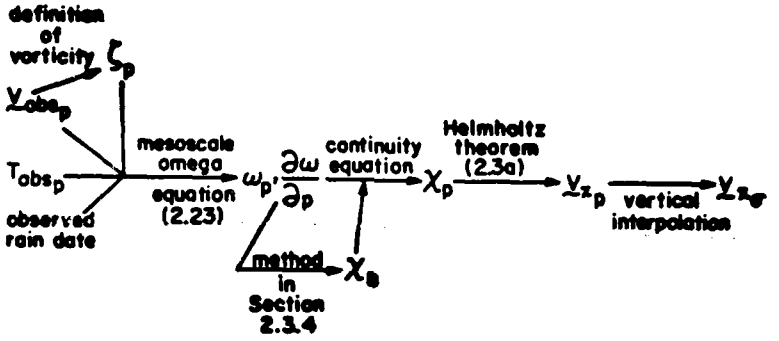

Fig. 18. Flow chart diagramming the calculation of omega on pressure surfaces and the divergent wind components on sigma surfaces.

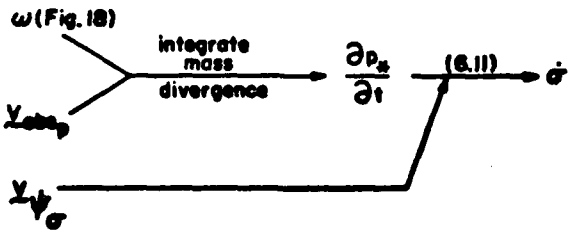

Fig. 19. Flow chart depicting the calculation of $\dot{\sigma}$.

calculated on sigma surfaces. Fig. 18 illustrates how the divergent wind components are obtained on sigma surfaces. In Fig. 19, we show how $\dot{\sigma}$ is calculated. Finally, in Fig. 20, we graphically compare the different initialization procedures. Although we are interested in all aspects of the results of the experiments, we will be primarily concerned with the initial precipitation amounts.

7.1 Initial conditions

In the three forecast experiments that were balanced (Forecasts 3, 4, and 5), a superadiabatic lapse rate occurred over much of the surface low pressure system (the eastern Rockies and the Plains states). In each initialization, geopotential is defined at the surface (sigma level 7). In Forecast 3, geopotential is calculated at 850 mb while in Forecasts 4 and 5, geopotential is calculated at sigma level 6½. Temperatures are then computed for the bottom layer from the hydrostatic equation. In each case, the lowest layer is about 500 m thick. One explanation for the superadiabatic lapse rates is the procedure used for the diagnosis of surface pressure. The initialization procedure uses temperature to diagnose surface pressure from sea level pressure in an iterative process using the hydrostatic equation. The sea level pressure observation was originally obtained from observed station pressure using the standard atmospheric lapse rate. Consequently, if the actual lapse rate is warmer (or colder) than the standard atmospheric lapse rate, the

a. Forecast 1.

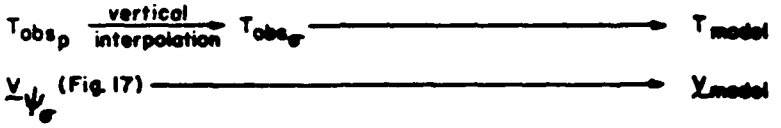

b. Forecast 2.

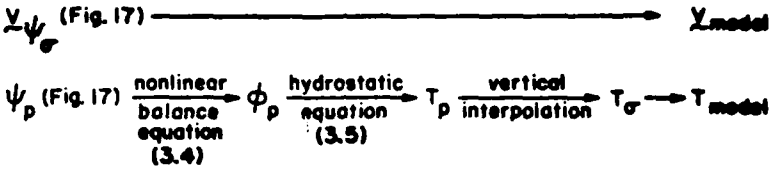

c. Forecast 3.

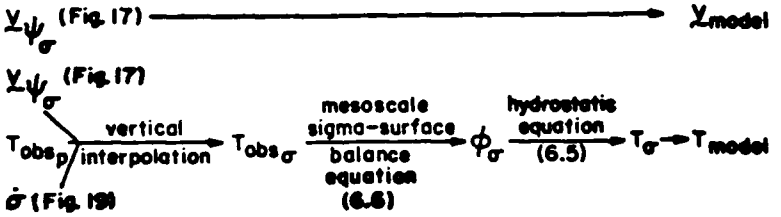

d. Forecast 4.

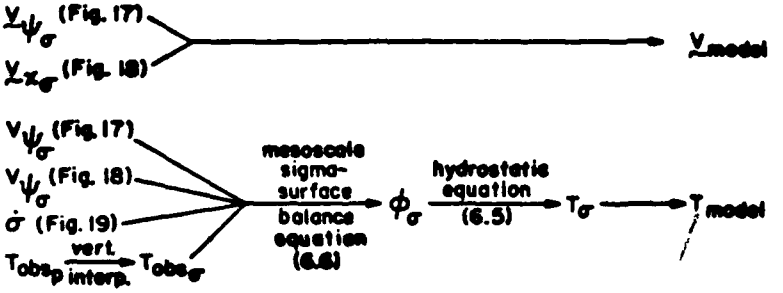

e. Forecast 5.

Fig. 20. Flow chart illustrating the differences in the initializations for the five forecast experiments.

diagnosed surface pressure will be higher (or lower) than the observed surface pressure. In this case, the surface pressure was underestimated in the vicinity of the low since the atmosphere was colder than the standard atmospheric lapse rate would predict for the 850 mb to surface layer.

Now we can examine typical errors in the temperature at the bottom level that could result if p_s or the geopotential at the lowest calculation level are in error. The finite-difference hydrostatic equation for $p_t = 0$ can be written:

$$\frac{\phi_{6\frac{1}{2}} - \phi_7}{\ln \frac{p_{6\frac{1}{2}}}{p_7}} = - R\overline{T} \tag{7.1}$$

where $\overline{T}$ applies at the logarithmic mean pressure of p_7 and $p_{6\frac{1}{2}}$, and the subscripts $6\frac{1}{2}$ and 7 refer to sigma levels $6\frac{1}{2}$ and 7, respectively. For p_7 = 1000 mb, a 10 m change in the geopotential at level $6\frac{1}{2}$ results in a two-degree change in the mean temperature of the layer. A 3-mb error in p_7 (p_s) results in a one-degree change in the mean temperature. Keyser (1978) reported that for a 925-mb height error of 10 m, the corresponding error in temperature for the 925-mb to surface layer is 3.8°C for SLP = 1013 mb and 4.4°C for SLP = 1000 mb. Keyser (personal communication) reported the occurrence of superadiabatic lapse rates (and not just in the lowest layer) in cases reported by Keyser (1978) and Anthes (1978). Barker* (personal communication) reported that areas with a superadiabatic lapse rate in the lowest layer occurred after balancing the initial conditions

*E. H. Barker, 1978, Naval Environmental Prediction Research Facility, Monterey, California.

for a global synoptic-scale primitive equation model. Hence, for thin layers especially, the hydrostatic equation is very sensitive to small errors in geopotential or surface pressure.

The atmosphere would not be expected to have a superadiabatic lapse rate over any large area. Hence the forecast model should not be provided with these erroneous lapse rates. Keyser and Barker (personal communication) recommended using a convective adjustment procedure at the end of the initialization. Although the balancing would be somewhat altered, the result is more realistic. Also, the presence of superadiabatic layers would artificially increase the initial precipitation rate. The convective adjustment procedure selected for use here is analogous to the one described by AW. Their scheme conserved the vertical integral of internal and potential energy.

The initial mean values of wind and temperature are given in Table 6. The temperatures for Forecasts 3, 4, and 5 apply after the convective adjustment was performed. The temperature changes produced by the convective adjustment procedure were several degrees at levels $5\frac{1}{2}$ and $6\frac{1}{2}$ and one degree at levels $1\frac{1}{2}$ and $2\frac{1}{2}$.

Barker (personal communication) found that the number of occurrences of superadiabatic lapse rates dropped dramatically when a new three-dimensional analysis procedure was applied to the raw data before balancing. The three-dimensional analysis scheme replaced a more conventional two-dimensional system. The analysis used on the 12191175 data was a two-dimensional analysis. This suggests that

Table 6. Mean values of the initial temperature and wind fields for Forecasts 1 through 5.

Forecast Number	1	2	3	4	5
Temperature (K) Sigma level					
1½	234.1	234.1	235.0	235.0	235.0
2½	254.1	254.1	252.6	255.1	255.0
3½	262.9	262.9	261.3	263.4	263.3
4½	268.7	268.7	268.8	268.1	268.0
5½	274.1	274.1	274.3	274.3	274.3
6½	279.7	279.7	280.2	277.5	277.7
u component ($m\ s^{-1}$) Sigma level					
1½	23.1	23.1	23.1	23.1	23.1
2½	15.8	15.9	15.9	15.9	15.7
3½	12.2	12.2	12.2	12.2	12.1
4½	9.82	9.84	9.84	9.84	9.75
5½	7.65	7.67	7.67	7.67	7.54
6½	4.10	4.12	4.12	4.12	4.10
v component ($m\ s^{-1}$) Sigma level					
1½	8.20	8.21	8.21	8.21	8.44
2½	7.20	7.18	7.18	7.18	7.27
3½	7.17	7.17	7.17	7.17	7.18
4½	7.58	7.59	7.59	7.59	7.58
5½	8.20	8.19	8.19	8.19	8.19
6½	8.66	8.65	8.65	8.65	8.72

an analysis procedure with some vertical consistency constraint should be used in the initialization of the PSU model to help eliminate geopotential errors.

The same surface pressure field was used in all five experiments. Because the temperature field at the lowest level is different for the unbalanced experiments and each balanced experiment, the initial sea level pressure fields are slightly different. Fig. 21a is the sea level pressure field for Forecast 5. Fig. 21b is the balanced 500-mb temperature field and Fig. 21c is the 500-mb height field for Forecast 5. The lowest height in the trough over the Rocky Mountains is 15 m less than in Forecast 3. Fig. 21d is the initial 500-mb wind field for Forecast 5. The nondivergent wind fields for Forecasts 2, 3, and 4 are identical.

One method of comparison of the initializations involves the computation of RMS temperature difference between them. The RMS temperature differences between the initial conditions of the experiments are presented in Table 7. The values are not unusual except for the level 6½ differences between the balanced experiments and the unbalanced experiments. An examination of the temperature difference field between Forecasts 1 and 5 reveals temperature differences of up to 10°C in the ridge over the southeastern United States at level 6½. In Forecasts 4 and 5, geopotentials were calculated on sigma surfaces and the height of the level 6½ sigma surface is as much as 35 m lower than the same sigma surface for Forecasts 1 and 3. This height difference is due to the mesoscale sigma-surface balance equation used for Forecasts 4 and 5. The 35-m

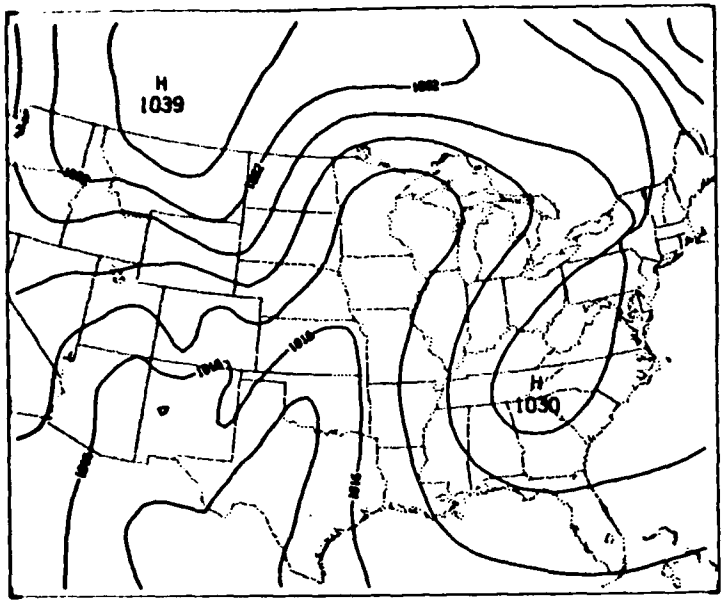

a. Sea level pressure. The contour interval is 4 mb.

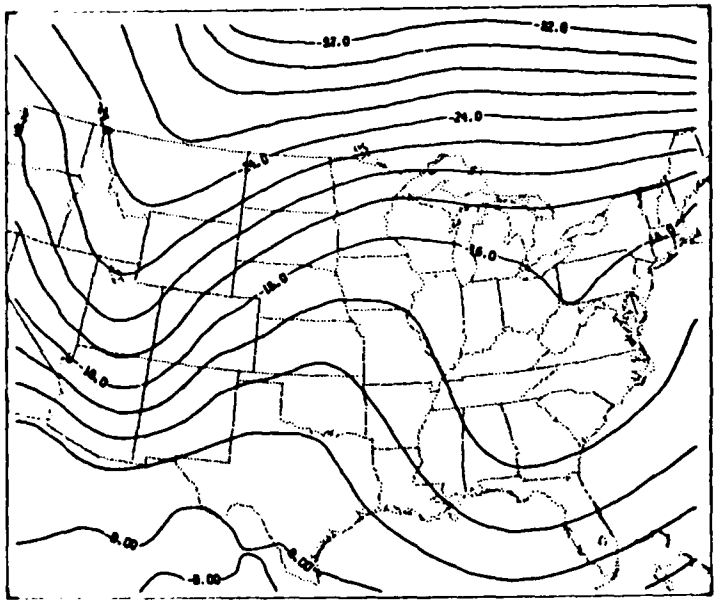

b. Balanced 500-mb temperatures. The contour interval is 2°C.

Fig. 21. Initial fields for Forecast 5.

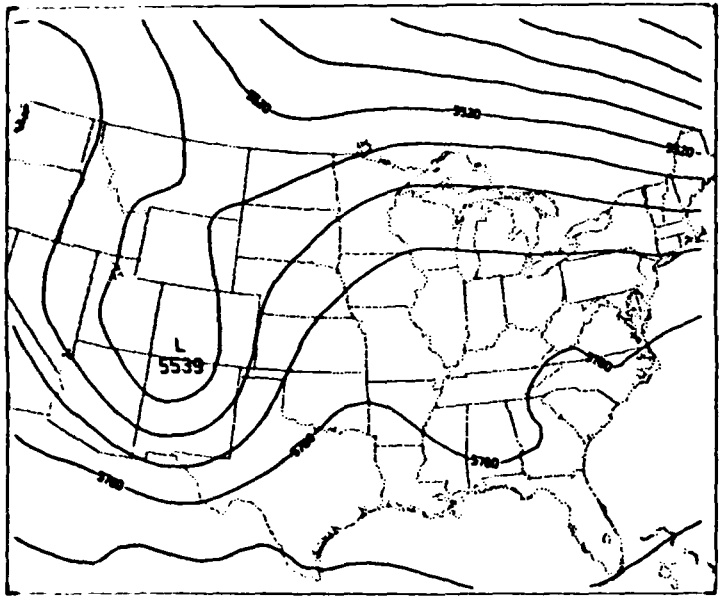

c. 500-mb height field. The contour interval is 60 m.

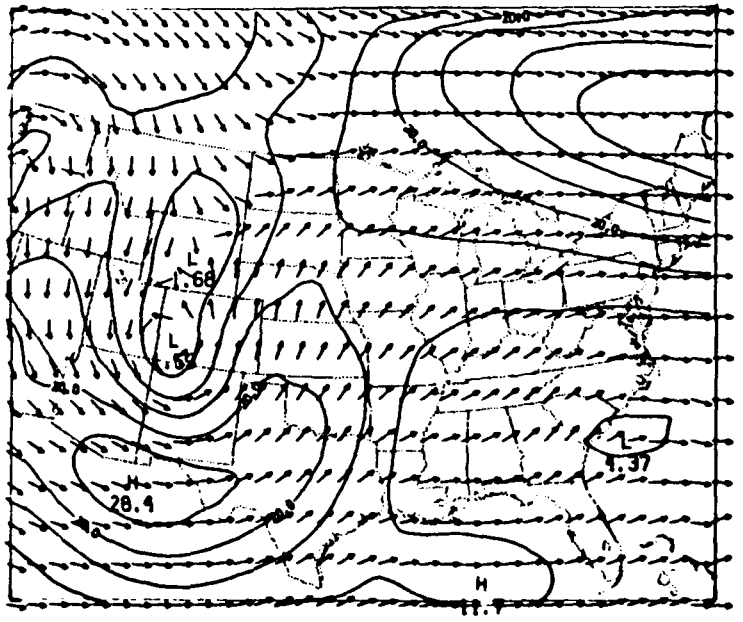

d. 500-mb wind field. The contour interval is 5 m s^{-1}.

Fig. 21. (Continued).

Table 7. RMS temperature differences (°C) between the initial conditions for some of the forecast experiments.

Forecast Experiment Numbers	1(2)-3	1(2)-5	3-4	3-5	4-5
Sigma level					
1½	2.06	1.17	2.13	2.11	0.17
2½	2.37	3.20	1.82	1.92	0.31
3½	2.53	3.15	1.04	1.22	0.30
4½	2.14	1.90	1.31	1.21	0.35
5½	1.84	2.28	1.59	1.66	0.23
6½	2.68	4.49	3.94	3.99	0.34

height difference changes the depth of the layer between sigma levels 6½ and 7 from about 470 m to about 440 m. This represents a 6 percent change in thickness and corresponds to a 6 percent reduction in the mean temperature of the lowest layer of about 20°C. This mean temperature applies at about sigma level 6 3/4. When the mean temperature is used to obtain the temperature at sigma level 6½, the resultant level 6½ temperature is up to 10°C lower than the unbalanced forecasts. We will see that this erroneous temperature difference adversely affects the RMS temperature errors at the lower levels. The geopotential errors in the vicinity of the high are an additional indication that an analysis procedure with some vertical constraint should be used in the initialization of the PSU model. That is, for a thin layer, a relatively small change in geopotential can make a relatively large change in the mean temperature of the layer.

7.2 The model forecasts

In this section the forecast results will be compared and contrasted with the exception of the precipitation predictions, which will be discussed in Section 7.3. For each forecast, noise characteristics and the 12-hour forecasts of sea level pressure, temperature, and wind will be discussed.

7.2.1 Gravity-inertia wave characteristics of the forecasts

Gravity-inertia waves in a forecast are sometimes referred to as "noise". As pointed out in Chapter 1, these waves can destroy the meteorological portion of a forecast if care is not exercised during the initialization and the forecast itself. However, gravity waves, particularly internal gravity waves, are responsible for the geostrophic adjustment process. Noise is perhaps an unfortunate choice of words as it implies that all gravity waves or vertical motions are undesirable. The undesirable vertical motions arise principally from the time-dependent boundary conditions and aliasing and are generally of smaller scale than the meteorologically significant vertical motions. The undesirable vertical motions are minimized with the enhanced horizontal diffusion scheme.

Most investigators have previously used a time series of the vertically integrated mass divergence as an indicator of noise. That is, $|\overline{\frac{\partial p_*}{\partial t}}|$ or $|\overline{\frac{\partial^2 p_*}{\partial t^2}}|$ have been used. Sundqvist (1975) plotted $|\frac{\partial p_*}{\partial t}|$ summed over the domain versus time. His curves showed an increase for the first two hours after initialization and then displayed a gradual decline.

Bleck (1977) preferred to use $|\overline{\frac{\partial^2 p_*}{\partial t^2}}|$. He stated that gravity waves appeared most clearly in the $\frac{\partial D}{\partial t}$ term of the divergence equation and, therefore, $|\overline{\frac{\partial^2 p_*}{\partial t^2}}|$ should be used to indicate external gravity-wave noise. Since $|\overline{\frac{\partial^2 p_*}{\partial t^2}}|$ is related to $\int_{p_s}^{p_t} \frac{\partial D}{\partial t}\, dp$ by the continuity equation, Bleck used $|\overline{\frac{\partial^2 p_*}{\partial t^2}}|$ as a measure of general noisiness. Bleck's plots of $|\overline{\frac{\partial^2 p_*}{\partial t^2}}|$ showed a sharp decline in general

noisiness for the first three hours followed by a gradual decline. His initial conditions were unbalanced so we should expect a high initial noise level. Bleck's model with terrain produced a value for $|\overline{\frac{\partial^2 p_*}{\partial t^2}}|$ of about 5×10^{-7} mb s^{-2} at the end of a 12-hour forecast on an 85-km mesh.

WAM reported $|\overline{\frac{\partial p_*}{\partial t}}|$ and $|\overline{\frac{\partial^2 p_*}{\partial t^2}}|$ for the PSU model applied to another data set. A time smoother has since been incorporated into the PSU model and the noise characteristics should now be somewhat different than those in WAM. Anthes (1978) used a version of the model employed here, on a 60-km grid mesh and another data set. He reported mean values of about 5×10^{-4} mb s^{-1} and 5×10^{-7} mb s^{-2} for $|\overline{\frac{\partial p_*}{\partial t}}|$ and $|\overline{\frac{\partial^2 p_*}{\partial t^2}}|$, respectively, at the end of the first 12 h of a 24-hour forecast.

Figs. 22 and 23 are the plots of $|\overline{\frac{\partial p_*}{\partial t}}|$ and $|\overline{\frac{\partial^2 p_*}{\partial t^2}}|$, respectively, versus time for Forecasts 1 through 5. In Fig. 22, the curves increase slightly for about an hour and then decrease slowly through the rest of the forecast period. Forecasts 1 and 2 have similar $|\overline{\frac{\partial p_*}{\partial t}}|$ plots and are not significantly different in this respect. Likewise, Forecasts 3, 4, and 5 have similar graphs. The forecasts started from balanced initial conditions (Forecasts 3, 4, and 5) do indicate a lower noise level as measured by $|\overline{\frac{\partial p_*}{\partial t}}|$ than the unbalanced experiments, 1 and 2. In Fig. 23, the plots decrease rapidly for three hours and then decrease more slowly for the rest of the forecast. The forecasts with unbalanced initial conditions again possess a higher noise level than the balanced experiments. Forecast 1 has a significantly higher noise level. As in Fig. 22, Forecasts 3, 4, and 5 are not substantially different. For Forecast 5, this implies that

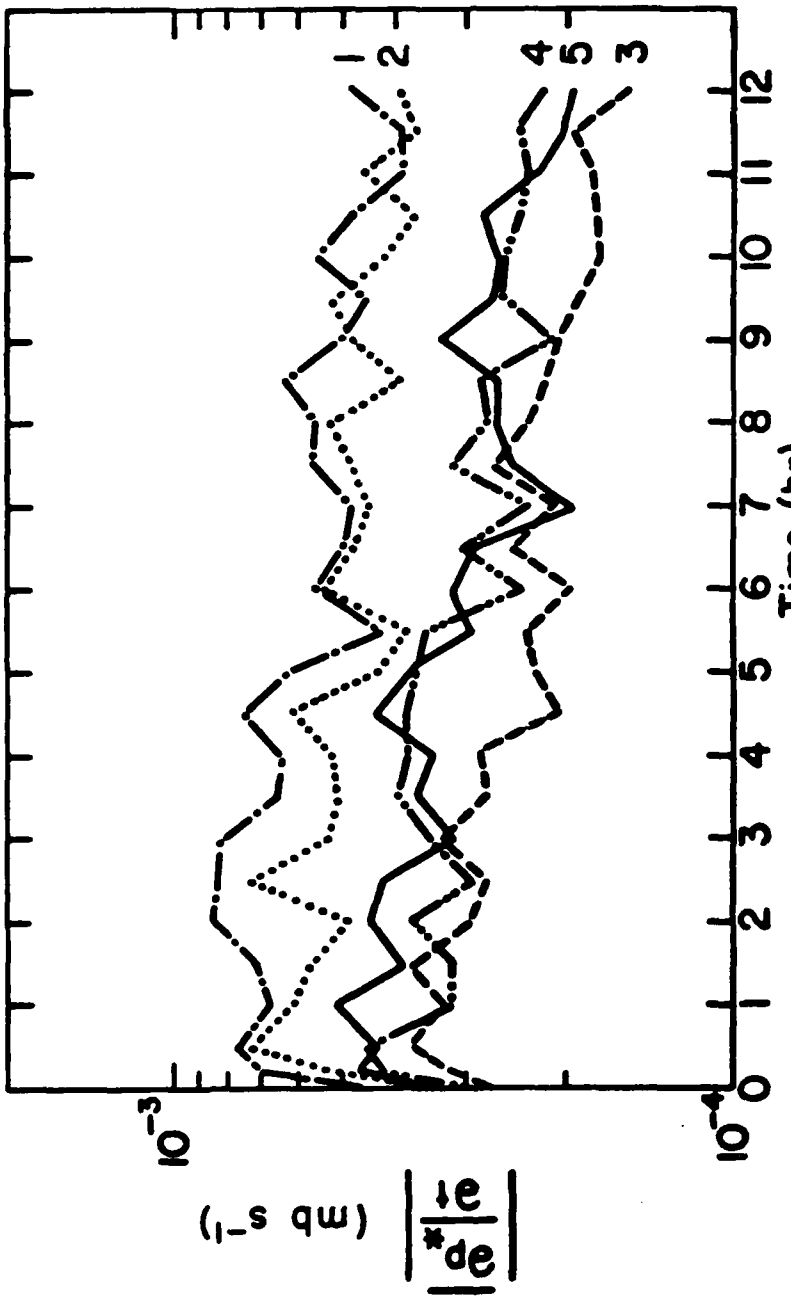

Fig. 22. External gravity-wave noise as shown by the temporal variation of $\overline{\left|\frac{\partial p_*}{\partial t}\right|}$ for Forecasts 1 through 5.

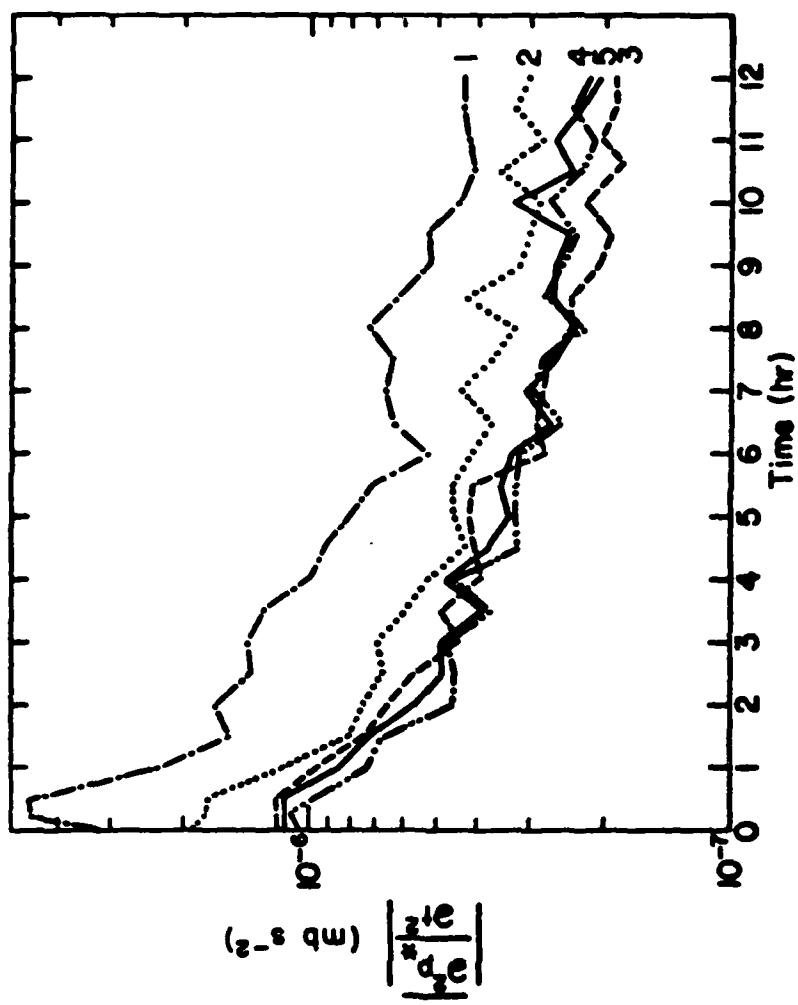

Fig. 23. External gravity-wave noise as shown by the temporal variation of $\left|\frac{\partial^2 p_*}{\partial t^2}\right|$ for Forecasts 1 through 5.

the added divergence does not generate significant additional noise in the forecast. That is, very little of the divergence is partitioned into gravity-inertia wave noise. In both Figs. 22 and 23, we detect no difference in noise level for the balanced experiments.

The results in Figs. 22 and 23 are similar to those of Bleck (1977) and Anthes (1978). Bleck's value of $|\frac{\partial^2 p_*}{\partial t^2}|$ for unbalanced initial conditions at 12 h was the same as that in Fig. 23 for Forecast 1. Anthes reported slightly higher values of $|\frac{\partial p_*}{\partial t}|$ and $|\frac{\partial^2 p_*}{\partial t^2}|$ at the end of 12 h than for the balanced experiments in Figs. 22 and 23, respectively. This was probably due to his use of a 60-km grid mesh, compared to the 120-km mesh used here. In another forecast experiment not reported on here, the parameter which controls the strength of the enhanced horizontal diffusion was increased by a factor of five. Although the precipitation amounts on the domain interior were not affected, the noise level as measured by $|\frac{\partial p_*}{\partial t}|$ was reduced by about a factor of three. Hence the temporal variation of surface pressure depends to some degree on the horizontal diffusion employed near the boundaries. This fact alone could account for the slight differences between the noise statistics reported by Bleck and Anthes and those reported here.

Sundqvist (1975) reported a significant reduction of noise level when the mass and momentum variables were balanced on sigma surfaces for a synoptic-scale model. He also reported a higher noise level for sigma-surface balancing when mountains were used as the lower boundary. The terrain field used by Sundqvist was smoothed such that $4\Delta x$ and shorter wavelengths were removed. No smoothing was applied

to the terrain field used in these experiments. Figs. 22 and 23 show no noise level reduction for balancing on sigma surfaces. Perhaps the mesoscale grid mesh, limited domain, and terrain field employed did not permit a significant noise reduction for Forecast 4, as compared to Forecast 3.

Økland (1970) studied a relatively simple two-level baroclinic model. He plotted RMS $\frac{\partial p_*}{\partial t}$ versus time for nondivergent and divergent initial conditions (divergent initial conditions consisted simply of the model prediction after 12 hours of integration; that is, the forecast was started 12 hours previously from different data). Økland's RMS $\frac{\partial p_*}{\partial t}$ curve was noisier for nondivergent initial conditions. As he pointed out, $\frac{\partial p_*}{\partial t}$ was primarily a measure of external gravity wave activity. Therefore, the forecast started from nondivergent initial conditions had more external gravity wave activity. Økland also plotted RMS omega values for a level near 500 mb. He pointed out that, because internal gravity modes have higher vertical velocities associated with them than external modes, the RMS omega curve will reflect primarily the internal gravity waves. The RMS omega curve given by Økland for the divergent initial conditions was relatively constant indicating that the internal modes were fully developed and that the model variables were approximately in balance. In Økland's nondivergent case, the RMS omega curve began at zero, reached the divergent initial condition omega curve in 3 to 4 hours, continued to rise to a maximum in 6 to 7 hours, and then decreased to a minimum at 11 to 13 hours.

Here precipitation rates are the primary interest. External gravity waves usually have a relatively small effect on precipitation. Precipitation arises mostly from the slower internal gravity modes. Therefore, the 500-mb RMS omega graphs versus time will be presented for Forecasts 3, 4, and 5. Although the previous measures of gravity-wave intensity (Figs. 22 and 23) were very similar for the three forecasts, the precipitation amounts, as shall be shown later, are significantly different. The RMS omega graphs will be related to the forecast precipitation.

Fig. 24 contains the 500-mb RMS omega plots for Forecasts 3, 4, and 5 (the plots for 1 and 2 are very similar to 3 and 4). The curve for 5 begins at a higher RMS omega value and, after 5 hours, reaches a maximum value lower than that of the nondivergent experiments. A strong similarity exists between Fig. 24 and Økland's graph of the RMS omega. Forecasts 2, 3, and 4 begin with no divergence, As the geostrophic adjustment process proceeds and those experiments begin to develop a divergent component, they actually "overshoot" the quasi-equilibrium value and develop a larger divergent component than Forecast 5 from 4 to 6 hours into the forecast. The 500-mb RMS omega curve for Forecast 5 indicates the rate of precipitation will rise slowly during the first hours of the forecast and then remain relatively constant.

Forecasts 1 and 2 possess higher noise levels than Forecasts 3, 4, and 5. Forecast 1 is particularly noisy as measured by $\overline{\left|\frac{\partial^2 p_*}{\partial t^2}\right|}$. The noise characteristics of Forecasts 3, 4, and 5 as measured by

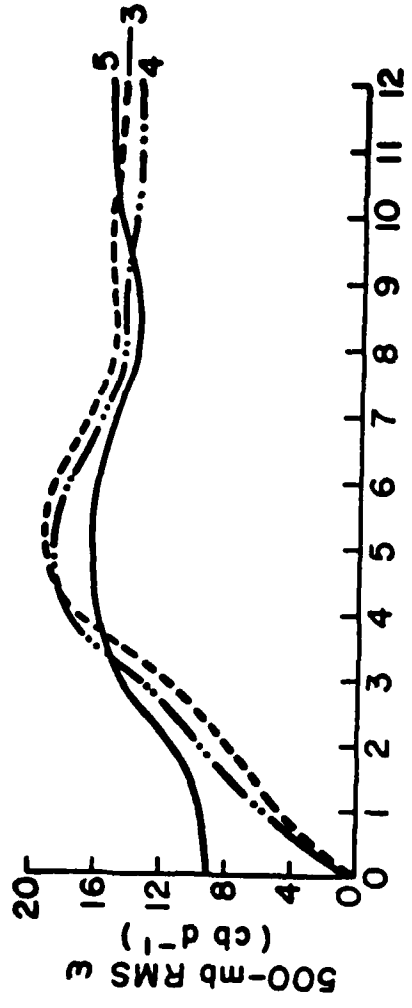

Fig. 24. Internal gravity-wave noise as measured by the temporal variation of RMS omega for Forecasts 3, 4, and 5.

graphs of $|\overline{\frac{\partial p_*}{\partial t}}|$ and $|\overline{\frac{\partial^2 p_*}{\partial t^2}}|$ are not significantly different. That is, no noise reduction resulted by balancing on sigma surfaces. However, the 500-mb RMS omega curves are significantly different between Forecast 5 and the nondivergent forecast experiments.

7.2.2 The forecasts of sea level pressure, temperature, and wind

Table 8 contains the RMS errors in the forecasts for sea level pressure and for temperature and the wind components at 400, 500, and 700 mb. No significant difference in the forecasts can be detected from these statistics although it is interesting to note that the unbalanced forecasts (Forecasts 1 and 2) had the lowest RMS temperature errors. Table 8 also contains the S1 scores for sea level pressure for each forecast. The S1 score was developed by Teweles and Wobus (1954). It is an objective measure of the forecast skill of the sea level pressure forecast that is simple to compute and has been reported often for other models. The S1 score for sea level pressure relates horizontal differences in the forecast sea level pressure to the observed differences. The S1 score is computed from

$$S1 = 100 \frac{\sum_{i=1}^{12} |\Delta P_f - \Delta P_o|}{\sum_{i=1}^{12} G_i} \qquad (7.2)$$

where ΔP_f and ΔP_o are the differences in forecast and observed sea level pressure, respectively, and G_i is the maximum of ΔP_f and ΔP_o

Table 8. RMS forecast errors and sea level pressure S1 scores for Forecasts 1 through 5.

	Forecast Number				
	1	2	3	4	5
Sea level pressure (mb)	2.76	2.79	2.60	3.31	3.01
Sea level pressure S1 score	30.2	33.5	34.3	37.5	34.6
Temperature (°C)					
400 mb	1.85	1.94	1.97	2.07	2.10
500 mb	1.77	2.05	2.22	3.06	3.22
700 mb	2.19	7.47	2.89	2.80	2.68
u component ($m\ s^{-1}$)					
400 mb	6.33	6.57	6.81	6.67	6.64
500 mb	4.30	4.22	4.54	4.49	4.43
700 mb	6.09	6.67	5.77	5.55	5.40
v component ($m\ s^{-1}$)					
400 mb	7.94	8.60	8.97	9.24	9.34
500 mb	6.49	7.26	7.45	7.18	7.35
700 mb	7.60	8.44	7.92	8.22	8.56

for a given pair of points. The differences in sea level pressure were calculated for all adjacent points in the set of nine points listed in Table 9, which gives a total of 12 combinations of points. The "observed" sea level pressure differences were calculated from the analysis of sea level pressure given in Fig. 10a. An S1 score of 20 is considered perfect for practical purposes while a score of 70 is nearly worthless.

With a slightly different version of the model used here, Anthes (1978) reported an average S1 score at 12 hours of 33.8 for 32 cases over the US and Europe. The FNWC hemispheric model achieved an S1 score at 12 hours of 37.2. These scores demonstrated considerable skill at 12 hours.

The S1 scores reported here compare well with those of Anthes and those at FNWC. It is interesting to note that the best S1 scores here are for the forecasts from unbalanced initial conditions (Forecasts 1 and 2). The S1 score of 30.2 for the forecast from observed initial conditions was significantly better than the other experiments. One conclusion from Table 8 is that divergent initialization did not improve the S1 score for sea level pressure or the RMS errors in the temperature and wind fields.

Økland (1970) obtained an analytic solution for a simple baroclinic model. From this solution, he concluded that the final adjusted state is independent of the initial divergence. Therefore, the RMS errors for the experiments in Table 8 should not be expected to be much different. Divergent initialization will, however, influence the initial precipitation rate.

Table 9. Indices of the points used in computing S1 scores. i denotes south-north direction; j denotes west-east direction. Point (1,1) is the lower left corner. Φ is north latitude; λ is west longitude.

Point	i	j	Φ	λ
1	5	10	29.4	104.2
2	5	20	29.5	91.8
3	5	30	28.1	79.7
4	15	10	40.3	106.0
5	15	20	40.8	91.3
6	15	30	39.0	76.7
7	25	10	51.5	108.8
8	25	20	52.1	90.6
9	25	30	50.2	72.5

The sea level pressure forecasts for the experiments are similar. Fig. 25a is the sea level pressure forecast for Forecast 5. The main difference between Fig. 25a and the nondivergent experiments is that the low in the nondivergent forecasts is 1009 mb. The observed central pressure of the low was 1004 mb (Fig. 10a).

The 500-mb temperature fields for the forecasts are again similar. Fig. 25d is the 500-mb temperature field for Forecast 5. None of the forecasts extended the cold air over the Rocky Mountains far enough to the south (compare with Fig. 10d). The intensity of the trough is underforecast.

Fig. 25b is the 500-mb height forecast for Forecast 5. The contour pattern is similar to the other forecasts. The lowest height over Colorado for Forecast 5 was 12 m lower than in Forecast 3. The observed height was 5472 m over the Colorado-Kansas border (see Fig. 10b).

Fig. 25c is the 500-mb wind forecast for Forecast 5. The forecasts are similar. The forecast agrees reasonably well with the observed wind field (Fig. 10c) with the exception of the wind maximum near El Paso. The forecast only slightly increased the core speed of the jet and moved the core northward a small distance. However, the core speed of the jet streak actually increased by 15.4 m s^{-1} and the core moved to a point near Dallas. As with the temperature and height fields, the wind forecast reflects the fact that the model did not forecast the rapid intensification of the trough or enough deepening of the surface low.

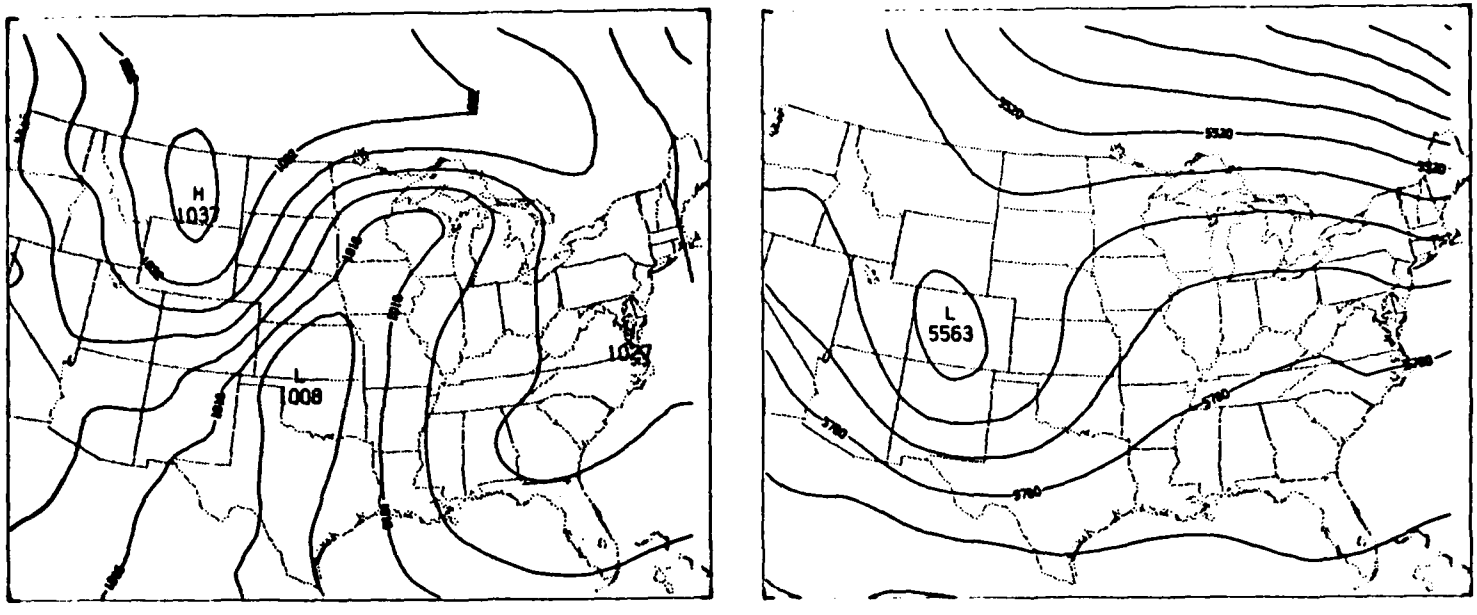

a. Sea level pressure. The contour interval is 4 mb.

b. 500-mb height field. The contour interval is 60 m.

Fig. 25. Forecast fields for Forecast 5 valid at 00201175.

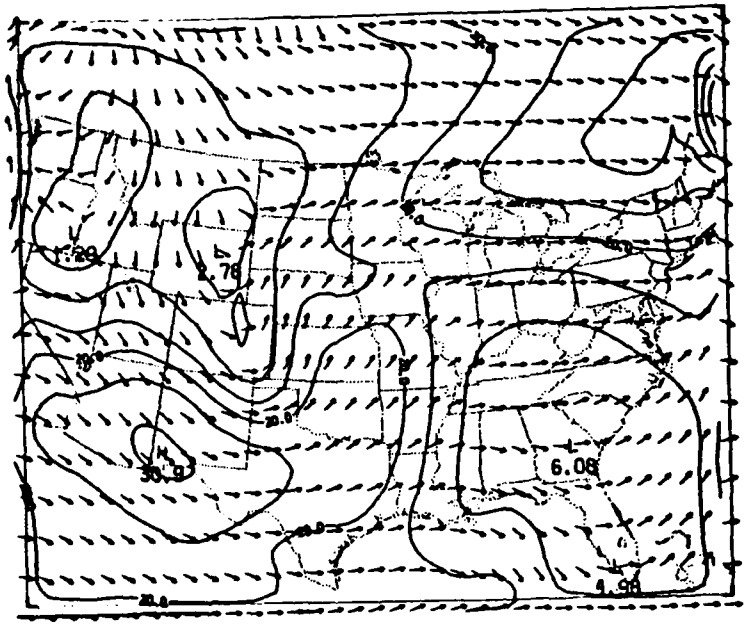

c. 500-mb winds. The contour interval is 5 m s^{-1}.

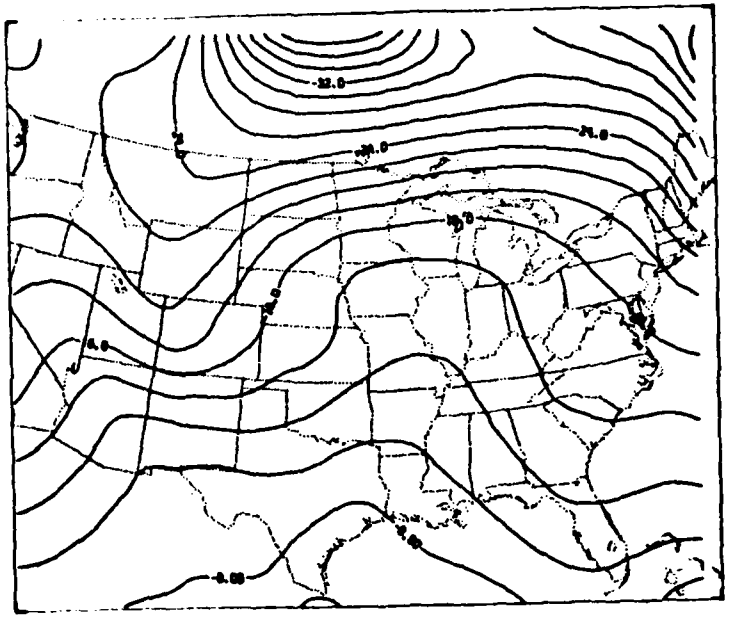

d. 500-mb temperatures. The contour interval is 2°C.

Fig. 25. (Continued).

7.3 The precipitation forecasts

In this section the precipitation forecasts will be compared. The precipitation forecasts will be viewed in several ways. First the forecasts will be "scored". Then the precipitation amounts themselves will be examined.

7.3.1 Scoring the precipitation forecasts

Anthes (unpublished) developed an objective procedure for the "scoring" of precipitation fields. If the forecast precipitation field is one grid increment displaced from the observed precipitation field, then the forecast still contains useful information. The objective procedure that will be used, scores a precipitation forecast in a quantitative way to determine if a shift in the forecast field with respect to the observed field improves the forecast when compared with the observations. The complete objective procedure is presented in Appendix 3. Therefore, it is discussed only briefly here. A correlation coefficient is calculated for each shift in position of the forecast field with respect to the observed field. An example matrix of correlation coefficients $c_{\ell,k}$ for a shift in each direction of two grid increments is given in Appendix 3. For example, $c_{0,0}$ is the correlation coefficient for no shift and $c_{1,0}$ is the correlation coefficient for a shift one grid increment to the right. Good forecasts would have a large maximum $c_{\ell,k}$ (1.0 is perfect) and low values for ℓ and k for the maximum correlation coefficient (0 and 0 are perfect).

Figs. 26a, 26b, and 26c contain the correlation coefficient matrices for the first three hours of the forecast for Forecasts 3, 4, and 5, respectively (Forecasts 1 and 2 are similar to Forecast 3). Note that for the nondivergent forecasts (3 and 4), the highest correlation coefficient is displaced one grid increment from the center. For Forecast 5, the highest correlation coefficient occurs with no spatial offset. Also the maximum correlation coefficient for Forecast 5 ($c_{0,0} = 0.75$) is higher than the nondivergent forecasts ($c_{0,1} = 0.55$ for Forecast 3 and $c_{0,1} = 0.66$ for Forecast 4). That is, the forecast experiment started with a divergent initialization produced the best scores.

Figs. 27a, 27b, and 27c contain the correlation coefficient matrices for the entire 12-hour period for Forecasts 3, 4, and 5. The maximum correlation coefficients for the three forecasts were 0.77, 0.75, and 0.76 for Forecasts 3, 4, and 5, respectively. For the entire forecast period, all three forecast experiments had the highest correlation coefficient with no spatial offset of the forecast and observed precipitation fields. Therefore, the objective procedure detects no differences in the 12-hour precipitation forecasts when divergence is included in the initial conditions.

7.3.2 The total precipitation amounts and the precipitation rates

Fig. 28 contains the total precipitation amounts for each hour through the forecast period for each experiment as well as the total depth of observed precipitation. The amounts were summed for the

$$C = \begin{vmatrix} 0.32 & 0.32 & 0.40 & 0.48 & 0.43 \\ 0.34 & 0.35 & 0.47 & 0.55 & 0.50 \\ 0.29 & 0.31 & 0.47 & 0.55 & 0.48 \\ 0.24 & 0.24 & 0.37 & 0.47 & 0.44 \\ 0.18 & 0.18 & 0.33 & 0.43 & 0.39 \end{vmatrix}$$

a. Forecast 3.

$$C = \begin{vmatrix} 0.32 & 0.40 & 0.51 & 0.57 & 0.51 \\ 0.37 & 0.45 & 0.61 & 0.66 & 0.57 \\ 0.36 & 0.42 & 0.61 & 0.66 & 0.55 \\ 0.31 & 0.35 & 0.53 & 0.61 & 0.50 \\ 0.24 & 0.23 & 0.45 & 0.55 & 0.42 \end{vmatrix}$$

b. Forecast 4.

$$C = \begin{vmatrix} 0.30 & 0.43 & 0.59 & 0.63 & 0.52 \\ 0.35 & 0.51 & 0.72 & 0.74 & 0.57 \\ 0.36 & 0.51 & 0.75 & 0.74 & 0.58 \\ 0.32 & 0.46 & 0.66 & 0.70 & 0.54 \\ 0.24 & 0.36 & 0.56 & 0.61 & 0.43 \end{vmatrix}$$

c. Forecast 5.

Fig. 26. Correlation coefficient matrices from the objective precipitation scoring procedure for the first three hours of the forecast.

$$C = \begin{vmatrix} 0.63 & 0.64 & 0.64 & 0.55 & 0.43 \\ 0.67 & 0.69 & 0.71 & 0.62 & 0.49 \\ 0.68 & 0.72 & 0.77 & 0.69 & 0.53 \\ 0.70 & 0.76 & 0.77 & 0.70 & 0.53 \\ 0.62 & 0.67 & 0.68 & 0.61 & 0.46 \end{vmatrix}$$

a. Forecast 3.

$$C = \begin{vmatrix} 0.66 & 0.67 & 0.66 & 0.55 & 0.42 \\ 0.69 & 0.70 & 0.71 & 0.61 & 0.48 \\ 0.69 & 0.72 & 0.75 & 0.67 & 0.52 \\ 0.70 & 0.75 & 0.75 & 0.67 & 0.50 \\ 0.61 & 0.66 & 0.66 & 0.59 & 0.43 \end{vmatrix}$$

b. Forecast 4.

$$C = \begin{vmatrix} 0.67 & 0.67 & 0.65 & 0.54 & 0.41 \\ 0.70 & 0.71 & 0.71 & 0.60 & 0.47 \\ 0.70 & 0.73 & 0.76 & 0.66 & 0.51 \\ 0.72 & 0.76 & 0.74 & 0.66 & 0.49 \\ 0.63 & 0.67 & 0.66 & 0.59 & 0.42 \end{vmatrix}$$

c. Forecast 5.

Fig. 27. Correlation coefficient matrices from the objective precipitation scoring procedure for the entire 12-hour forecast period.

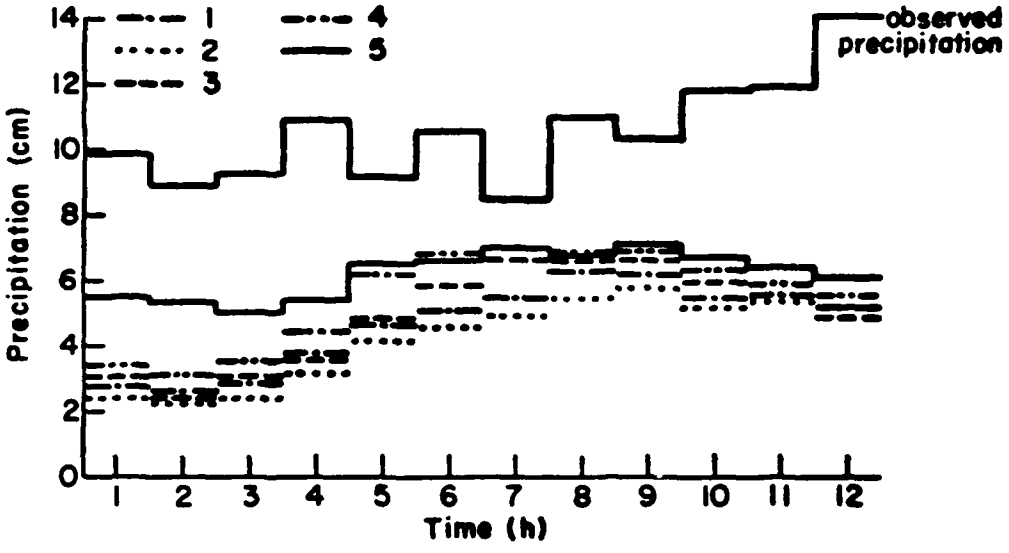

Fig. 28. Total precipitation depth (cm) for the entire domain for Forecasts 1 through 5.

entire domain in order to compare the total depth of precipitation for each forecast with the observed precipitation. Multiplying each depth by the area of a grid square would yield precipitation volume. The total amount of precipitation forecast by the model is a useful statistic because the forecasts over the whole domain can be compared. Similarly, Figs. 29a and 29b present the total precipitation depth forecast by the convective and nonconvective precipitation parameterizations, respectively.

For the nondivergent experiments, a slight decrease in the total precipitation occurs from hour 1 to hour 2 followed by an increase each hour to the maximum amounts in hours 7, 8, and 9. Then the amounts generally decrease for each hour through the end of the forecast. The behavior of the convective and nonconvective precipitation follows the same general pattern. However, Forecasts 1 and 2 have consistently smaller nonconvective precipitation amounts after hour 3. In contrast, the total precipitation for the forecast from a divergent initialization (Forecast 5) is more uniform throughout the forecast period. The precipitation from Forecast 5 does reach maximum values in hours 7, 8, and 9, and these maximum values are approximately equal to Forecasts 3 and 4 for those hours. However, the maximum values are only about 20 percent greater than the first and last forecast hours. The observed precipitation is about uniform throughout the forecast period although there is an increase in the last three hours. Recall the 500-mb RMS omega curves of Fig. 24. The relatively constant curve for Forecast 5 is reflected in the relatively constant

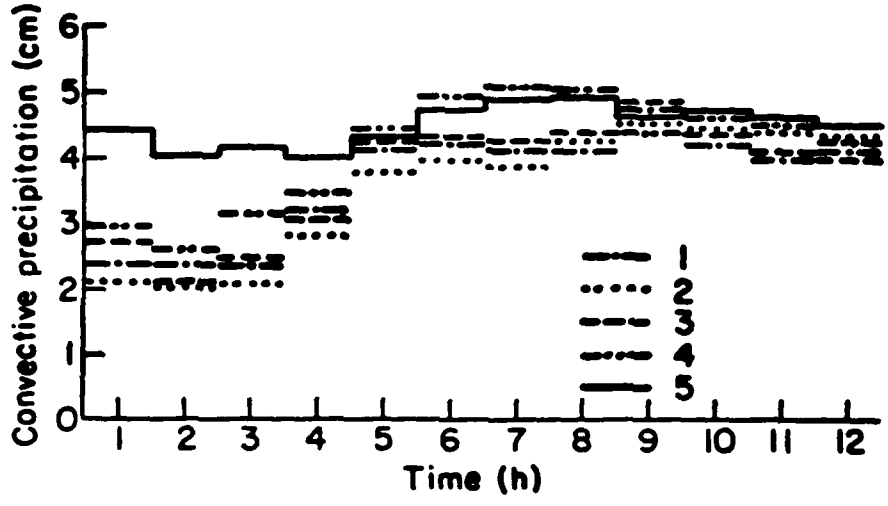

a. Convective precipitation.

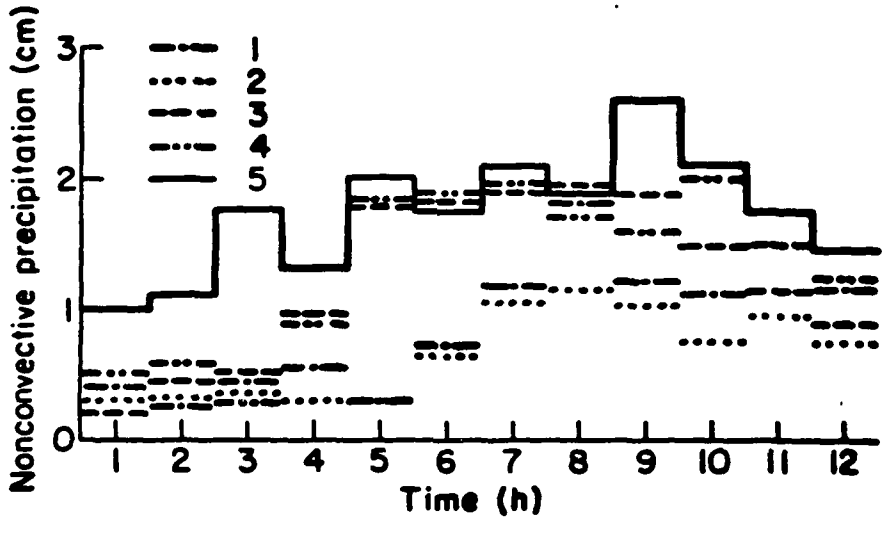

b. Nonconvective precipitation.

Fig. 29. Total precipitation depth (cm) for the entire domain for the convective and nonconvective precipitation parameterizations for Forecasts 1 through 5.

precipitation amounts for each hour. The greater variability of the curves for Forecasts 3 and 4 is reflected in the greater variability in the precipitation amounts by hour for those experiments. Note that the maxima in the RMS omega curves for Forecasts 3 and 4 occur at hour 5 while the maxima in their precipitation amounts occur later in the forecast period. Therefore, the 500-mb RMS omega curves are not perfectly correlated with the precipitation amounts. Instead, it is suggested that a greater variability in the RMS omega curves implies a greater variability in the rainfall amounts, but that the maxima in the two do not necessarily coincide.

The 12-hour precipitation depths summed for every grid point over the domain for the experiments are 55.2 cm, 50.5 cm, 58.8 cm, 65.6 cm, and 72.9 cm for Forecasts 1 through 5, respectively. Note that, for the entire period, Forecast 5 produced 32, 44, 24, and 11 percent more precipitation than Forecasts 1, 2, 3, and 4, respectively. However, the 12-hour precipitation total for Forecast 5 is only 58.1 percent of the observed precipitation total. The 12-hour observed precipitation is really an approximation because precipitation is sampled only at a few points. Also, there is evidence of convective activity in Fig. 11b (small-scale peaks in precipitation amounts). A model with a grid increment of 120 km cannot be expected to forecast small (e.g., 30 km by 30 km) areas of convective activity. For this reason, the model should not be expected to forecast 100 percent of the observed point values of precipitation, when these values are not representative of grid-square averages. In spite of this, the

precipitation forecast for the divergent initialization is a significant improvement over the other forecasts.

For all the experiments, the total precipitation for hours 7 through 12 is about the same. Therefore, the difference in the 12-hour forecast amounts is due almost entirely to the first 6 hours of the forecasts. Additionally, most of the difference in the first 6 hours occurs in the first 3 of those 6 hours. In the first 3 hours, Forecast 5 produced 89, 118, 83, and 56 percent more precipitation than Forecasts 1, 2, 3, and 4, respectively. This precipitation increase is directly attributable to the divergent initialization.

When nondivergent initial conditions are used, the model did produce about the same amount of precipitation in the last half of the forecast as it did with divergent initial conditions. The nondivergent forecasts did not "overshoot". That is, they did not precipitate more than the divergent forecast later in the 12-hour period. If the nondivergent forecasts did overshoot, they would begin to catch up to the total 12-hour amount produced by the divergent initialization. Therefore, the precipitation lost at the beginning of a forecast started from a nondivergent initialization is not recovered.

For Forecast 5, the initial slight increase in the 500-mb RMS omega curve in Fig. 24 and the more realistic precipitation amounts in the first 4 hours of the forecast are the best indicators that the model did indeed remember the initial divergence.

The usefulness of divergent initialization is not just the additional precipitation in the first 6 hours of the forecast but also the relatively constant precipitation rate. Although precipitation does not necessarily occur at an almost constant rate, it did not occur in the pattern of amounts shown by the nondivergent forecasts either. That is, the amounts in Fig. 28 for the nondivergent experiments reflect the anomolous divergence associated with the geostrophic adjustment process in the model. The divergent component gradually builds up, overshoots the balanced state, and then gradually oscillates about the balanced state. This is the principle cause of the oscillation in the precipitation amounts for the nondivergent forecasts. However, in the divergent initialization experiment, the model was closer to an initial balance between the nondivergent and divergent components. Hence there is less tendency for the model to reflect temporal maxima and minima in the mean precipitation amounts that are as extreme as for the nondivergent forecasts.

The precipitation fields for Forecasts 3, 4, and 5 will now be compared with each other and with the observed precipitation. Figs. 30b, 30c, and 30d are the forecast precipitation amounts for the first three hours for Forecasts 3, 4, and 5, respectively. Figs. 31b, 31c, and 31d are the forecast precipitation amounts for the 12-hour forecasts for Forecasts 3, 4, and 5, respectively. Figs. 30a and 31a are the observed precipitation amounts for the first three hours and the entire 12-hour period, respectively. There is some evidence of noise in all the forecast precipitation figures. For example,

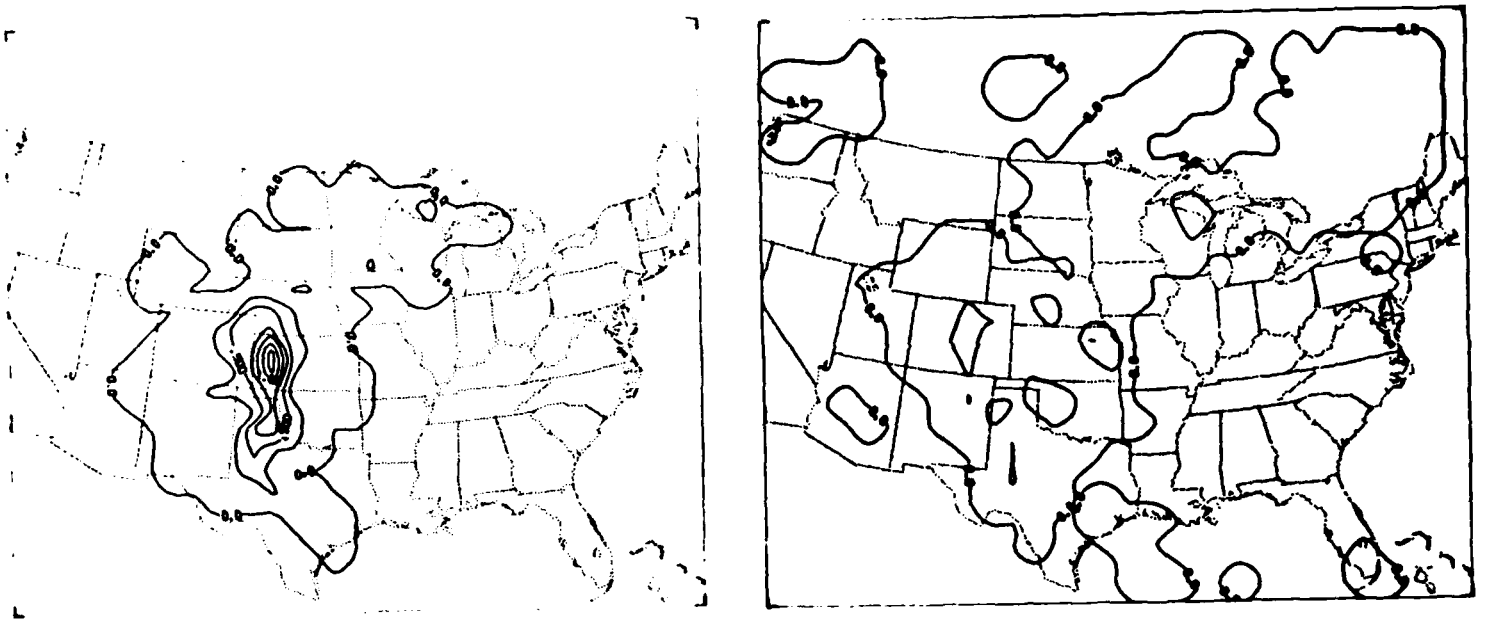

a. Observed precipitation. The maximum amount over western Kansas is about 1.5 cm. The contour interval is 0.25 cm.

b. Forecast precipitation for Forecast 3. The maximum amount over western Kansas is less than 0.13 cm. The contour interval is 0.125 cm.

Fig. 30. Observed precipitation for the first three hours of the forecast period (12191175 to 15191175) and the forecast precipitation for the same period for Forecasts 3, 4, and 5.

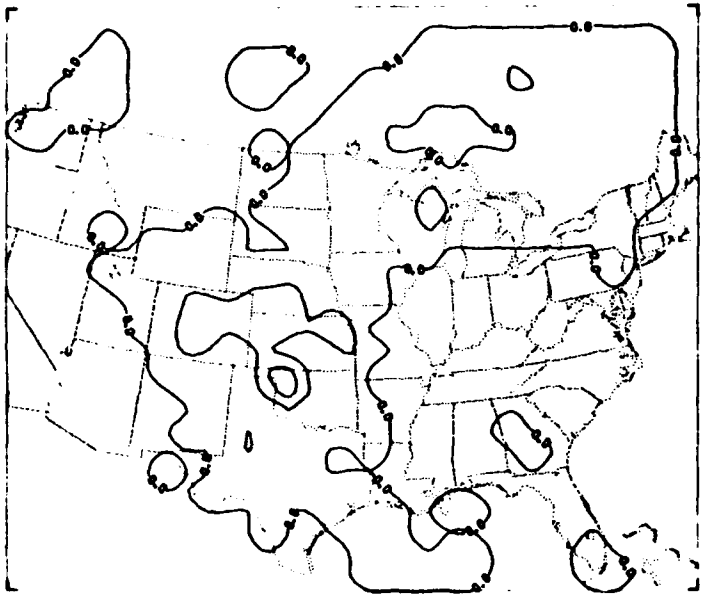

c. Forecast precipitation for Forecast 4. The maximum amount over western Kansas is about 0.2 cm. The contour interval is 0.125 cm.

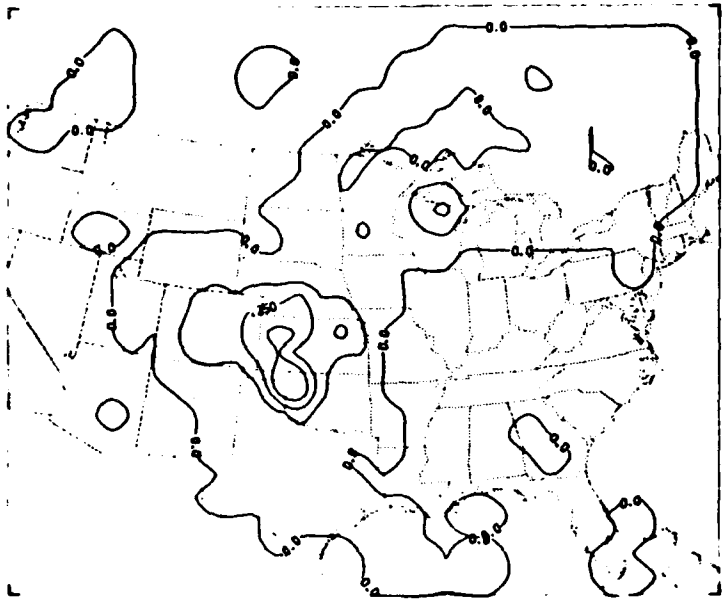

d. Forecast precipitation for Forecast 5. The maximum amount over western Kansas is about 0.45 cm. The contour interval is 0.125 cm.

Fig. 30. (Continued).

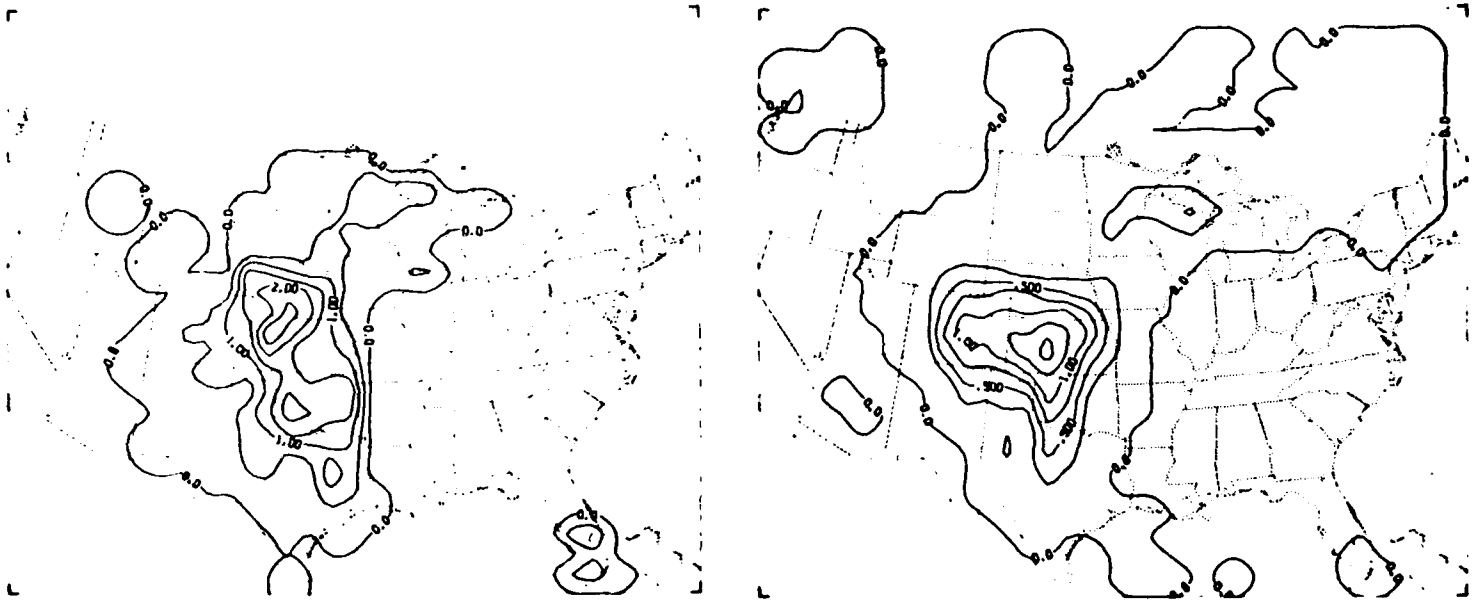

a. Observed precipitation. The maximum amount over western Kansas is about 2.6 cm. The contour interval is 0.5 cm.

b. Forecast precipitation for Forecast 3. The maximum amount over western Kansas is about 1.5 cm. The contour interval is 0.25 cm.

Fig. 31. Observed precipitation for the entire 12-hour forecast period (12191175 to 00201175) and the forecast precipitation for the same period for Forecasts 3, 4, and 5.

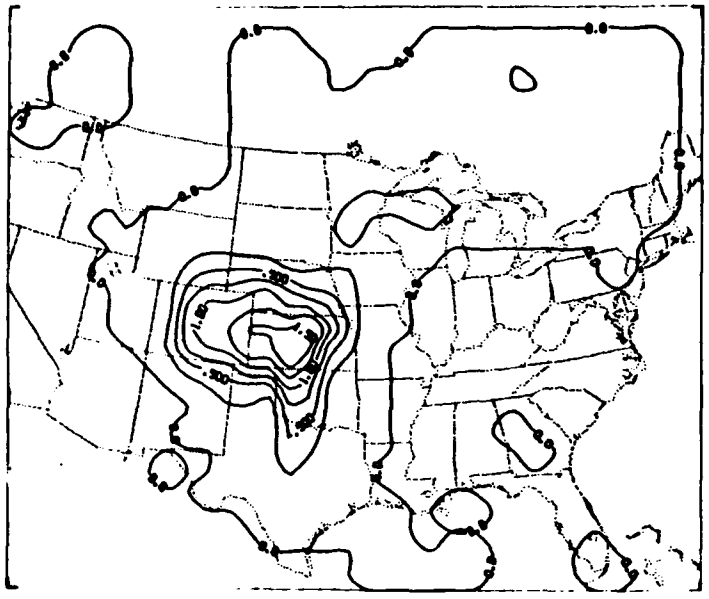

c. Forecast precipitation for Forecast 4. The maximum amount over western Kansas is about 1.6 cm. The contour interval is 0.25 cm.

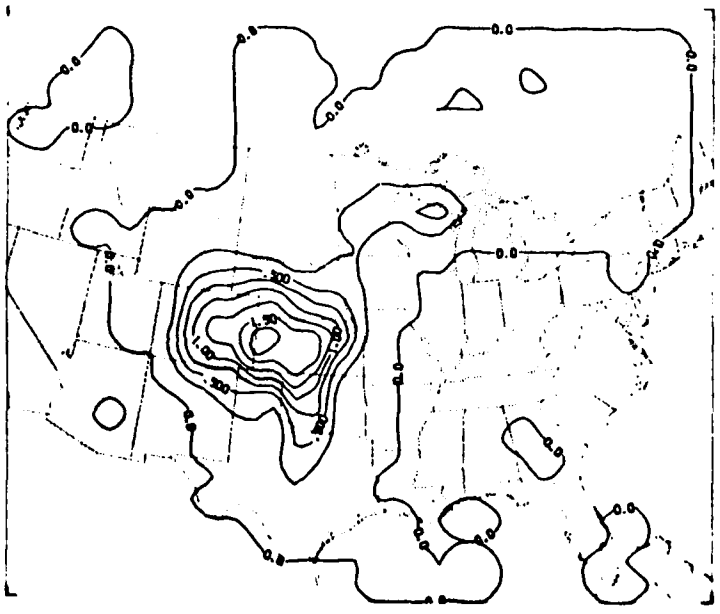

d. Forecast precipitation for Forecast 5. The maximum amount over western Kansas is about 1.8 cm. The contour interval is 0.25 cm.

Fig. 31. (Continued).

the small area of precipitation in the northwest corner of the domain is due to boundary-generated noise and is not meteorological.

In comparing Figs. 30b, 30c, and 30d, note that the 0.25-cm contour in Fig. 30d covers a larger area than in Figs. 30b and 30c. It is apparent that more precipitation occurred in the first three hours of the forecast with divergent initial conditions. For the 12-hour forecast precipitation amounts, the 0.25-cm contour in Figs. 31b, 31c, and 31d covers about the same area. Again, the highest amounts appear inside the 0.25-cm contour of Fig. 31d.

Since the model did produce an improved precipitation forecast with the divergent initialization used in Forecast 5, especially in the first few hours, the initial divergence was "remembered" or retained by the model. That is, the initial divergence was not dissipated by internal gravity waves before it could be supported by precipitation and the associated release of latent heat. Since the precipitation occurred in the correct locations, the divergent wind fields and consequently the diagnosed omega field were sufficiently accurate to be useful in divergent initialization.

In order to show that the model did retain the initial divergence, the initial precipitation rates at several locations will be examined. These locations are plotted in Fig. 32. The points were selected because most of those locations had significant precipitation at the initial time. For each location in Fig. 32, Fig. 33 contains the forecast precipitation for each 0.1-hour interval for the first 1.6 hours of the forecast period. Fig. 33 also contains the "observed"

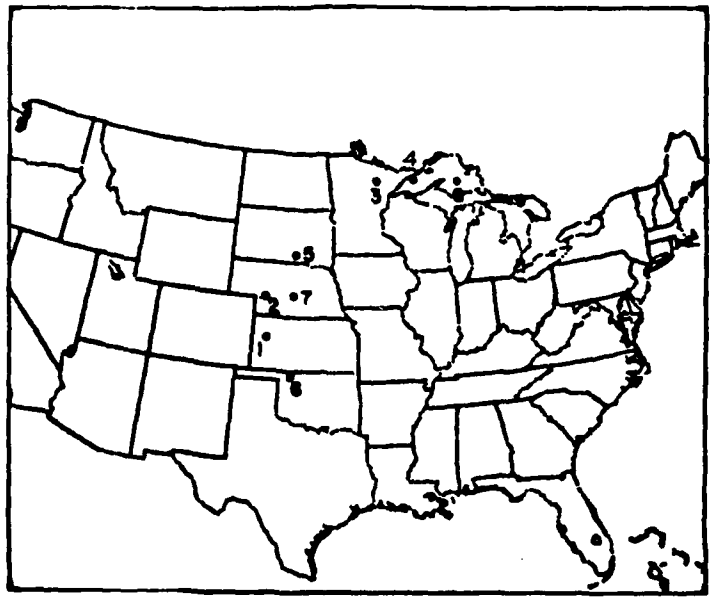

Fig. 32. Locations at which the initial precipitation was examined.

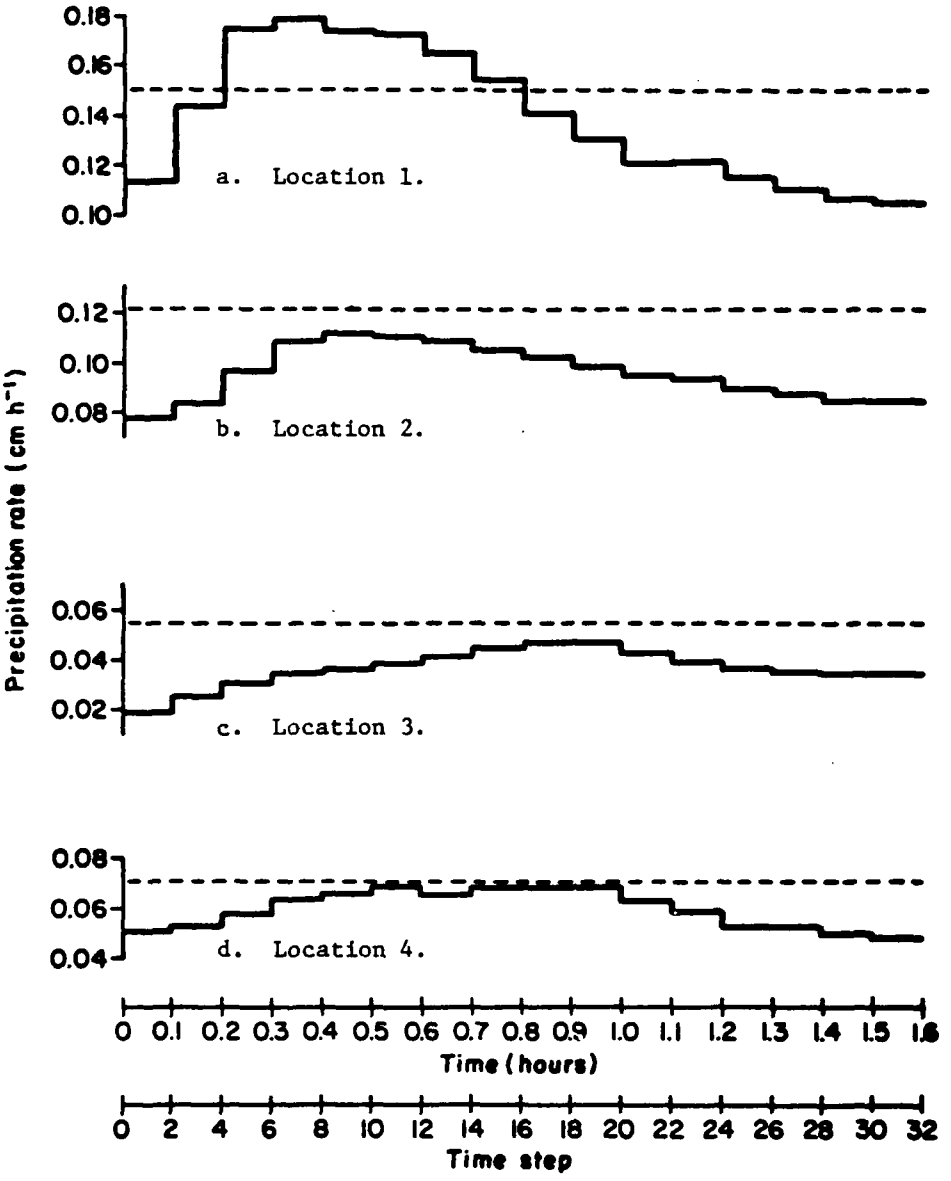

Fig. 33. Initial precipitation rates (cm h^{-1}) at the locations in Fig. 32 for the first 1.6 hours of the forecast from Forecast 5. The dashed line represents the "observed" initial rain rate as depicted in Fig. 13. The solid line is the precipitation amount for each two time-step period (0.1 hour).

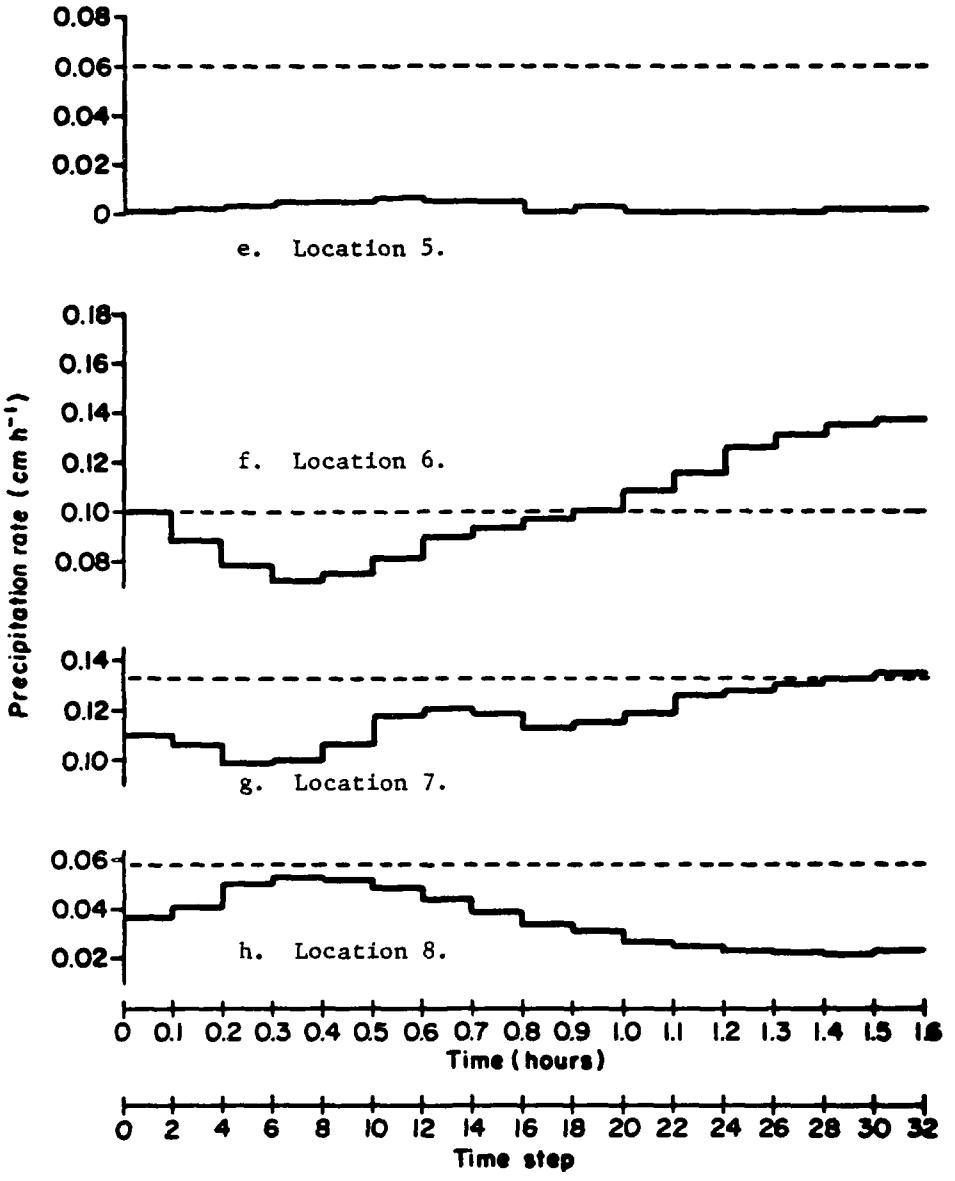

Fig. 33. (Continued).

initial precipitation rate. The observed rate was taken from the same four-hour average precipitation rate that was used for the diabatic term of the omega equation (Fig. 13). The purpose of Fig. 33 is to show how well the forecast initial precipitation rate for Forecast 5 matches the observed initial precipitation rate. At most of the points, the forecast initial precipitation rate is near the observed rate. Also, the forecast rate is relatively constant indicating that the initial divergence did not dissipate or migrate away from the initial precipitation area. The worst result was at location 5. It is near an area of relatively light observed initial precipitation. Also, the initial moisture analysis indicates that location 5 is on the edge of the saturated area. Therefore, the initial divergence probably did not initiate precipitation fast enough for the divergence to be maintained. Recall that saturated initial conditions are *essential for divergent* initialization in areas of initial observed precipitation because immediate latent heat release is required to maintain the upward motion associated with strong convergence. Otherwise, the initial divergence would be dissipated by internal gravity waves.

Fig. 33 demonstrates that the initial divergence is retained reasonably well. However, it is possible that the initial divergence produced precipitation at an unexpected location. For example, the precipitation that was expected at location 5 could have occurred to the south or southwest of location 5. This possibility will be examined in Fig. 34. Figs. 34b through 34o contain the initial

AD-A105 501 AIR FORCE INST OF TECH WRIGHT-PATTERSON AFB OH F/G 7/2
THE INITIALIZATION OF THE DIVERGENT COMPONENT OF THE HORIZONTAL--ETC(U)
MAY 79 T C TARBELL
UNCLASSIFIED AFIT-CI-79-294D-S NL

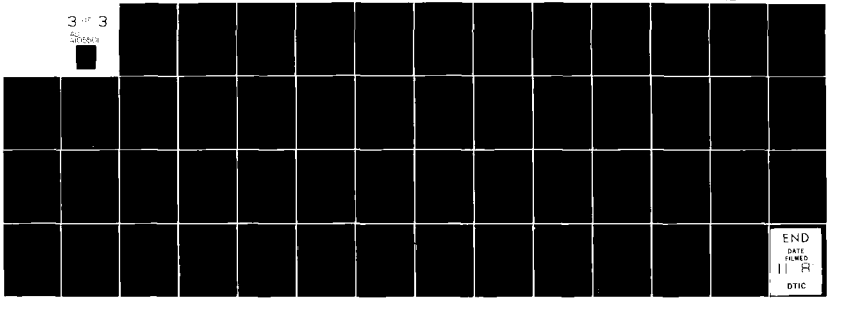

Fig. 34. Forecast rain rates (cm h^{-1}) for each 0.1-hour period for the first 1.4 hours of Forecast 5, the forecast with divergent initial conditions, for that portion of the domain with the highest initial precipitation rates. For comparison, the observed rain rate (cm h^{-1}) derived from Fig. 13 and the locations from Fig. 32 are also given. The contour interval is 0.05 cm h^{-1}.

a. Observed 0.1-hour rain rate.
b. 0.0-0.1 hour.
c. 0.1-0.2 hour.
d. 0.2-0.3 hour.
e. 0.3-0.4 hour.
f. 0.4-0.5 hour.
g. 0.5-0.6 hour.
h. 0.6-0.7 hour.
i. 0.7-0.8 hour.
j. 0.8-0.9 hour.
k. 0.9-1.0 hour.
l. 1.0-1.1 hours.
m. 1.1-1.2 hours.
n. 1.2-1.3 hours.
o. 1.3-1.4 hours.

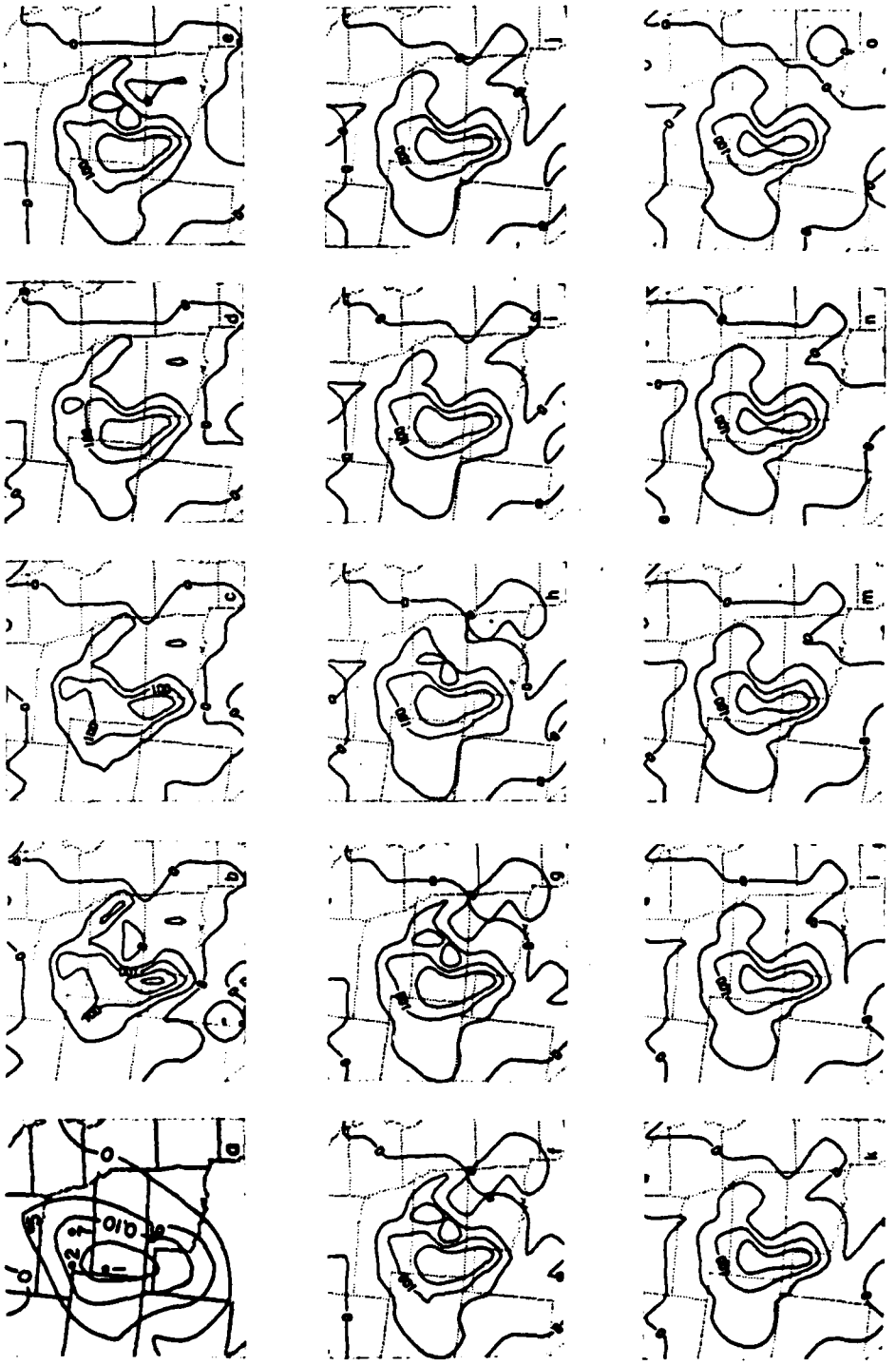

forecast rain rates (0.05 cm h^{-1} contour interval) for each 0.1-hour period for the first 1.4 hours of the divergent initialization experiment for that portion of the domain which had the highest observed initial precipitation rate. For comparison purposes, Fig. 34a contains the observed initial precipitation rate (0.05 cm h^{-1} contour interval) as well as the five locations from Fig. 32 that fall within the area of heaviest precipitation. First, note that the zero contour is forecast well in the northwest, east, southeast, and southwest portions of the region portrayed. Second, the highest initial precipitation rates occur on too small a scale to be retained. Sufficient vertical motion to sustain them was probably not diagnosed by the omega equation on that scale either. The largest forecast rain amounts that did occur are in Fig. 34b. These could be due in part to the relatively high initial noise level since no attempt was made to obtain a divergent wind component that was exactly compatible with the nondivergent wind component. Third, although the forecast 0.1 cm h^{-1} contour covers a smaller area than the observed one, note that it consistently remains about the same size. It is almost exactly the same size in Figs. 34d through 34h and again in Figs. 34i through 34o. There are no rapid changes in the forecast pattern that would be associated with the dissipation of the initial divergence. Fig. 34 shows that the divergent initialization experiment did not forecast the total observed amount because the highest observed precipitation rates were not duplicated and because the area of heaviest forecast precipitation was not as large as the corresponding observed area.

Figs. 33 and 34 demonstrate conclusively that the initial precipitation rates were steady and duplicated the observed initial rates reasonably well. The divergent initialization was useful in improving the initial precipitation rates. The following are possible reasons why the divergent initialization experiment did not duplicate the observed initial precipitation rate exactly:

(1) The forecast model's cumulus parameterization, which was responsible for most of the initial precipitation, might not be producing precipitation at the correct rate for the given profiles of specific humidity and the dynamic variables.

(2) The moisture analysis may not have been saturated over a large enough area to support the necessary latent heating rate implied by the initial vertical motion field.

(3) The initial divergent wind component was not completely compatible with the nondivergent component.

(4) Some of the initial divergence may have dissipated before latent heating had time to support it.

(5) The heaviest observed precipitation rate occurred on a scale too small for the omega equation and/or the forecast model to represent on a 120-km grid mesh.

For this case divergent initialization significantly improved the short-range forecasting of precipitation with a mesoscale numerical

weather prediction model started from a static initialization. Greater improvements would be likely for cases with higher precipitation rates at the initial time.

7.4 Chapter summary

In this chapter five 12-hour forecasts were compared in which the forecast model was initialized in different ways. The five initializations were presented in Fig. 20.

The external gravity-wave noise characteristics of the forecasts as measured by $|\frac{\partial p_*}{\partial t}|$ and $|\frac{\partial^2 p_*}{\partial t^2}|$ were not greatly different although the forecasts from unbalanced initial conditions contained more noise. These measures of noise levels were comparable to those values reported by Anthes (1978) and Bleck (1977). Sundqvist (1975) reported that a lower noise level resulted from an initialization on sigma surfaces. We did not obtain a reduced noise level in the experiments balanced on sigma surfaces. This was probably due to the smaller grid increment, unsmoothed terrain, and limited domain used here. The 500-mb RMS omega curve for the divergent initialization (Forecast 5) was significantly different from others as it exhibited less variability during the 12-hour forecast. The internal gravity-wave activity in the forecast from the divergent initialization was therefore more uniform and the model was initially closer to a "balanced" state. The 500-mb RMS omega graphs exhibited similar behavior to those of Økland (1970).

The forecasts of sea level pressure, temperature, and wind fields were not significantly different in terms of RMS error. That is, the divergent initialization did not improve the forecast of these variables. The S1 forecasts for sea level pressure were best for the unbalanced experiments, especially for the forecast initialized directly with observed data.

The precipitation forecasts were compared in several ways. The forecasts for Forecasts 3, 4, and 5 were scored with the objective procedure presented in Appendix 3. This procedure is a type of pattern recognition evaluation and can determine if the forecast precipitation is in the correct location when compared with the observations. When measured with this technique, the forecast with divergent initial conditions did much better in the first three hours. However, over the entire forecast period, all three forecasts scored equally well.

The total precipitation amounts over the entire domain were compared with the observed amounts. It was found that the amounts for the nondivergent experiments gradually rose until about hour 9 and then gradually decreased. Although a maximum occurred in the divergent forecast at about hour 9, the precipitation amounts were relatively uniform for the entire forecast period. The changes in forecast amounts for the nondivergent experiments were related to the adjustment occurring in the model. In the forecast with divergent initial conditions, the model was much closer to a balanced state at the beginning of the forecast.

Forecast 5 produced significantly more precipitation in the 12-hour forecast period. Much of the improvement in the forecast precipitation amounts came in the first three hours. The nondivergent forecasts started with a precipitation deficit and did not make up that deficit later in the forecast. The best short-term precipitation forecast was obtained with the divergent initialization.

The initial forecast precipitation rates were studied at selected points and for that portion of the domain containing the highest precipitation rates. The initial precipitation rates were nearly uniform and the area enclosed by specific contours was relatively constant. Although the highest observed initial precipitation rates were underforecast, both in terms of maximum rate and the area covered by a given contour, the forecast model did indeed retain a substantial portion of the initial divergence.

Divergent initialization on the mesoscale was successful in improving the precipitation forecast for this data set. It improved the forecast in two ways: (1) the initial precipitation rate was almost uniform and allowed significantly higher precipitation in the first three hours, and (2) the total precipitation amounts through the entire forecast period were more realistic.

8.0 SUMMARY AND CONCLUSIONS

Numerical weather prediction in general, the initialization of primitive equation models, and previous attempts at the initialization of the divergent component of the horizontal wind were reviewed in this thesis. Most prior divergent initializations were on the synoptic scale and, on that scale, had little effect on the initial precipitation rate.

Scale analyses were conducted to establish the form of the vertical velocity and divergence equations appropriate on the mesoscale. The effect of the assumptions used in neglecting the time dependent terms in the vertical velocity and divergence equations was analyzed. The scale dependence of divergent initialization on the synoptic and mesoscales was examined. For the vertical velocity equation on the synoptic scale, the diabatic term is of the same order as differential vorticity advection or the Laplacian of temperature advection. Also, the Coriolis term was important. On the mesoscale, the diabatic term dominated in precipitation areas and must be included. The Coriolis term was not nearly as important on the mesoscale as it was on the synoptic scale. For the divergence equation on the synoptic scale, the Coriolis term was on the same order as the other most significant terms. However, on the mesoscale, the effect of the earth's rotation was less important.

The general divergent initialization scheme required the solution of elliptic partial differential equations on a limited domain.

Since the domain was not cyclic or periodic, boundary conditions on the dependent variables were required. After an examination of what properties the boundary conditions should possess, suitable boundary conditions for geopotential, omega, and stream function were stated. A new method for the determination of boundary condition on velocity potential on a limited domain, mathematically equivalent to a Green's function solution for an infinite domain, was found such that the low-wavenumber boundary variation of velocity potential was accurate. This method's effectiveness was demonstrated on analytic velocity potential fields.

The forecast model used, the PSU mesoscale model, and its nondivergent initialization scheme were discussed briefly. The synoptic case chosen for study was also presented.

The finite-difference form of the omega equation was derived. From experiments conducted with this equation, it was concluded:

(1) The quasi-geostrophic omega equation with a diabatic term overestimated omega, especially in precipitation areas.

(2) The diabatic term in the mesoscale omega equation was the single most important term.

(3) The largest single uncertainty in the determination of omega and the divergent wind component was the representativeness of precipitation observations. This uncertainty was transmitted to the divergent wind components themselves. The uncertainty was large

enough that there is no advantage to calculating vertical velocities directly in sigma coordinates in order to avoid interpolation error.

The balance equation consistent with the model was derived in finite-difference form in sigma coordinates. The procedure for applying the balance equation was outlined.

Five experiments were conducted which started from the same synoptic time but which were initialized in a different manner. The initializations were:

(1) independent (unbalanced) analyses of winds and temperatures;

(2) as in (1) except the divergence was removed from the winds;

(3) nondivergent winds, geopotential calculated on pressure surfaces from the balance equation, and hydrostatically derived temperatures;

(4) nondivergent winds, geopotential calculated on sigma surfaces from the balance equation, and hydrostatically derived temperatures; and

(5) nondivergent and divergent wind components, geopotential calculated on sigma surfaces from the balance equation, and hydrostatically derived temperatures.

At the completion of each balanced initialization, superadiabatic lapse rates were present in the lowest model layer in the vicinity of the surface low pressure area. These were removed by applying a convective adjustment procedure to the balanced data.

The forecasts were compared and the following conclusions were reached:

(1) There was no large difference in the external gravity-wave noise characteristics of the forecasts as measured by graphs of $\overline{\left|\frac{\partial p_*}{\partial t}\right|}$ and $\overline{\left|\frac{\partial^2 p_*}{\partial t^2}\right|}$ versus time. However, the forecasts with unbalanced initial conditions had a consistently higher noise level than the balanced forecasts.

(2) There was no significant difference in the RMS forecast errors of sea level pressure or temperature and the wind components at the 400-, 500-, and 700-mb levels. This result was expected. The S1 scores for sea level pressure were best for the experiments with unbalanced initial conditions.

(3) For the experiments with balanced initial conditions, the precipitation forecasts were scored by an objective procedure. For the first three hours of the forecast, the divergent initialization experiment scored higher than the other forecasts. For the entire 12-hour period, all the forecasts scored equally well.

(4) The nondivergent forecasts experienced a precipitation deficit in the first half of the forecast period because the model had to develop a divergent component. They produced nearly the same amount of precipitation as the forecast with divergent initial conditions during the last half of the forecast period. Therefore, the divergent initialization produced the most accurate precipitation forecast for this case.

(5) The precipitation amounts for each hour were more realistic in the forecast with divergent initial conditions. The nondivergent forecasts displayed an oscillation associated with the mutual adjustment of the model's nondivergent and divergent wind components.

(6) The model "remembered" the divergent component in the experiment with divergent initialization. The initial precipitation amounts were nearly uniform. The area covered by the highest observed initial precipitation rates was underforecast and, therefore, the divergent initialization experiment did not predict as much precipitation as observed.

(7) Since the experiment with divergent initial conditions was initially closer to a balanced state and its initial precipitation rate was the most realistic, we conclude that the diagnosed omega values were sufficiently accurate to be useful in the divergent initialization performed here.

This thesis has the limitation that only one data case was studied. Even though this divergent initialization experiment significantly improved the short-term precipitation forecast for this data set, it cannot be concluded that divergent initialization will improve the precipitation forecast in every case. However, the divergent initialization procedure that was developed was general and should produce improved short-range precipitation forecasts on other cases.

8.1 Suggestions for further research

The balancing procedure described in Chapter 3 which is currently used by the PSU model should be improved. It can be made more consistent with the model while still balancing on pressure surfaces. Presently, temperatures are derived at dot points and then averaged to get temperatures at cross points where temperature is defined in the model. Temperatures should be derived directly at cross points since every unnecessary averaging or interpolation step introduces error in an initialization.

Manually digitized radar (MDR) data should be used to obtain the precipitation rate required by the divergent initialization in the omega equation diabatic term. These data are described in Moore et al. (1974). MDR data can provide a precipitation rate which is more spatially representative than raingauge observations, since MDR data represent entire grid squares. MDR data can also be obtained more

readily than rainfall observations. Unfortunately, MDR data are available only over the eastern half of the United States and therefore are of only limited usefulness.

The divergent and nondivergent initializations could be improved by incorporating a three-dimensional analysis scheme before the balancing procedure. This analysis should consider significant levels reported in rawinsonde data. This change should improve the vertical consistency between the mass and momentum variables, eliminate most of the superadiabatic lapse rates, and therefore enable the model to produce better forecasts.

The precipitation forecast produced by the divergent initialization presented here should be compared with a dynamic initialization on the same data set. This would determine which technique produces the better precipitation forecast. It is possible that the divergent initialization would produce comparable forecasts and at a significantly reduced computer cost.

The divergent initialization procedure should be applied on the synoptic scale. Then the results could be compared with those of other investigators.

For the forecasting of significant precipitation events, better forecasts would result if a complete radiation parameterization were incorporated into the model. This would be most useful in convective situations.

The divergent initialization scheme presented here should be extended to include the time-dependent terms in the omega and

divergence equations. The divergent initialization scheme could then be used at grid increments as small as 10 km. At a 10-km grid increment, an improved moisture initialization coupled with a divergent initialization would perhaps yield even better precipitation forecasts.

The divergent initialization scheme presented here should be tested on a grid increment of about 60 km for a heavy precipitation event. For example, the scheme should be quite useful at that grid increment in the initialization of hurricane models. If precipitation rate data is available (e.g., from satellite data) for a hurricane case, this technique should provide a realistic hurricane initialization.

APPENDIX 1

DERIVATION OF THE FINITE-DIFFERENCE FORM OF THE OMEGA EQUATION

Recall

$$\nabla^2(\sigma_s\omega) + f\,\zeta_a \frac{\partial^2\omega}{\partial p^2} = f\,\frac{\partial}{\partial p}\,\underset{\sim}{V}_\psi\cdot\nabla\zeta$$

$$+ f\,\frac{\partial}{\partial p}\,\underset{\sim}{V}_\chi\cdot\nabla\zeta + \frac{R}{p}\,\nabla^2\,\underset{\sim}{V}_\psi\cdot\nabla T + \frac{R}{p}\,\nabla^2\,\underset{\sim}{V}_\chi\cdot\nabla T \qquad (2.23)$$

$$- f\,\frac{\partial}{\partial p}\,\zeta D + f\,\frac{\partial}{\partial p}\,\omega\,\frac{\partial\zeta}{\partial p} + f\,\frac{\partial}{\partial p}\,\nabla\omega\cdot\nabla\,\frac{\partial\psi}{\partial p}$$

$$- \frac{R}{c_p p}\,\nabla^2 Q + f\,\frac{\partial}{\partial p}\,g\,\frac{\partial}{\partial p}\,\nabla\times\underset{\sim}{\tau}$$

where $\sigma_s = -\frac{RT}{p\theta}\frac{\partial\theta}{\partial p}$.

For each term, we will now derive its FD analog.

T1: From (2.23a), we can get

$$\sigma_s = -\frac{R}{p}\left[\frac{\partial T}{\partial p} - \kappa\,\frac{T}{p}\right] \quad . \qquad (A1.1)$$

Applying (A1.1) at point $(i,j,k+\frac{1}{2})$, we get

$$\sigma_{s_{i,j,k+\frac{1}{2}}} = -\frac{R}{p_{k+\frac{1}{2}}}\left[\frac{\delta T_{k+\frac{1}{2}}}{\delta p_{k+\frac{1}{2}}} - \kappa\,\frac{\overline{T}^{\sigma}_{k+\frac{1}{2}}}{\overline{p}^{\sigma}_{k+\frac{1}{2}}}\right] \quad . \qquad (A1.1a)$$

We will solve the FD analog of (2.23) for omega at full (standard-pressure) levels except for the top (200 mb) and the bottom (1000 mb) levels. Therefore, $\sigma_{s_{i,j,k+\frac{1}{2}}}$ is interpolated to $\sigma_{s_{i,j,k}}$ using $\overline{\sigma}^{\sigma}_{s_{i,j,k}}$. Since we do not have temperature data at the lowest pressure level, we set $\sigma_{i,j,1} = \sigma_{i,j,2}$. Therefore, T1 becomes, for level k,

$$(\sigma_{s_{i,j+1,k}}\omega_{i,j+1,k} + \sigma_{s_{i+1,j,k}}\omega_{i+1,j,k} + \sigma_{s_{i-1,j,k}}\omega_{i-1,j,k} + \sigma_{s_{i-1,j-1,k}}\omega_{i-1,j-1,k} - 4\sigma_{s_{i,j,k}}\omega_{i,j,k})\, m^2/(\Delta x)^2 \qquad \text{(A1.2)}$$

or

$$T1 = m^2(\sigma_s\omega)_{xx} + m^2(\sigma_s\omega)_{yy} \qquad \text{(A1.2a)}$$

in FD notation at point (i,j,k).

T2: $$f\zeta_a = f_{i,j}\,[m(v_{i,j,k})_x - m(u_{i,j,k})_y]$$

$$\frac{\partial\omega}{\partial p} = \frac{\delta\omega_{i,j,k}}{\delta p_k}$$

$$\frac{\partial^2\omega}{\partial p^2} = \frac{\delta}{\delta p_k}\frac{\delta\omega_{i,j,k}}{\delta p_k}$$

Therefore,

$$T2 = f_{i,j}\,[m(v_{i,j,k})_x - m(u_{i,j,k})_y]\,\frac{\delta}{\delta p_k}\,\frac{\delta \omega_{i,j,k}}{\delta p_k} \qquad \text{(A1.3)}$$

The terms on the RHS of (2.23) are forcing functions. Since we do not yet know omega, we do not know u_χ or v_χ. Hence, we will first describe the terms we can compute: T3, T5, T10, and T11. Also, the forcing functions will first be computed at half-levels.

T3: $\left(f\,\frac{\partial}{\partial p}\,\underset{\sim}{V}_\psi\cdot\nabla\zeta\right)_{i,j,k+\frac{1}{2}}$

$$= \frac{f_{i,j}\,[(\underset{\sim}{V}_\psi\cdot\nabla\zeta)_{i,j,k+1} - (\underset{\sim}{V}_\psi\cdot\nabla\zeta)_{i,j,k}]}{p_{k+1} - p_k}$$

$$= \frac{m_{i,j} f_{i,j}}{p_{k+1}-p_k}\,[u_{\psi_{i,j,k+1}}\,(\zeta_{i,j,k+1})_x + v_{\psi_{i,j,k+1}}\,(\zeta_{i,j,k+1})_y \qquad \text{(A1.4)}$$

$$- u_{\psi_{i,j,k}}\,(\zeta_{i,j,k})_x - v_{\psi_{i,j,k}}\,(\zeta_{i,j,k})_y]$$

T5: $\left(\frac{R}{p}\,\nabla^2\,\underset{\sim}{V}_\psi\cdot\nabla T\right)_{i,j,k+\frac{1}{2}}$

$$= \frac{R}{2p_{k+\frac{1}{2}}}\,[m_{i,j}^2\,(m_{i,j}\,u_{\psi_{i,j,k+1}}\,(T_{i,j,k+1})_x$$

$$+ m_{i,j}\,v_{\psi_{i,j,k+1}}\,(T_{i,j,k+1})_y)_{xx} + m_{i,j}^2\,(m_{i,j}\,u_{\psi_{i,j,k}}\,(T_{i,j,k})_x \qquad \text{(A1.5)}$$

$$+ m_{i,j}\,v_{\psi_{i,j,k}}\,(T_{i,j,k})_y)_{yy}]$$

T10: $$-\frac{R}{c_p p}\nabla^2 Q$$

where Q is the heating rate per unit mass. To determine the vertical distribution of Q, we follow Krishnamurti (1968a) and Anthes*. The specific humidity, q, is defined as the ratio of mass of water vapor to the total mass of air volume. If q is changing with time following a parcel, then

$$\frac{dh}{dt} = -L\frac{dq}{dt} \tag{A1.6}$$

is the heating rate per second per unit mass of air (L = latent heat of condensation ~ 580 cal/g of water). We assume that, in areas of precipitation, the air is saturated with respect to water vapor. In that case, expanding the material derivative on the RHS of (A1.6) yields

$$\frac{dh}{dt} = -L\left(\frac{\partial q_s}{\partial t} + \underset{\sim}{V}_H \cdot \nabla q_s + \omega\frac{\partial q_s}{\partial p}\right) \quad . \tag{A1.7}$$

We further assume that, in regions of precipitation, the first two terms on the RHS of (A1.7) are negligible compared to the third. That is,

*Anthes (1976) assumed a parabolic distribution of omega in the vertical arising from the latent heating. The entire portion of this description dealing with the determination of the parabolic omega profile is taken from his unpublished notes.

$$\frac{dh}{dt} = - L\omega \frac{\partial q_s}{\partial p} \quad . \tag{A1.8}$$

Integration of (A1.8) over the depth of the precipitating column per unit horizontal area can be written

$$\frac{1}{g} \int_{p_s}^{p_t} \frac{dh}{dt} \, dp = \frac{dQ}{dt} = \frac{L}{g} \int_{p_s}^{p_t} \omega \frac{\partial q_s}{\partial p} \, dp \quad . \tag{A1.9}$$

We can calculate $\frac{dQ}{dt}$, the heating rate through the column per unit area, from the rainfall rate, R (cm/d). First convert R to mass/(cm^2s):

$$\text{cm } H_2O \text{ d}^{-1} = \text{g cm}^{-2} \ H_2O \ \text{d}^{-1} \times 1 \text{ d}/8.64\text{x}10^5 \text{ s}$$

$$= 1.1574\text{x}10^{-5} \text{ g cm}^{-2} \text{ s}^{-1} \ H_2O$$

$$LR = 6.71\text{x}10^{-3} \text{ cal cm}^{-2} \text{ s}^{-1}$$

$$= 281 \text{ joule m}^{-2} \text{ s}^{-1} \quad .$$

Therefore,

$$\frac{dQ}{dt} = LR = 281 \ R \quad . \tag{A1.10}$$

Combining (A1.9) and (A1.10) yields

$$\int_{p_s}^{p_t} \omega \frac{\partial q_s}{\partial p} \, dp = \frac{g}{L} \frac{dQ}{dt}$$

$$= 1.134 \ R \text{ g s}^{-3} \ H_2O \text{ for } [R] = \text{cm d}^{-1} \tag{A1.11}$$

$$= 1.134\text{x}10^{-6} \ R \text{ cb s}^{-1} \quad .$$

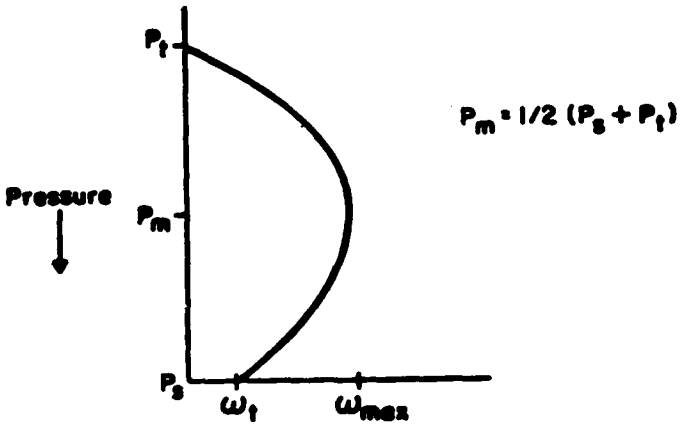

Fig. 35. Parabolic convective omega profile.

Now, we know $\frac{\partial q_s}{\partial p}$ from the initial data since we know the temperature at the pressure surfaces.

The third assumption in the determination of Q is that the omega profile that results is quadratic in pressure (reference Fig. 35).

$$\omega(p) = a + bp + cp^2 \qquad \text{(A1.12)}$$

The boundary conditions on the omega profile are

$$\omega(p_s) = \omega_t \qquad \text{(A1.13a)}$$

and

$$\omega(p_t) = 0 \quad . \qquad \text{(A1.13b)}$$

We also know that

$$\omega(p_m) = \omega_{max} \quad . \tag{A1.13c}$$

Therefore, we can write

$$\omega_t = a + bp_s + cp_s^2 \tag{A1.14a}$$

$$\omega_{max} = a + bp_m + cp_m^2 \quad . \tag{A1.14b}$$

$$0 = a + bp_t + cp_t^2 \tag{A1.14c}$$

Eliminating a between (A1.14a) and (A1.14c) yields

$$\omega_t = b(p_s-p_t) + c(p_s^2-p_t^2) \quad . \tag{A1.15a}$$

Eliminating a between (A1.14a) and (A1.14b) yields

$$\omega_t - \omega_{max} = b(p_s-p_m) + c(p_s^2-p_m^2) \quad . \tag{A1.15b}$$

Dividing (A1.15a) by (p_s-p_t) and (A1.15b) by (p_s-p_m) and eliminating b between the resulting equations yields

$$c = \frac{\omega_t-\omega_{max}}{(p_s-p_m)(p_m-p_t)} - \frac{\omega_t}{p_s-p_t} \quad . \tag{A1.16}$$

We now get b in terms of c from (A1.15b):

$$b = \frac{\omega_t - \omega_{max}}{p_s - p_m} - c(p_s + p_m) \quad . \tag{A1.17}$$

Given b and c, we obtain a from (A1.14c). Then (A1.12) can be solved for omega at any pressure level.

To calculate c, we need to know ω_{max}. We write (A1.11) in FD form as

$$\sum_{k=1}^{KMAX} \omega_{k+\frac{1}{2}} \, \delta q_{k+\frac{1}{2}} = R' \tag{A1.18}$$

where $R' = 1.134 \times 10^{-6}$ R and KMAX is one less than the number of levels. Substituting (A1.12) into (A1.18) yields

$$\sum_{k=1}^{KMAX} a\delta q_{k+\frac{1}{2}} + \sum_{k=1}^{KMAX} bp_{k+\frac{1}{2}} \, \delta q_{k+\frac{1}{2}} + \sum_{k=1}^{KMAX} cp^2_{k+\frac{1}{2}} \, \delta q_{k+\frac{1}{2}} = R' \quad . \tag{A1.19}$$

Equation (A1.19) can be rewritten

$$af_1 + bf_2 + cf_3 = R' \tag{A1.20}$$

where

$$f_1 = \sum_{k=1}^{KMAX} \delta q_{k+\frac{1}{2}} \quad , \tag{A1.20a}$$

$$f_2 = \sum_{k=1}^{KMAX} p_{k+\frac{1}{2}} \, \delta q_{k+\frac{1}{2}} \quad , \tag{A1.20b}$$

and

$$f_3 = \sum_{k=1}^{KMAX} p_{k+\frac{1}{2}}^2 \, \delta q_{k+\frac{1}{2}} \quad . \tag{A1.20c}$$

Note that we can calculate f_1, f_2, and f_3. Solving (A1.20) for c yields

$$c = \frac{R' - af_1 - bf_2}{f_3} \quad . \tag{A1.21}$$

Now, solving (A1.14c) for a yields

$$a = - bp_t - cp_t^2 \quad . \tag{A1.21a}$$

Using (A1.17) in (A1.21a) for b and inserting that result into (A1.21) leads to

$$\begin{aligned} c = \frac{1}{f_3} [R' + \{[\frac{\omega_t - \omega_{max}}{p_s - p_m} - c(p_s + p_m)] \, p_t \\ + cp_t^2\} \, f_1 - [\frac{\omega_t - \omega_{max}}{p_s - p_m} - c(p_s + p_m)] \, f_2] \end{aligned} \tag{A1.22}$$

$$= \frac{R' + \frac{\omega_t - \omega_{max}}{p_s - p_m} (p_t f_1 + f_2)}{p_t f_1 (p_s + p_m - p_t) - f_2 (p_s + p_m) + f_3} \quad .$$

Let h be the denominator of (A1.22). Now, substituting (A1.16) into (A1.22) and solving for ω_{max} using the result that $\frac{p_s - p_m}{p_s - p_t} = 1/2$, we get

$$\omega_{max} = \frac{\frac{1}{2}\omega_t - \frac{\omega_t(p_m-p_t)(p_t f_1 - f_2)}{h} + \frac{R'(p_s-p_m)(p_m-p_t)}{h}}{1 - \frac{p_m-p_t}{h}(p_t f_1 + f_2)} \quad . \qquad \text{(A1.23)}$$

To summarize, we can calculate from observations R', f_1, f_2, f_3, p_s, ω_s, and upon setting p_t, we know p_m. Therefore, we can use (A1.23) to get ω_{max}. We then use (A1.22) to get c, (A1.17) to get b, and (A1.14a) to get a. Omega as a function of pressure is now given by (A1.12). Since we know the omega profile due to latent heating, we can return to (A1.11) and calculate

$$\dot{Q}_{k+\frac{1}{2}} = - L \, \bar{\omega}^{\sigma}_{k+\frac{1}{2}} \frac{\delta q_{s_{k+\frac{1}{2}}}}{\delta p_{k+\frac{1}{2}}} \qquad \text{(A1.24)}$$

where

$$q_{s_{k+\frac{1}{2}}} = \frac{\varepsilon \, e_{s_{k+\frac{1}{2}}}}{p_{k+\frac{1}{2}}} = \frac{0.622}{p_{k+\frac{1}{2}}} \times 0.611 \times \exp\left\{\frac{m_v L}{R^*}\left[\frac{1}{273} - \frac{1}{T_{k+\frac{1}{2}}}\right]\right\} \quad . \qquad \text{(A1.25)}$$

Finally, given $\dot{Q}_{k+\frac{1}{2}}$, we calculate T10 using

$$T10 = - \frac{R}{c_p \, \bar{p}^{\sigma}_{k+\frac{1}{2}}} \left[(\dot{Q}_{k+\frac{1}{2}})_{xx} + (\dot{Q}_{k+\frac{1}{2}})_{yy}\right] \quad . \qquad \text{(A1.26)}$$

T11: $T11 = f \dfrac{\partial \, Fr}{\partial p}$

First of all, this term only applies in the lowest level (K=KMAX + 1). Secondly, it only applies to the lowest 10 cb of the PBL. Hence Δp in T11 is 10 cb. As in the forecast model,

$$Fr_x = g\ \rho_s\ C_D\ V_{KMAX+1}\ u_{KMAX+1} \tag{A1.27}$$

where Fr_x is the x-component of the frictional force, ρ_s is the surface air density (here, 10^{-3} g cm^{-3}), $C_D = 0.002$, u_{KMAX+1} is the 1000-mb u component, and V_{KMAX+1} is the 1000-mb wind speed, calculated from

$$V_{KMAX+1} = (u^2_{KMAX+1} + v^2_{KMAX+1})^{\frac{1}{2}} \quad . \tag{A1.28}$$

Similarly,

$$Fr_y = g\ \rho_s\ C_D\ V_{KMAX+1}\ v_{KMAX+1} \quad . \tag{A1.29}$$

Recall that we now know the forcing functions T3, T5, T10, and T11 at half-levels. Therefore, we interpolate them to the full levels from K = 2 through K = KMAX. Let $F_{i,j,k}$ represent the total forcing function at each grid point. We can now rewrite T1, T2, and $F_{i,j,k}$, using (A1.2a) and (A1.3), as

$$\begin{aligned} &m^2_{i,j}\ [(\sigma_{s_{i,j,k}}\ \omega_{i,j,k})_{xx} + (\sigma_{s_{i,j,k}}\ \omega_{i,j,k})_{yy}] \\ &+ m^2_{i,j}\ f_{i,j}\ [(v_{i,j,k})_x - (u_{i,j,k})_y]\ \frac{\delta}{\delta p_k}\ \frac{\delta \omega_{i,j,k}}{\delta p_k} = F_{i,j,k} \quad . \end{aligned} \tag{A.30}$$

Mathematically, this is a second-order elliptic PDE and, given boundary conditions on the top, bottom, and side faces of the domain, (A1.30) can be solved by a standard relaxation technique (Haltiner, 1971). The appropriate boundary conditions that will be used are given in Section 2.3.3. Let $R^n_{i,j,k}$ be the residual (the difference between the LHS and RHS of (A1.30)) after the n^{th} iteration using $\omega^n_{i,j,k}$. Then, we want to find $\omega^{n+1}_{i,j,k}$ such that $R^{n+1}_{i,j,k} = 0$. First, leaving out map factors, we write

$$R^n_{i,j,k} = \frac{1}{(\Delta x)^2}\left[(\sigma_s\omega^n)_{i+1,j,k} + (\sigma_s\omega^n)_{i-1,j,k} + (\sigma_s\omega^n)_{i,j+1,k} + (\sigma_s\omega^n)_{i,j-1,k} - 4(\sigma_s\omega^n)_{i,j,k}\right] + \frac{2B_{i,j,k}}{p_{k-1}-p_{k+1}}\left[\frac{\omega^n_{i,j,k-1} - \omega^n_{i,j,k}}{p_{k-1}-p_k} - \frac{\omega^n_{i,j,k} - \omega^n_{i,j,k+1}}{p_k-p_{k+1}}\right] - F_{i,j,k} \tag{A1.31}$$

where $B_{i,j,k} = f_{i,j}\,\zeta_{i,j,k}$. Adjusting $\omega^{n+1}_{i,j,k}$ such that $R^{n+1}_{i,j,k} = 0$ gives

$$0 = \frac{1}{(\Delta x)^2}\left[(\sigma_s\omega^n)_{i+1,j,k} + (\sigma_s\omega^n)_{i-1,j,k} + (\sigma_s\omega^n)_{i,j+1,k} + (\sigma_s\omega^n)_{i,j-1,k} - 4(\sigma_s\omega^{n+1})_{i,j,k}\right] + \frac{2B_{i,j,k}}{p_{k-1}-p_{k+1}}\left[\frac{\omega^n_{i,j,k-1} - \omega^{n+1}_{i,j,k}}{p_{k-1}-p_k} - \frac{\omega^{n+1}_{i,j,k} - \omega^n_{i,j,k+1}}{p_k-p_{k+1}}\right] . \tag{A1.32}$$

Subtracting (A1.31) from (A1.32) and simplifying yields

$$\omega^{n+1}_{i,j,k} = \omega^{n}_{i,j,k} + \frac{R^{n}_{i,j,k}}{\frac{4\sigma_{s_{i,j,k}}}{(\Delta x)^2} + \frac{2B_{i,j,k}}{p_{k-1}-p_{k+1}}\left(\frac{1}{p_{k-1}-p_{k}} + \frac{1}{p_{k}-p_{k+1}}\right)} \quad \text{(A1.33)}$$

After applying (A1.33) repeatedly, we will have omega at every grid point in the 30 x 35 x 7 domain. With this knowledge, we can apply the method for the determination of χ_B discussed in Section 2.3.4 to determine u_χ and v_χ at the half levels. Interpolation provides u_χ and v_χ at the full levels. Now we can return to calculate the remaining forcing functions in (2.23). They are T4, T6, T7, T8, and T9.

T4: This term is exactly like T3 except in (A1.4) replace $u_{\psi_{i,j,k}}$, $u_{\psi_{i,j,k+1}}$, $v_{\psi_{i,j,k}}$, and $v_{\psi_{i,j,k+1}}$ with $u_{\chi_{i,j,k}}$, $u_{\chi_{i,j,k+1}}$, $v_{\chi_{i,j,k}}$, and $v_{\chi_{i,j,k+1}}$, respectively.

T6: This term is exactly like T5 except in (A1.5) replace $u_{\psi_{i,j,k}}$, $u_{\psi_{i,j,k+1}}$, $v_{\psi_{i,j,k}}$, and $v_{\psi_{i,j,k+1}}$ with $u_{\chi_{i,j,k}}$, $u_{\chi_{i,j,k+1}}$, $v_{\chi_{i,j,k}}$, and $v_{\chi_{i,j,k+1}}$, respectively.

T7: $f \frac{\partial}{\partial p} \zeta D$

$D_{i,j,k+\frac{1}{2}}$ is available from the determination of u_χ and v_χ since

$$\nabla^2 \chi_{i,j,k+\frac{1}{2}} = D_{i,j,k+\frac{1}{2}} = - \frac{\delta \omega_k}{\delta p_k} \quad . \tag{A1.34}$$

Therefore, we can write T7 as

$$f_{i,j} D_{i,i,k+\frac{1}{2}} \frac{\delta \zeta_{i,j,k+\frac{1}{2}}}{\delta p_{k+\frac{1}{2}}} \quad . \tag{A1.35}$$

T7 is valid at half levels.

T8: $f \frac{\partial}{\partial p} \omega \frac{\partial \zeta}{\partial p}$

$$T8 = f_{i,j} \frac{\delta}{\delta p_k} \overline{\omega}^{\sigma}_k \frac{\delta}{\delta p_k} \zeta_{i,j,k} \tag{A1.36}$$

T8 applies at full levels.

T9: $f \frac{\partial}{\partial p} \nabla\omega \cdot \frac{\partial}{\partial p} \nabla\psi$

$$T9 = f_{i,j} \frac{\delta}{\delta p_k} [\overline{\omega}^{\sigma}_{i,j,k_x} \frac{\delta}{\delta p_k} v_{\psi_{i,j,k}} - \overline{\omega}^{\sigma}_{i,j,k_y} \frac{\delta}{\delta p_k} u_{\psi_{i,j,k}}] \tag{A1.37}$$

T9 applies at full levels.

To incorporate these terms into the omega relaxation scheme, we must first interpolate T4, T6, and T7 to full levels. Note that T8

and T9 already apply at full levels. Second, only one of the above terms contains $\omega_{i,j,k}$ itself. Expanding (A1.36) we get, for the n^{th} iteration,

$$T8 = \frac{f_{i,j}}{p_{k+\frac{1}{2}}-p_{k-\frac{1}{2}}} \left[\frac{1}{2}\left(\omega^n_{i,j,k+1} + \omega^n_{i,j,k}\right) \frac{(\zeta_{i,j,k+1} - \zeta_k)}{p_{k+1}-p_k}\right.$$

$$\left. - \frac{1}{2}\left(\omega^n_{i,j,k} + \omega^n_{i,j,k-1}\right) \frac{(\zeta_{i,j,k} - \zeta_{i,j,k-1})}{p_k-p_{k-1}}\right] \quad . \tag{A1.38}$$

We can now place this term on the LHS of (A1.30), perform the appropriate modification to (A1.31) and (A1.32), and in place of (A1.33) we get

$$\omega^{n+1}_{i,j,k} = \omega^n_{i,j,k} + \frac{R^n_{i,j,k}}{T1 + T2 + T3 + T4} \tag{A1.39}$$

where

$$T1 = \frac{4\sigma_{s_{i,j,k}}}{(\Delta x)^2} \quad ,$$

$$T2 = \frac{2B_{i,j,k}}{p_{k-1}-p_{k+1}} \left(\frac{1}{p_{k-1}-p_k} + \frac{1}{p_k-p_{k+1}}\right) \quad ,$$

$$T3 = \frac{f_{i,j}(\zeta_{i,j,k-1} - \zeta_{i,j,k})}{(p_{k-1}-p_{k+1})(p_{k-1}-p_k)} \quad ,$$

and

$$T4 = \frac{f_{i,j}(\zeta_{i,j,k} - \zeta_{i,j,k+1})}{(p_{k-1}-p_{k+1})(p_k-p_{k+1})} \quad .$$

After applying (A1.39) for a sufficient number of iterations over the domain, we have omega defined over the domain to the accuracy permitted by (2.23) and the observations.

Given omega over the domain, we can compute the divergence and velocity potential, the latter of which provides u_χ and v_χ. This completes the set of data required for the divergent initialization on sigma surfaces.

APPENDIX 2

DERIVATION OF THE FINITE-DIFFERENCE FORM OF THE BALANCE EQUATION

The term designators used refer to the terms in (6.6).

T1 and T2:

$$\overline{\phi_{x}}^{y}_{i,j} = \frac{m_{i,j}}{2\Delta x}(\phi_{i+\frac{1}{2},j+\frac{1}{2}} + \phi_{i-\frac{1}{2},j+\frac{1}{2}} - \phi_{i+\frac{1}{2},i-\frac{1}{2}} - \phi_{i-\frac{1}{2},j-\frac{1}{2}})$$

where i and j refer to dot points.

$$\overline{\overline{\phi_{x}}^{y}}^{y} = \frac{m_{i+\frac{1}{2},j}}{4\Delta x}(\phi_{i+1,j+\frac{1}{2}} + \phi_{i,j+\frac{1}{2}} - \phi_{i+1,j-\frac{1}{2}} - \phi_{i,j-\frac{1}{2}})$$

$$+ \frac{m_{i-\frac{1}{2},j}}{4\Delta x}(\phi_{i,j+\frac{1}{2}} + \phi_{i-1,j+\frac{1}{2}} - \phi_{i,j-\frac{1}{2}} - \phi_{i-1,j-\frac{1}{2}})$$

$$T1 = (\overline{\overline{\phi_{x}}^{y}}^{y})_{x_{i,j}} = \frac{m_{i,j}}{\Delta x}\left[\frac{m_{i+\frac{1}{2},j+\frac{1}{2}}}{4\Delta x}(\phi_{i+1,j+1} + \phi_{i,j+1} - \phi_{i+1,j} - \phi_{i,j})\right.$$

$$+ \frac{m_{i-\frac{1}{2},j+\frac{1}{2}}}{4\Delta x}(\phi_{i,j+1} + \phi_{i-1,j+1} - \phi_{i,j} - \phi_{i-1,j})$$

$$- \frac{m_{i+\frac{1}{2},j-\frac{1}{2}}}{4\Delta x}(\phi_{i+1,j} + \phi_{i,j} - \phi_{i+1,j-1} - \phi_{i,j-1})$$

$$\left. - \frac{m_{i-\frac{1}{2},j-\frac{1}{2}}}{4\Delta x}(\phi_{i,j} + \phi_{i-1,j} - \phi_{i,j-1} - \phi_{i-1,j-1})\right]$$

where i,j now refer to cross points.

Similarly, for T2,

$$\overline{\phi_y}^{x}_{i,j} = \frac{m_{i,j}}{2\Delta x}\left(\phi_{i+\frac{1}{2},j+\frac{1}{2}} + \phi_{i+\frac{1}{2},j-\frac{1}{2}} - \phi_{i-\frac{1}{2},j+\frac{1}{2}} - \phi_{i-\frac{1}{2},j-\frac{1}{2}}\right)$$

where i,j refer to dot points.

$$T2 = \left(\overline{\overline{\phi_y}^{x}}\right)_{y_{i,j}} = \frac{m_{i,j}}{\Delta x}\left[\frac{m_{i+\frac{1}{2},j+\frac{1}{2}}}{4\Delta x}\left(\phi_{i+1,j+1} + \phi_{i+1,j} - \phi_{i,j+1} - \phi_{i,j}\right)\right.$$

$$+ \frac{m_{i+\frac{1}{2},j-\frac{1}{2}}}{4\Delta x}\left(\phi_{i+1,j} + \phi_{i+1,j+1} - \phi_{i,j} - \phi_{i,j-1}\right)$$

$$- \frac{m_{i-\frac{1}{2},j+\frac{1}{2}}}{4\Delta x}\left(\phi_{i,j+1} + \phi_{i,j} - \phi_{i-1,j+1} - \phi_{i-1,j}\right)$$

$$\left. - \frac{m_{i-\frac{1}{2},j-\frac{1}{2}}}{4\Delta x}\left(\phi_{i,j} + \phi_{i,j-1} - \phi_{i-1,j} - \phi_{i-1,j-1}\right)\right]$$

where i,j now refer to cross points.

Summing T1 and T2 yields the LHS of (6.6):

$$T1 + T2 = \frac{m_{i,j}}{2(\Delta x)^2}\left[m_{i+\frac{1}{2},j+\frac{1}{2}}\phi_{i+1,j+1} + m_{i-\frac{1}{2},j+\frac{1}{2}}\phi_{i-1,j+1}\right.$$

$$+ m_{i+\frac{1}{2},j-\frac{1}{2}}\phi_{i+1,j-1} + m_{i-\frac{1}{2},j-\frac{1}{2}}\phi_{i-1,j-1}$$

$$\left. - \left(m_{i+\frac{1}{2},j+\frac{1}{2}} + m_{i+\frac{1}{2},j-\frac{1}{2}} + m_{i-\frac{1}{2},j+\frac{1}{2}} + m_{i-\frac{1}{2},j-\frac{1}{2}}\right)\phi_{i,j}\right] .$$

Note that in FD notation,

$$4\,\overline{\overline{m_{i,j}}^{xy}} = m_{i+\frac{1}{2},j+\frac{1}{2}} + m_{i+\frac{1}{2},j-\frac{1}{2}} + m_{i-\frac{1}{2},j+\frac{1}{2}} + m_{i-\frac{1}{2},j-\frac{1}{2}} .$$

The RHS of (6.6) (terms T3 through T12) are the forcing functions. Once these are evaluated, they can be used with the expression for the sum of T1 and T2 to solve for $\phi_{i,j}$.

T3: $\overline{u}^x = \frac{1}{2}(u_{i,j+\frac{1}{2}} + u_{i,j-\frac{1}{2}})$ where i,j refer to dot points.

Note that $p_* u = \overline{up_*}^{xy}$. Let $p_{i,j} = \overline{p_*}^{xy}{}_{i,j}$ and let $A_{i,j} = p_{i,j} u_{i,j}$. Then $\left.\frac{\widehat{A}}{m}^y\right|_{i,j} = \frac{1}{4m_{i,j}} (A_{i+1,j} + 2A_{i,j} + A_{i-1,j})$.

$$\text{T3a} = \left.\frac{\overline{\widehat{A}}^{yx}}{m}\right|_{i,j} = \frac{1}{8}\left[\frac{1}{m_{i,j+\frac{1}{2}}} (A_{i+1,j+\frac{1}{2}} + 2A_{i,j+\frac{1}{2}} + A_{i-1,j+\frac{1}{2}}) + \frac{1}{m_{i,j-\frac{1}{2}}} (A_{i+1,j-\frac{1}{2}} + 2A_{i,j-\frac{1}{2}} + A_{i-1,j-\frac{1}{2}})\right]$$

$$\begin{aligned}(\overline{u}^x \text{ T3a})_x = \frac{m_{i,j}}{16\Delta x} \Bigg[\Bigg(& \left(\frac{1}{m_{i,j+1}} (A_{i+1,j+1} + 2A_{i,j+1} + A_{i-1,j+1}) + \frac{1}{m_{i,j}} (A_{i+1,j} + 2A_{i,j} + A_{i-1,j})\right)(u_{i,j+1} + u_{i,j}) \\ & - (u_{i,j} + u_{i,j-1})\left(\frac{1}{m_{i,j}} (A_{i+1,j} + 2A_{i,j} + A_{i-1,j}) + \frac{1}{m_{i,j-1}} (A_{i+1,j-1} + 2A_{i,j-1} + A_{i-1,j-1})\right)\Bigg)\Bigg]\end{aligned}$$

$$\text{Let } Al_{i,j} = A_{i+1,j+1} + 2A_{i,j+1} + A_{i-1,j+1}$$

$$A2_{i,j} = A_{i+1,j} + 2A_{i,j} + A_{i-1,j}$$

$$A3_{i,j} = A_{i+1,j-1} + 2A_{i,j-1} + A_{i-1,j-1} \quad .$$

Simplifying yields

$$(\overline{u}^x\, T3a)_x = \frac{m_{i,j}}{16\Delta x}\left[\frac{(u_{i,j+1} + u_{i,j})}{m_{i,j+1}} Al_{i,j} + \frac{(u_{i,j+1} - u_{i,j-1})}{m_{i,j}} A2_{i,j}\right.$$

$$\left. - \frac{(u_{i,j} + u_{i,j-1})}{m_{i,j-1}} A3_{i,j}\right] \quad .$$

$$T3b_{i,j} = -\frac{m_{i,j}}{p_{i,j}} (\overline{u}^x\, T3a)_x$$

$$= -\frac{m^2_{i,j}}{16p_{i,j}\Delta x}\left[\frac{(u_{i,j+1} + u_{i,j})}{m_{i,j+1}} Al_{i,j} + \frac{(u_{i,j+1} - u_{i,j-1})}{m_{i,j}} A2_{i,j}\right.$$

$$\left. - \frac{(u_{i,j} + u_{i,j-1})}{m_{i,j-1}} A3_{i,j}\right]$$

$$= -\frac{1}{16\Delta x} T3c_{i,j}$$

where i,j still refers to dot points.

$$T3_{i+\frac{1}{2},j+\frac{1}{2}} = -\frac{m_{i+\frac{1}{2},j+\frac{1}{2}}}{32(\Delta x)^2}\,(T3c_{i+1,j+1} + T3c_{i,j+1} - T3c_{i+1,j} - T3c_{i,j})$$

Note that $1+\frac{1}{2},j+\frac{1}{2}$ is a cross point. For example,

$$T3c_{i+1,j+1} = \frac{m^2_{i+1,j+1}}{p_{i+1,j+1}} \left[\frac{(u_{i+1,j+2} + u_{i+1,j+1})}{m_{i+2,j+2}} A1_{i+1,j+1}\right.$$

$$+ \frac{(u_{i+1,j+2} - u_{i+1,j})}{m_{i+1,j+1}} A2_{i+1,j+1}$$

$$\left. - \frac{(u_{i+1,j} - u_{i+1,j})}{m_{i+1,j}} A3_{i+1,j+1}\right]$$

T4: Note $p_* v = \overline{vp_*}^{xy}$. Let $p_{i,j} = \overline{p_*}^{xy}$ and $B = p_{i,j} v_{i,j}$.

Then $\widetilde{\frac{B}{m}}^{x}\Big|_{i,j} = \frac{1}{4m_{i,j}} (B_{i,j+1} + 2B_{i,j} + B_{i,j-1})$.

$$T4a = \widetilde{\frac{B}{m}}^{xy}\Big|_{i,j} = \frac{1}{8} \left[\frac{1}{m_{i+\frac{1}{2},j}} (B_{i+\frac{1}{2},j+1} + 2B_{i+\frac{1}{2},j} + B_{i+\frac{1}{2},j-1})\right.$$

$$\left. + \frac{1}{m_{i-\frac{1}{2},j}} (B_{i-\frac{1}{2},j+1} + 2B_{i-\frac{1}{2},j} + B_{i-\frac{1}{2},j-1})\right.$$

$$(\overline{u}^{y}\ T4a)_y = \frac{m_{i,j}}{16\Delta x} \left[\frac{(u_{i+1,j} + u_{i,j})}{m_{i+1,j}} [(B_{i+1,j+1} + 2B_{i+1,j} + B_{i+1,j-1})\right.$$

$$\left. + \frac{1}{m_{i,j}} (B_{i,j+1} + 2B_{i,j} + B_{i,j-1})\right]$$

$$- (u_{i,j} + u_{i-1,j}) \left[\frac{1}{m_{i,j}} (B_{i,j+1} + 2B_{i,j} + B_{i,j-1})\right.$$

$$\left. + \frac{1}{m_{i-1,j}} (B_{i-1,j+1} + 2B_{i-1,j} + B_{i-1,j-1})\right]$$

Let $B1_{i,j} = B_{i+1,j+1} + 2B_{i+1,j} + B_{i+1,j-1}$

$B2_{i,j} = B_{i,j+1} + 2B_{i,j} + B_{i,j-1}$

$B3_{i,j} = B_{i-1,j+1} + 2B_{i-1,j} + B_{i-1,j-1}$.

Simplifying yields

$$(\overline{u}^{y}\ T4a)_{y} = \frac{m_{i,j}}{16\Delta x}\left[\frac{(u_{i+1,j} + u_{i,j})}{m_{i+1,j}} B1_{i,j} + \frac{(u_{i+1,j} - u_{i-1,j})}{m_{i,j}} B2_{i,j} - \frac{(u_{i,j} + u_{i-1,j})}{m_{i-1,j}} B3_{i,j}\right] .$$

$$T4b_{i,j} = -\frac{m_{i,j}}{p_{i,j}} (\overline{u}^{y}\ T4a)_{y}$$

$$= -\frac{m^{2}_{i,j}}{16p_{i,j}\Delta x}\left[\frac{(u_{i+1,j} + u_{i,j})}{m_{i+1,j}} B1_{i,j} + \frac{(u_{i+1,j} - u_{i-1,j})}{m_{i,j}} B2_{i,j} - \frac{(u_{i,j} + u_{i-1,j})}{m_{i-1,j}} B3_{i,j}\right]$$

$$= -\frac{1}{16\Delta x} T4c_{i,j}$$

Therefore, T4 at cross point $i+\frac{1}{2},j+\frac{1}{2}$ can be written

$$T4_{i+\frac{1}{2},j+\frac{1}{2}} = -\frac{m_{i+\frac{1}{2},j+\frac{1}{2}}}{32(\Delta x)^{2}} (T4c_{i+1,j+1} + T4c_{i,j+1} - T4c_{i+1,j} - T4c_{i,j}) .$$

T5: T5 is analogous to T3 except that in T3c, u is replaced with v and, because the outside differentiation is with respect to y instead of x, the final expression is

$$T5_{i+\frac{1}{2},j+\frac{1}{2}} = -\frac{m_{i+\frac{1}{2},j+\frac{1}{2}}}{32(\Delta x)^{2}} (T3c_{i+1,j+1} + T3c_{i+1,j} - T3c_{i,j+1} - T3c_{i,j}) .$$

T6: T6 is analogous to T4 except that in T4c, u is replaced with v and, again because of the outside differentiation, the final expression is

$$T6_{i+\frac{1}{2},j+\frac{1}{2}} = -\frac{m_{i+\frac{1}{2},j+\frac{1}{2}}}{32(\Delta x)^2}\left(T4c_{i+1,j+1} + T4c_{i+1,j} - T4c_{i,j-1} - T4c_{i,j}\right) .$$

$$T7: \quad -\frac{1}{m\overline{p_*}^{xy}}\frac{\delta}{\delta\sigma}\left(\dot{\sigma}^{xy}\,\overline{p_* u}\right) = -\frac{1}{m\overline{p_*}^{xy}}\frac{\delta}{\delta\sigma}\left(\dot{\sigma}^{xy}\,\overline{u}^{\sigma}\,\overline{p_*}^{xy}\right)$$

$$= -\frac{1}{m}\frac{\delta}{\delta\sigma}\,\dot{\sigma}^{xy}\,\overline{u}^{\sigma}$$

$$\text{Therefore, } T7 = -\left[\overline{\frac{1}{m}\frac{\delta}{\delta\sigma}\left(\dot{\sigma}^{xy}\,\overline{u}^{\sigma}\right)}^{y}\right]_x .$$

$$\overline{\dot{\sigma}}^{xy}_{i,j,k+\frac{1}{2}} = \frac{1}{4}\left(\dot{\sigma}_{i+\frac{1}{2},j+\frac{1}{2},k+\frac{1}{2}} + \dot{\sigma}_{i+\frac{1}{2},j-\frac{1}{2},k+\frac{1}{2}} + \dot{\sigma}_{i-\frac{1}{2},j+\frac{1}{2},k+\frac{1}{2}} + \dot{\sigma}_{i-\frac{1}{2},j-\frac{1}{2},k+\frac{1}{2}}\right)$$

$$\overline{u}^{\sigma}_{i,j,k+\frac{1}{2}} = \frac{1}{2}\left(u_{i,j,k+1} + u_{i,j,k}\right)$$

$$\overline{\dot{\sigma}}^{xy}_{i,j,k+\frac{1}{2}}\,\overline{u}_{i,j,k+\frac{1}{2}} = \frac{1}{8}\left(\dot{\sigma}_{i+\frac{1}{2},j+\frac{1}{2},k+\frac{1}{2}} + \dot{\sigma}_{i+\frac{1}{2},j-\frac{1}{2},k+\frac{1}{2}} + \dot{\sigma}_{i-\frac{1}{2},j+\frac{1}{2},k+\frac{1}{2}}\right.$$

$$\left. + \dot{\sigma}_{i-\frac{1}{2},j-\frac{1}{2},k+\frac{1}{2}}\right)\left(u_{i,j,k+1} + u_{i,j,k}\right)$$

$$T7a_{i,j,k+\frac{1}{2}} = \frac{1}{8m_{i,j}(\sigma_{k+1} - \sigma_k)} [(\dot{\sigma}_{i+\frac{1}{2},j+\frac{1}{2},k+1} + \dot{\sigma}_{i+\frac{1}{2},j-\frac{1}{2},k+1}$$

$$+ \dot{\sigma}_{i-\frac{1}{2},j+\frac{1}{2},k+1} + \dot{\sigma}_{i-\frac{1}{2},j-\frac{1}{2},k+1})(u_{i,j,k+3/2} + u_{i,j,k+\frac{1}{2}})$$

$$- (\dot{\sigma}_{i+\frac{1}{2},j+\frac{1}{2},k} + \dot{\sigma}_{i+\frac{1}{2},j-\frac{1}{2},k} + \dot{\sigma}_{i-\frac{1}{2},j+\frac{1}{2},k} + \dot{\sigma}_{i-\frac{1}{2},j-\frac{1}{2},k})$$

$$(u_{i,j,k+\frac{1}{2}} + u_{i,k,k-\frac{1}{2}})]$$

$$= \frac{1}{8(\sigma_{k+1} - \sigma_k)} \; T7b_{i,j,k+\frac{1}{2}}$$

$$T7_{i+\frac{1}{2},j+\frac{1}{2}} = - \frac{m_{i+\frac{1}{2},j+\frac{1}{2}}}{16\Delta x(\sigma_{k+1} - \sigma_k)} (T7b_{i+1,j+1,k+\frac{1}{2}} + T7b_{i,j+1,k+\frac{1}{2}}$$

$$- T7b_{i+1,j,k+\frac{1}{2}} - T7b_{i,j,k+\frac{1}{2}})$$

T8: T8 is analogous to T7 except that the u is replaced by v in T7b. Also, the outside differentiation is with respect y instead of x and the final expression is

$$T8_{i+\frac{1}{2},j+\frac{1}{2}} = - \frac{m_{i+\frac{1}{2},j+\frac{1}{2}}}{16\Delta x(\sigma_{k+1} - \sigma_k)} (T7b_{i+1,j+1,k+\frac{1}{2}} + T7b_{i+1,j,k+\frac{1}{2}}$$

$$- T7b_{i,j+1,k+\frac{1}{2}} - T7b_{i,j,k+\frac{1}{2}}) \quad .$$

$$\text{T9:}\quad \text{T9a} = \frac{mR\overline{T}^{xy}\ \overline{\overline{p_*}^{\,y}}_{x}}{m\overline{p_*}^{xy}\ (1 + \frac{p_t}{\sigma\overline{p_*}^{xy}})} = \frac{R\overline{T}^{xy}\ \overline{\overline{p_*}^{\,y}}_{x}}{\overline{p_*}^{xy}\ (1 + p_t/\sigma)}$$

Let $p_{i,j} = \overline{p_*}^{xy}$.

$$\overline{T}^{xy}_{i,j} = \frac{1}{4}\ (T_{i+\frac{1}{2},j+\frac{1}{2}} + T_{i+\frac{1}{2},j-\frac{1}{2}} + T_{i-\frac{1}{2},j+\frac{1}{2}} + T_{i-\frac{1}{2},j-\frac{1}{2}})$$

$$p_{i,j} = \frac{1}{4}\ (p_{*i+\frac{1}{2},j+\frac{1}{2}} + p_{*i+\frac{1}{2},j-\frac{1}{2}} + p_{*i-\frac{1}{2},j+\frac{1}{2}} + p_{*i-\frac{1}{2},j-\frac{1}{2}})$$

$$\overline{\overline{p_*}^{\,y}}_{x_{i,j}} = \frac{m_{i,j}}{2\Delta x}\ (p_{*i+\frac{1}{2},j+\frac{1}{2}} + p_{*i-\frac{1}{2},j+\frac{1}{2}} - p_{*i+\frac{1}{2},j-\frac{1}{2}} - p_{*i-\frac{1}{2},j-\frac{1}{2}})$$

Therefore, T9a is

$$\text{T9a}_{i,j} = \frac{m_{i,j}}{2\Delta x}\ [\frac{(T_{i+\frac{1}{2},j+\frac{1}{2}} + T_{i+\frac{1}{2},j-\frac{1}{2}} + T_{i-\frac{1}{2},j+\frac{1}{2}} + T_{i-\frac{1}{2},j-\frac{1}{2}})}{(p_{*i+\frac{1}{2},j+\frac{1}{2}} + p_{*i+\frac{1}{2},j-\frac{1}{2}} + p_{*i-\frac{1}{2},j+\frac{1}{2}} + p_{*i-\frac{1}{2},j-\frac{1}{2}})}$$

$$\frac{(p_{*i+\frac{1}{2},j+\frac{1}{2}} + p_{*i-\frac{1}{2},j+\frac{1}{2}} - p_{*i+\frac{1}{2},j-\frac{1}{2}} - p_{*i-\frac{1}{2},j-\frac{1}{2}})}{(1 + p_t/\sigma)}] \quad .$$

$$\text{T9}_{i+\frac{1}{2},j+\frac{1}{2}} = -\frac{m_{i+\frac{1}{2},j+\frac{1}{2}}}{4(\Delta x)^2}\ (\text{T9a}_{i+1,j+1} + \text{T9a}_{i,j+1} - \text{T9a}_{i+1,j} - \text{T9a}_{i,j})$$

T10: T10 is analogous to T9 except that $\overline{\overline{p_*}^{\,x}}_{y}$ replaces $\overline{\overline{p_*}^{\,y}}_{x}$ and the outside differentiation is with respect to y instead of x.

$$\overline{\overline{p_*}^{\,x}}_{y} = \frac{m_{i,j}}{2\Delta x}\ (p_{*i+\frac{1}{2},j+\frac{1}{2}} + p_{*i+\frac{1}{2},j-\frac{1}{2}} - p_{*i-\frac{1}{2},j+\frac{1}{2}} - p_{*i-\frac{1}{2},j-\frac{1}{2}})$$

$$T10a_{i,j} = \frac{m_{i,j}}{2\Delta x}\left[\frac{(T_{i+\frac{1}{2},j+\frac{1}{2}} + T_{i+\frac{1}{2},j-\frac{1}{2}} + T_{i-\frac{1}{2},j+\frac{1}{2}} + T_{i-\frac{1}{2},j-\frac{1}{2}})}{(p_{*i+\frac{1}{2},j+\frac{1}{2}} + p_{*i+\frac{1}{2},j-\frac{1}{2}} + p_{*i-\frac{1}{2},j+\frac{1}{2}} + p_{*i-\frac{1}{2},j-\frac{1}{2}})}\right.$$

$$\left.\frac{(p_{*i+\frac{1}{2},j+\frac{1}{2}} + p_{*i+\frac{1}{2},j-\frac{1}{2}} - p_{*i-\frac{1}{2},j+\frac{1}{2}} - p_{*i-\frac{1}{2},j-\frac{1}{2}})}{(1 + p_t/\sigma)}\right]$$

$$T10_{i+\frac{1}{2},j+\frac{1}{2}} = -\frac{m_{i+\frac{1}{2},j+\frac{1}{2}}}{4(\Delta x)^2}\,(T10a_{i+1,j+1} + T10a_{i+1,j} - T10a_{i,j+1} - T10a_{i,j})$$

$$T11:\quad T11a = \frac{fp_*v}{m\overline{p_*}^{xy}} = \frac{fv\overline{p_*}^{xy}}{m\overline{p_*}^{xy}} = \frac{fv}{m}$$

$$T11a_{i,j} = \frac{fv}{m}\Big|_{i,j}$$

Therefore,

$$T11_{i+\frac{1}{2},j+\frac{1}{2}} = \frac{m_{i+\frac{1}{2},j+\frac{1}{2}}}{2\Delta x}\,(T11a_{i+1,j+1} + T11a_{i,j+1} - T11a_{i+1,j} - T11a_{i,j})\quad .$$

$$T12:\quad T12a = \frac{fp_*u}{m\overline{p_*}^{xy}} = \frac{fu\overline{p_*}^{xy}}{m\overline{p_*}^{xy}} = \frac{fu}{m}$$

$$T12a_{i,j} = \frac{fu}{m}\Big|i,j$$

Therefore,

$$T12_{i+\frac{1}{2},j+\frac{1}{2}} = -\frac{m_{i+\frac{1}{2},j+\frac{1}{2}}}{2\Delta x}\,(T12a_{i+1,j+1} + T12a_{i+1,j} - T12a_{i,j+1} - T12a_{i,j})\quad .$$

APPENDIX 3

OBJECTIVE PRECIPITATION SCORING PROCEDURE

In this appendix, we present the objective precipitation scoring procedure developed by Anthes (unpublished). Mesoscale models are now producing forecasts that are finer in scale than synoptic-model precipitation forecasts. Hence a mesoscale model might forecast the correct intensity and shape of a precipitation field but displace the field by some small distance. This forecast would receive a poor score with a conventional scoring method but the forecast does contain useful information. The skill score presented here was designed to detect forecast displacement errors.

Let PF and PO be N by M matrices of forecast and observed precipitation, respectively. An example matrix of the 29 by 34 fields used here is

$$P = \begin{vmatrix} P_{29,1} & \cdots & & & \cdots & P_{29,34} \\ \vdots & & & & & \vdots \\ \vdots & & & & & \vdots \\ \vdots & & & & & \vdots \\ \vdots & \vdots & & & & \vdots \\ \vdots & \vdots & & & & \vdots \\ \vdots & \vdots & & & & \vdots \\ P_{2,1} & P_{2,2} & \cdots & & & \vdots \\ P_{1,1} & P_{1,2} & \cdots & & \cdots & P_{1,34} \end{vmatrix} . \qquad \text{(A3.1)}$$

The skill of a forecast will be computed for various shifts or "lags" of the forecast and observed fields. A shift of the forecast field a distance $k\Delta x$ to the left with respect to the observed field will be given by a positive integer parameter k; similarly, a downward shift will be given by a positive ℓ. When the forecast and observed fields are shifted, a skill score will be computed for the overlap region only. Let A be the total number of points in the overlap region. Then A is given by

$$A = (N - \ell)(M - k) \quad . \tag{A3.2}$$

Define the variance of PO in the overlap region as

$$S_{PO} \equiv \begin{cases} A^{-1} \sum_{i=1}^{N-\ell} \sum_{j=1}^{M-k} (PO_{i,j} - \overline{PO})^2 & \ell>0,\ k>0 \\ A^{-1} \sum_{i=1}^{N-\ell} \sum_{j=1-k}^{M} (PO_{i,j} - \overline{PO})^2 & \ell>0,\ k<0 \\ A^{-1} \sum_{i=1-\ell}^{N} \sum_{j=1}^{M-k} (PO_{i,j} - \overline{PO})^2 & \ell<0,\ k>0 \\ A^{-1} \sum_{i=1-\ell}^{N} \sum_{j=1-k}^{M} (PO_{i,j} - \overline{PO})^2 & \ell<0,\ k<0 \end{cases} \tag{A3.3}$$

where

$$\overline{PO} = A^{-1} \sum_i \sum_j PO_{i,j} \quad . \tag{A3.4}$$

Similarly, the variance of forecast precipitation, S_{PF}, is given by (A3.3) except that $(PO_{i,j} - \overline{PO})^2$ is replaced by $(PF_{i,j} - \overline{PF})^2$. The elements $c_{\ell,k}$ of a matrix C are defined as

$$AS_{PO}^{\frac{1}{2}} S_{PF}^{\frac{1}{2}} c_{\ell,k} \equiv \begin{cases} \sum_{i=1}^{N-\ell} \sum_{j=1}^{M-k} (PO_{i,j} - \overline{PO})(PF_{i+\ell,j+k} - \overline{PF}) & \ell>0, \; k>0 \\ \sum_{i=1}^{N-\ell} \sum_{j=1-k}^{M} (PO_{i,j} - \overline{PO})(PF_{i+\ell,j+k} - \overline{PF}) & \ell>0, \; k<0 \\ \sum_{i=1-\ell}^{N} \sum_{j=1}^{M-k} (PO_{i,j} - \overline{PO})(PF_{i+\ell,j+k} - \overline{PF}) & \ell<0, \; k>0 \\ \sum_{i=1-\ell}^{N} \sum_{j=1-k}^{M} (PO_{i,j} - \overline{PO})(PF_{i+\ell,j+k} - \overline{PF}) & \ell<0, \; k<0 \end{cases} \tag{A3.5}$$

Let ℓ and k vary over some range. For example, let $\ell = k = 2$. Then the matrix C is

$$C = \begin{vmatrix} c_{-2,-2} & c_{-2,-1} & c_{-2,0} & c_{-2,1} & c_{-2,2} \\ c_{-1,-2} & c_{-1,-1} & c_{-1,0} & c_{-1,1} & c_{-1,2} \\ c_{0,-2} & c_{0,-1} & c_{0,0} & c_{0,1} & c_{0,2} \\ c_{1,-2} & c_{1,-1} & c_{1,0} & c_{1,1} & c_{1,2} \\ c_{2,-2} & c_{2,-1} & c_{2,0} & c_{2,1} & c_{2,2} \end{vmatrix} \tag{A3.6}$$

The elements $c_{\ell,k}$ of the matrix C are the correlation coefficients between the observed and forecast precipitation fields for a given

displacement defined by ℓ and k. The maximum element of C represents the highest correlation between the observed and forecast patterns. The values of ℓ and k represent the spatial offset necessary to achieve the best score. Good forecasts would have a large maximum $c_{\ell,k}$ (1.0 is perfect) and, for the maximum $c_{\ell,k}$, low values of ℓ and k (0 and 0 are perfect).

REFERENCES

Adler, R. F., and E. B. Rodgers, 1977: Satellite-observed latent heat release in a tropical cyclone. Mon. Wea. Rev., 105, 956-963.

Ames, W. F., 1977: Numerical Methods for Partial Differential Equations. Academic Press, New York, 365 pp.

Anthes, R. A., 1976: Initialization of mesoscale models with real data. Preprint, Sixth Conference on Weather Forecasting and Analysis, Albany, 10-13 May 1976, American Meteorological Society, 156-160.

_____, 1977: A cumulus parameterization scheme utilizing a one-dimensional cloud model. Mon. Wea. Rev., 105, 270-286.

_____, 1978: Tests of a mesoscale model over Europe and the United States. Naval Postgraduate School Tech. Report NPS 63-78004, Monterey, CA, 107 pp.

_____, and T. T. Warner, 1978: The development of mesoscale models suitable for air pollution and other mesometeorological studies. Mon. Wea. Rev., 106, 1045-1078.

Asselin, R., 1972: Frequency filter for time integrations. Mon. Wea. Rev., 100, 487-490.

Baer, F., 1977: Adjustment of initial conditions required to suppress gravity oscillations in nonlinear flows. Beiträge zur Physik der Atmosphäre, 50, 350-366.

_____, and J. J. Tribbia, 1977: On complete filtering of gravity modes through nonlinear initialization. Mon. Wea. Rev., 105, 1536-1539.

Baumhefner, D. P., 1968: Application of a diagnostic numerical model to the tropical atmosphere. Mon. Wea. Rev., 96, 218-228.

Bedient, H. A., and J. Vederman, 1964: Computer analysis and forecasting in the tropics. Mon. Wea. Rev., 92, 565-577.

Bengtsson, L., 1975: Four-dimensional assimilation of meteorological observations. GARP Publication Series No. 15, World Meteorological Organization, Geneva, Switzerland, 76 pp.

Benwell, G. R. R., A. J. Gadd, J. F. Keers, M. S. Timpson, and P. W. White, 1971: The Bushby-Timpson 10-level model on a fine mesh. Meteorological Office Scientific Paper No. 32, Her Majesty's Stationary Office, London, 72 pp.

REFERENCES (Continued)

Bergthórsson, P., and B. R. Döös, 1955: Numerical weather map analysis. Tellus, 7, 329-340.

Bleck, R., 1977: Numerical simulation of lee cyclogenesis in the Gulf of Genoa. Mon. Wea. Rev., 105, 428-445.

Blumen, W., 1975: An analytical view of updating meteorological variables. Part I. J. Atmos. Sci., 32, 274-286.

Brown, J. A., Jr., and K. A. Campana, 1978: An economical time-differencing scheme for numerical weather prediction models. Mon. Wea. Rev., 106, 1125-1136.

_____, and J. R. Neilon, 1961: Case studies of numerical wind analysis. Mon. Wea. Rev., 89, 83-90.

Cahn, A., 1945: An investigation of the free oscillations of a simple current system. J. Meteor., 2, 113-119.

Charney, J. G., 1955: The use of the primitive equations of motion in numerical prediction. Tellus, 7, 22-26.

Cressman, G. P., 1959: An operational objective analysis system. Mon. Wea. Rev., 87, 367-374.

Deardorff, J. W., 1972: Parameterization of the planetary boundary layer for use in general circulation models. Mon. Wea. Rev., 100, 93-106.

Dey, C. H., and R. D. McPherson, 1977: An experiment in global divergent initialization. Mon. Wea. Rev., 105, 1372-1383.

Dickinson, R. E., and D. L. Williamson, 1972: Free oscillations of a discrete stratified fluid with application to numerical weather prediction. J. Atmos. Sci., 29, 623-640.

Dutton, J. A., 1976: The Ceaseless Wind, An Introduction to the Theory of Atmospheric Motion. McGraw-Hill, New York, 579 pp.

Elsberry, R. L., and G. W. Ley, 1976: On the strategy of initializing nested grid meshes in numerical weather prediction. Mon. Wea. Rev., 104, 797-799.

Endlich, R. M., 1967: An iterative method for altering the kinematic properties of wind fields. Mon. Wea. Rev., 95, 837-844.

REFERENCES (Continued)

Fankhauser, J. C., 1974: The derivation of consistent fields of wind and geopotential height from mesoscale rawinsonde data. J. Appl. Meteor., 13, 637-646.

Flattery, T. W., 1971: Spectral models for global analysis and forecasting. Proc. Sixth AWS Technical Exchange Conference, U. S. Naval Academy, 21-24 September 1970. Air Weather Service Tech. Report 242, 42-54.

Haltiner, G. J., 1971: Numerical Weather Prediction. Wiley, New York, 317 pp.

_____, and R. T. Williams, 1975: Some recent advances in numerical weather prediction. Mon. Wea. Rev., 103, 571-590.

Hawkins, H. F., Jr., 1972: Development of a seven-level, balanced, diagnostic model and its application to three disparate tropical disturbances. NOAA Tech. Memo. ERL NHRL-98, 207 pp.

_____, and S. L. Rosenthal, 1965: On the computation of stream functions from the wind field. Mon. Wea. Rev., 93, 245-252.

Hill, K., and R. E. Turner, 1977: NASA's atmospheric variability experiment (AVE). Bull. Amer. Meteor. Soc., 58, 170-172.

Hinklemann, K., 1951: Der Mechanimus des meteorologichen Lärmes. Tellus, 3, 285-296.

Hoke, J. E., and R. A. Anthes, 1976: The initialization of numerical models by a dynamic-initialization technique. Mon. Wea. Rev., 104, 1551-1556.

Houghton, D. D., D. P. Baumhefner, and W. M. Washington, 1971: On global initialization of the primitive equations: Part II. The divergent component of the horizontal wind. J. Appl. Meteor., 12, 626-634.

Keyser, D., 1978: The initialization procedure for limited area models for numerical weather prediction. Naval Postgraduate School Tech. Report NPS63-78003, Monterey, California, 72 pp.

Krishnamurti, T. N., 1968a: A diagnostic balance model for studies of weather systems of low and high latitudes, Rossby number less than 1. Mon. Wea. Rev., 96, 197-207.

_____, 1968b: A study of a developing wave cyclone. Mon. Wea. Rev., 96, 208-217.

REFERENCES (Continued)

Lejenäs, H., 1977: Initialization of primitive equation models - Some aspects of including a divergent component into the initial state. Contributions to Atmospheric Physics, 50, 154-168.

Lorenz, E. N., 1965: A study of the predictability of a 28-variable atmospheric model. Tellus, 17, 321-333.

Lubeck, O. M., T. Rosmond, and R. T. Williams, 1977: Divergent initialization experiments using a spectral model. Naval Postgraduate School Tech. Report NPS-63Wu7791, Monterey, California, 75 pp.

Machenhauer, B., 1977: On the dynamics of gravity oscillations in a shallow water model, with applications to normal mode initialization. Beiträge zur Physik der Atmosphäre, 50, 253-271.

Mathur, M. B., 1974: A multiple-grid primitive equation model to simulate the development of an asymmetric hurricane (Isbell, 1964). J. Atmos. Sci., 31, 371-393.

Matsuno, T., 1966: Numerical integrations of the primitive equations by a simulated backward difference method. J. Meteor. Soc. Japan, Series II, 44, 76-84.

Miller, B. I., P. P. Chase, and B. R. Jarvinen, 1972: Numerical prediction of tropical weather systems. Mon. Wea. Rev., 100, 825-835.

Moore, P. L., A. D. Cummings, and D. L. Smith, 1974: The NWS manually-digitized radar program and its applicability to precipitation probability forecasting. Proc. Fifth Conference on Forecasting and Analysis, May 1974, Boston, 69-74.

Morse, P. M., and H. Feshbach, 1953: Methods of Theoretical Physics, McGraw-Hill, New York, 1978 pp.

Nitta, T., and J. B. Hovermale, 1967: On analysis and initialization for the primitive forecast equations. U. S. Weather Bureau Tech. Memo. NMC-42, 38 pp.

Økland, H., 1970: On the adjustment toward balance in primitive equation weather prediction models. Mon. Wea. Rev., 98, 271-279.

Orlanski, I., 1975: A rational subdivision of scales for atmospheric processes. Bull. Amer. Meteor. Soc., 56, 527-530.

REFERENCES (Continued)

Paegle, J., and J. N. Paegle, 1976: On geopotential data and ellipticity of the balance equation: a data study. Mon. Wea. Rev., 104, 1279-1288.

Panofsky, H. A., 1949: Objective weather map analysis. J. Meteor., 6, 386-392.

Phillips, N. A., 1958: Geostrophic errors in predicting the Appalachian storm of Nov. 1950. Geophysics, 5, 389-405.

_____, 1960: On the problem of initial data for the primitive equations. Tellus, 12, 121-126.

_____, 1963: Geostrophic Motion. Reviews of Geophysics, 2, 123-176.

Richardson, L. F., 1922: Weather Prediction by Numerical Process. Cambridge University Press, 236 pp.

Robert, A. J., 1966: The integration of a low order spectrum form of the primitive meteorological equations. J. Meteor. Soc. Japan, 44, 237-245.

Rosmond, T. E., and F. D. Faulkner, 1976: Direct solution of elliptic equations by block cyclic reduction and factorization. Mon. Wea. Rev., 104, 641-649.

Rossby, C. G., 1938: On the mutual adjustment of pressure and velocity distributions in certain simple current systems, II. J. Marine Res., 1, 239-263.

Sangster, W. E., 1960: A method of representing the horizontal pressure force without reduction of pressures to sea level. J. Meteor., 17, 166-176.

Sasaki, Y., 1958: An objective analysis based on the variational method. J. Meteor. Soc. Japan, Series II, 36, 77-88.

_____, 1969: Proposed inclusion of time variation terms, observational and theoretical, in numerical variational analysis. J. Meteor. Soc. Japan, Series II, 47, 115-124.

Schaeffer, J. T., and C. A. Doswell III, 1979: On the interpolation of a vector wind field. To appear in Mon. Wea. Rev.

Shaginaw, R., 1979: Effects of planetary boundary layer formulation on a subsynoptic-scale forecast. The Pennsylvania State University, Department of Meteorology, Master's Thesis, May, 1979, 101 pp.

REFERENCES (Continued)

Shukla, J., and K. R. Saha, 1974: Computation of nondivergent stream function and irrotational velocity potential from observed winds. Mon. Wea. Rev., 102, 419-425.

Shuman, F. G., and J. B. Hovermale, 1968: An operational six-layer primitive equation model. J. Appl. Meteor., 7, 525-547.

Smagorinsky, J., S. Manabe, and J. L. Holloway, Jr., 1965: Numerical results from a nine-level general circulation model of the atmosphere. Mon. Wea. Rev., 93, 727-768.

_____, and Staff Members, 1967: Prediction experiments with a general circulation model. Dynamics of Large-Scale Atmospheric Processes, Proc. of the International Symposium, Moscow, June 23-30, 1965, 70-134.

Stephens, J. J., and K. W. Johnson, 1978: Rotational and divergent wind potentials. Mon. Wea. Rev., 106, 1452-1457.

Sundqvist, H., 1975: Initialization for models using sigma as the vertical coordinate. J. Appl. Meteor., 14, 153-158.

Swarztrauber, P., and R. Sweet, 1975: Efficient FORTRAN subprograms for the solution of elliptic partial differential equations. National Center for Atmospheric Research Tech. Note NCAR-TN/IA-109, Boulder, Colorado, 139 pp.

Temperton, C., 1976: Dynamic initialization for barotropic and multi-level models. Quart. J. Royal Meteorol. Soc., 102, 297-311.

Teweles, S., Jr., and H. B. Wobus, 1954: Verification of prognostic charts. Bull. Amer. Meteor. Soc., 35, 455-463.

Thompson, P. D., 1961: Numerical Weather Analysis and Prediction. The MacMillan Company, 170 pp.

Warner, T. T., 1972: The initialization of jet maxima in a barotropic primitive equation model. The Pennsylvania State University, Department of Meteorology, Master's Thesis, June, 1972, 85 pp.

_____, R. A. Anthes, and A. L. McNab, 1978: Numerical simulations with a three-dimensional mesoscale model. Mon. Wea. Rev., 106, 1079-1099.

Washington, W. M., 1964: A note on the adjustment towards geostrophic equilibrium in a simple fluid system. Tellus, 16, 530-534.

REFERENCES (Continued)

Williamson, D. L., 1976: Normal mode initialization procedure applied to forecasts with the global shallow water equations. Mon. Wea. Rev., 104, 195-206.

_____, and R. E. Dickinson, 1976: Free oscillations of the NCAR global circulation model. Mon. Wea. Rev., 104, 1372-1391.

Wolcott, S. W., 1979: A humidity initialization scheme utilizing surface and satellite data. The Pennsylvania State University, Department of Meteorology, Master's Thesis, May, 1979, 75 pp.

VITA

Terry C. Tarbell was born on August 23, 1945, in Oklahoma City, Oklahoma. After graduation from Tumon High School, Agana, Guam, in June, 1963, he attended the University of New Hampshire and received his B.S. in Chemistry in June, 1967. Mr. Tarbell then entered the Air Force and received meteorology training at Texas A & M University.

Lieutenant Tarbell's next assignment was Andersen AFB, Guam, where he learned tropical and satellite meteorology. Captain Tarbell was assigned to The Pennsylvania State University in June, 1971, under the auspices of the Air Force Institute of Technology. He graduated with an M.S. in Meteorology in December, 1972. His previous thesis work was concerned with the extension of surface layer wind and temperature profile theory beyond the surface layer for unstable conditions.

Captain Tarbell was then assigned to the Air Force Global Weather Central near Omaha, Nebraska. Captain Tarbell was reassigned to The Pennsylvania State University in June, 1976.

Captain Tarbell is a member of Chi Epsilon Pi and a professional member of the American Meteorological Society.

END

DATE
FILMED
11-81

DTIC